Surface and Interfacial Approaches for the Characterization of Biomolecular Interactions and to Optimize DESI-MS Performance

Moriam Oluwaseun Ore

A dissertation submitted to the Faculty of Graduate Studies in Partial Fulfillment of the requirements for the degree of Doctor of Philosophy

Graduate Program in Chemistry
York University
Toronto, Ontario

July 2016

Abstract

This work involves the surface and interfacial characterization of biomolecular interactions by atomic force microscopy and optimization of desorption electrospray ionization mass spectrometry. In the first part (part I), suitable surface of functionalized porous silicon are created and characterized to enhance Desorption Electrospray Ionization Mass Spectrometry (DESI-MS) capability. DESI-MS is a powerful emerging analytical tool that finds applications in fundamental research and as a diagnostic tool. Enhancement of the performance of this technique will make it superior and improve the scope of its applications. The use of super hydrophobic porous silicon proved to enhance the desorption/ionization mechanism of DESI. It improves the ionization efficiency almost two fold when compared to the traditionally used glass slide and porous polytetraflouroethylene surfaces under the same conditions. The functionalized porous surfaces showed incredible stability, which is suitable for long time and high throughput analysis. We proposed a mechanism whereby the porous silicon acts as a barrier for the spray solvent, and creates a pool of analyte during desorption, leading to greater stability. On the other hand, the super hydrophobic functionality improves the ionization power of the technique by increasing analyte concentration over the area sampled and preventing filing of the pores. The functionalized porous surfaces are also suitable for DESI-imaging of biomolecules and tissue cells.

In the second part (part II) of this thesis, Atomic Force Microscopy (AFM) was used to confirm site-specific protein-DNA interaction of the vancomycin resistance associated regulatory protein (VraR) from *S. aureus*. The protein stoichiometry at the binding site was confirmed as being mostly dimer for VraR, and as oligomers for

phosphorylated VraR. In another project, AFM proved to be a very useful technique for the visualization and characterization of RNA. It enable us to visualized for the first time, the three dimensional structural architecture of genomic RNA of tomato bushy stunt virus. AFM allowed us to confirm the proposed long range-RNA-RNA interaction existing within the genome, leading to a more compact structure. Volume analyses enable to confirm the existence of compact structures as visualized in the AFM images. These results are consistent with expected conformations utilized by the TBSV virus for different viral processes. Sub-genomic RNA expressed by the TBSV virus, also exhibited compact structures with different degree of protrusions. All observed RNA and sub-genomic RNA structures from our AFM images were consistent with the selective 2'-hydroxyl acylation analyzed by primer extension (SHAPE) predicted structures.

Publications

1. Wu, B., Grigull, J., **Ore, M.O.,** Morin, S., White, K.A, " Global organization of a positive-strand RNA Virus genome", *PLoS Pathog,* 9(5) e1003363 (2013) 1-15.

2. Schwab, N.V., **Ore, M.O.,** Eberlin, M.N., Morin, S., Ifa, D.R, "Functionalized porous silicon surfaces as substrate for small molecule analysis", *Anal Chem.,* 86 (2014) 11722- 11726

3. Tata, A., Perez, C.J., **Ore, M.O.,** Lostun, D., Passas, A., Morin, S., Ifa, D.R. " Evaluation of imprint DESI-MS substrates for the analysis of fungal metabolites", *RSC Adv*., 5 (2015) 75458-75464.

4. **Ore, M.O.,** Belcheva, A., Wong, E., Gregor, J., Golemi-Kotra, D., and Morin, S, "Atomic force Microscopy Investigation of DNA binding activity of Vancomycin resistance associated regulatory protein, *in preparation*

Acknowledgements

I want to express my deepest appreciation to my supervisor Prof. Sylvie Morin for giving me the opportunity of working with her. It was her generous help and guidance that enabled me to complete my Ph.D. studies. She has supported and guided me throughout my research career, and for this I am very grateful.

Also, I would like to thank my committee members Prof. D. Wilson, Prof. R. Lew, Prof. A. White and Prof. D. Ifa for all their support, guidance and suggestions.

I cordially express my thanks and appreciation to Prof. Morin's group members, M. Hariri, A. Sepehrifard, S. Zahedijasbi, M. Nazari, A. Dumont, and all of the old members for their help, support, and the friendly atmosphere.

I would like to acknowledge the Natural Science and Engineering Research Council (NSERC) and Granting Agencies for their financial support. I also would like to show my gratitude to the Department of Chemistry and the Faculty of Graduate studies at York University.

Finally, I would like to thank my dear husband, Hafeez Tukuru for his love and for always believing in me. Thank you for always supporting and encouraging me. To my lovely daughters, A'shadieeyah and Hamdieeyah, who always bring a smile to my face and made each day worth living. My sincere and deepest appreciation goes to my dad Omotayo Muti Oreagba, and my sisters Habibat and Sekinat. To my mom Moriliat Olabisi Alatilehin Muti-Ore whose constant prayer and assistance with the kids enabled me to complete this work, to her I dedicate this thesis.

Statement of Collaboration

This thesis is presented in two parts. In part I, I completed all the work involving the fabrication, functionalization and characterization of porous silicon surfaces. All DESI-MS operation was performed in the laboratory of Prof. Demian Ifa, (Department of Chemistry, York University) with the assistance of Nicolas Schwab (Ph.D. candidate), Consuelo Perez and Amin Khatami (M.Sc. candidates), who are all acknowledged for their support throughout this project. Pore wetting SEM experiments were performed by Evgeny Modin (Ph.D candidate) and Prof. Sylvie Morin at the Electron Microscopy Laboratory led by Dr. Andrey Chuvilin at CIC Nanogune, San Sebastian, Spain.

In part II, I completed the work involving vancomycin resistance associated regulator protein expression, purification and DNA amplification, in the laboratory of Prof. Dasantila Golemi-Kotra (Department of Chemistry, York University) under the supervision of Antoaneta Belcheva (Ph.D. candidate). I completed all AFM imaging, characterization, protein and complex volume analysis in Prof. Morin's facility.

The work on AFM imaging of TBSV RNA was performed in collaboration with Prof. White, department of biology. Dr. Boadong Wu (post-doctoral fellow), from the laboratory of Prof. Andrew White (Department of Biology, York University) performed the RNA sample preparation and SHAPE analysis. Prof. Jörg Grigull (Department of Mathematics and Statistics, York University) performed the statistic guiding the shape structure and theoretical maximum distance ladder. I performed all AFM imaging and volume analysis of the RNA samples in Prof. Morin's facility.

Table of Contents

List of Figures

List of Tables

Chapter One

Introduction

1.1 Objectives of the thesis

Much research is currently centered on the use of novel analytical techniques for the investigation of the structure and functionality of various biological molecules. We undertook the work of functionalized porous silicon that was fabricated and used as substrate for enhancement of a high- throughput emerging analytical technique, desorption electrospray ionization mass spectrometry (DESI-MS). The key advantages of porous silicon are its unique tuneable features such as, surface area, thickness, porosity, pore size and its surface chemistry; not to mention it is biodegradable and biocompatible, which is why it is of interest for investigation of biomolecules and for specific cellular functions. Pore size and other physical characteristics were examined by scanning electron microscopy (SEM) and Fourier transform infrared spectroscopy (FTIR) and correlated with DESI-MS signal. The chemical modification of porous silicon, which provides optimization, and the stability of DESI-MS signal were examined for quantitative analysis of biological relevant small molecules. As well the functionalized porous silicon was used for imaging of rat brain tissues.

In addition a significant part of our work involved understanding specific pathogens namely *staphylococcus aureus* and tomato bushy stunt virus at the molecular level together with our collaborators. We made use of high resolution atomic force microscopy (AFM) for both structural and quantitative analysis of the extracted

biomolecules of interest from the above mention pathogens to obtain a better understanding of their functions. AFM was used for visualization of DNA-binding activity of a response regulatory protein (VraR) from *staphylococcus aureus mu50*. Member of a two-component regulatory system (VraS/VraR) involved in the control of cell wall peptidoglycan biosynthesis. Expression and purification of the protein was performed. The phosphorylated protein and the DNA-binding interaction were monitored on a mica surface by AFM. Quantitative volume analysis of both the protein and the protein-DNA complex for determination of stoichiometry of protein at the binding site was performed. Furthermore global structural organization of full-length tomato bushy stunt viral RNA and the different transcribed sub-genomic mRNA was investigated by AFM. We observed the three dimensional structure adopted by the RNA due to RNA-RNA long-range interactions. Diameter and volume analysis of the obtained RNA AFM images was performed.

1.2 Chapters of the thesis

This work makes use of novel analytical techniques for investigation of different health relevant biological samples at the molecular level. Having the ability to obtain and provide visual images of these biological samples is an ever-emerging scientific area, which is aiding in understanding various health-related biological systems both at the research and hospital levels. Two main techniques were utilized in this research namely DESI-MS and AFM, both unique and providing different but rather important information about the biological samples of interest.

In brief, the thesis is divided into two parts. Part I of the thesis reports the functionalization of porous silicon as substrate for enhancement of DESI-MS, which

includes chapters 2 to 7. Chapter 2 presents an introduction to DESI-MS and ways to improve its analytical capability. Chapter 3 illustrates the fabrication and characterization of porous silicon surface. This chapter provides details on materials and methods used for formation of porous silicon with varying pore diameters. Oxidation of porous silicon and its functionalization with 1-decene and heptadecafluoro-1,1,2,2-tetrahydrodecyl trimethoxsilane providing a hydrophobic substrate. Moreover this chapter provides insights on the key mechanistic properties of DESI-MS. In chapter 4, the results of the fabrication and characterization of functionalized porous silicon as monitored using SEM and FITR are presented. Chapter 5 includes the results from studies involving the use and application of the porous silicon surfaces as suitable substrate for DESI-MS. These studies lead to an optimization of signal intensity and stability. These substrates were further used for the investigation of biological relevant small molecules providing the lowest limit of detection at the time these results were published in 2015. These same substrates were also used for the investigation of DESI-MS imaging of rat brain tissue and the results are discussed in chapter 6. The final conclusions are presented in Chapter 7.

Part II of the thesis reports the AFM investigation of biomolecules, which includes chapters 8 to 12. Chapter 8 provides an introduction to the analytical methods used for the investigation of biomolecules, and the advantages of using AFM. Also discussed are the pathogens and the biological molecules investigated by AFM. In chapter 9 one can find a description of the materials and methods utilized, included therein is a detailed explanation of AFM. It illustrates AFM principles, break down of its machinery and also the information output provided from this techniques and how it was

utilized to help better understand the investigated biological samples. Chapter 10 presents the AFM results and a detailed discussion of DNA binding activity of the phosphorylated response regulatory protein obtained from vancomycin resistance *staphylococcus aureus* bacteria, which is one of the leading causes of hospital borne bacterial infections in North America. Also included are the volume analysis results from the AFM images. Chapter 11 presents the AFM results of the full genomic and sub-genomic RNA extracted from the TBSV virus. The AFM images were supported with, selective 2'-hydroxyl acylation analyzed by primer extension (SHAPE) analysis and statistical analysis of theoretical maximum ladder distance (MLD) from our collaborators. The final conclusions are presented in Chapter 12. Chapter 13 offers a perspective on the importance and relevance of our investigations of the various biological samples to science and how this can lead to future direction of research.

Part I: Functionalization of Porous Silicon as Substrate for Enhancement of Desorption Electrospray Ionization Mass Spectrometry Technique

Chapter Two

Introduction

2.1 Ambient ionization techniques

Few analytical techniques allow chemical analysis of untreated biological samples; and one of the most important is mass spectrometry. Mass spectrometry is a well-developed technique used for identification of compounds in a mixture and structural composition of large biomolecules. The critical step in mass spectrometry is the formation of gas-phase analyte ions from the sample. Method of ionizations such as electron ionization (EI), chemical ionization (CI), and field desorption involves the samples being introduced into high vacuum, which puts limitation on the various samples that can be analyzed [Gross, 2011]. Molecular ionization methods for creating ions from large biological molecules and biological complexes that were rather intractable, has been achieved by introduction of electrospray ionization (ESI) and matrix-assisted laser desorption ionization (MALDI) [Fenn et al., 1990; Bahr et al., 1992]. ESI can only be used for analysis of samples in liquid forms, while MALDI can be used for analysis of sample co-crystallized in matrix and deposited on suitable surfaces. The above methods however require time-consuming sample preparation procedures, thus preventing *in situ* and rapid sample analysis. These limitations prompted the investigation of alternative

surface ionization method that can allow direct sampling of analyte deposited on surfaces under ambient conditions [Takats et al., 2004].

Desorption electrospray ionization mass spectrometry (DESI-MS) was one of the first ambient ionization technique whereby ionization occurs externally to the inlet and only the analyte ions are introduce into the mass spectrometer [Ifa et al., 2010]. DESI-MS allows analysis of sample surface under native environment with minimal to no sample preparation. In DESI-MS, electrospray solvent directed towards the sample surface, hits the sample, picks up small analyte and large biomolecules, ionizes them as secondary droplet and delivers them to the mass analyzer [Cooks et al., 2006]. The mass analyzer provides information of ions based on their mass to charge ratio. After the introduction of DESI, there have been other successive ambient ionization techniques developed over the years. Some of the methods make use of the spray ionization method, i.e., desorption sonic spray ionization (DeSSI) [Haddad, Sparrapan and Eberline, 2006], and extractive electrospray ionization (EESI) [Chen and Zenobi, 2007]. Furthermore, there are the laser induced desorption coupled with electrospray ionization such as electrospray laser ablation ionization (ELDI) [Shiea et al., 2005], MALDI assisted electrospray ionization (MALDESI) [Sampson et al, 2006] and laser ablation electrospray ionization (LAESI) [Nemes and Vertes, 2007].

Also there are the extensions of the traditional chemical and photo ionization, such as desorption atmospheric pressure chemical (DAPCI) [Takats et al., 2005] and photo ionization (DAPPI) [Haapala et al., 2007]. Lastly we have the plasma assisted desorption ionization (PADI) [Ratcliffe et al., 2007] and ambient solid analysis probe (ASAP) [McEwen et al., 2005]. All the above-mentioned methods have one characteristic

in common, and that is they are all surface ionization methods, and require suitable surface for optimal results. All these methods require a stream of ionizing/ion-desorbing medium directed onto a surface sample in ambient environments from which analyte are ionized and delivered into the mass analyzer [Gross, 2011]. These methods enable detection of various compounds on suitable surfaces and exposing the sample to the ionization region without damaging it. This makes these methods suitable for analysis of biological molecules and tissue cells [Gross, 2011; Cooks et al., 2011].

Desorption electrospray ionization mass spectrometry is an ambient ionization technique that is widely used for surface sampling, high throughput analysis and chemical imaging [Badu-Tawiah and Cooks, 2010]. DESI allows ambient mass spectrometry analysis where the sample is fully accessible and can be manipulated at atmospheric condition/pressure. DESI-MS was developed in the lab of Professor R. Graham Cook in 2004 [Takats et al., 2004]. DESI is characterized by its high speed, due to no sample preparation. It is a soft ionization technique, which produces less fragmentation. It can be performed in both positive and negative ionization modes. Due to these characteristics, DESI can be used to analyze a wide range of compounds from small to large molecules, polar, non-polar and ionic compounds. It is applicable to solids, liquid samples and frozen solutions [Talaty et al., 2005]. DESI can detect low molecular weight organic compounds and also large biological molecules. This is owing to the ionization technique in DESI, which is a combination of both electrospray and desorption ionization [Takats et al., 2005].

DESI-MS has found application in wide range of fields such as biomedical, pharmaceutical and forensics. DESI as been used for high throughput analysis of

pharmaceutical tablets, where samples are analyzed at a rapid rate using a moving belt and selecting the speed. Sampling was performed at range of 0.1-2.67 samples/sec [Chen et al., 2005]. DESI was used for *in vivo* analysis of plant tissue showing variety of alkaloids and their distribution in the plant tissue. Different plants were investigated and the extent of the alkaloids present in each was judge by the signal intensity [Talaty et al., 2005]. Additionally, DESI was used as a form of pharmacokinetics, and drug metabolite analysis in blood and other biological fluids. The biological fluids can be directly analyzed by DESI as a dried spot on a suitable substrate [Takats et al., 2005]. Moreover, DESI has been used in analysis of living tissue, whereby an antihistamine drug Loratadine was detected directly from the finger of a person after ingestion of the drug [Takats et al., 2004].

Also it has been found that the urine of mice can be used to distinguish their different disease states by DESI analysis [Chen et al., 2006]. Metabolites detected by these DESI measurements were compared to that of NMR analysis for both test mice with tumors and healthy mice. It was found that some of these metabolites that are involved in important metabolic enzyme pathway, i.e., citric, acetic and lactic acid, were decreased from the tumor mice to the healthy mice [Chen et al., 2006]. Forensic application of DESI includes identification of toxic compounds, chemical warfare, and explosives. Identification of several explosives by DESI-MS has been published. This includes trinitrotoluene (TNT), hexahydrotrinitro-1,3,5-triazine (RDX) and many more. DESI-MS can also detect traces of the explosives in variety of surfaces [Cotte-rodriguez et al., 2005]. Reactive DESI analysis for chemical selectivity was employed for specific reaction. For example, the formation of complex ions (enzyme-substrate) by doping the

spray solvent with the appropriate substrate was achieved [Takats et al., 2004]. DESI has also been used for *in vivo* experiments, whereby trace amount of explosives were directly detected from the subjects fingerprint [Justes, et al., 2007]. DESI was also used for forensic analysis of chemical compounds found in condoms. Traces elements and their analytical performance were compared, for cases of sexual assault [Mirabelli et al., 2015]. Absence of sample preparation gives advantages in terms of sample preservation, reduced contamination and allowing for successive analysis to be performed on the same samples [Mirabelli et al., 2015].

Biomedical application of DESI involves imaging of biological tissues [Wu et al., 2013]. DESI imaging provided not only the molecular identity of analyte on the surface, but also spatial distribution and amount of analyte present in the sample. Recent research on DESI analysis and applications are largely focused on DESI imaging. This is of high interest because it can provide chemical and spatial information as well as visualization of chemical components distribution in two-dimensions, i.e., as images [Ifa et al., 2011; Wu, et al., 2013]. DESI and other probe electrospray ionization techniques have been used in human cancer tissue imaging and diagnosis [Ifa and Eberlin, 2016]. It has been use for imaging of different biological tissues, rat brain [Wiseman et al., 2006], dog bladder [Dill et al., 2009], and human brain and bladder [Dill et al., 2011; Eberlin and Dill et al., 2010]. Lipid profile in biological specimens can serve as biomarkers to diseases. Therefore DESI-MS imaging of lipids can serve as possible diagnostic tool for tumorous cancers [Wu et al., 2013]. The difference in lipid composition of tumorous and diseases tissues were obtained and provided a better understanding for diagnosis purpose. It was reported that there was higher level of sphingomyelin in the cancerous portion of

human-liver tissues, compare to that of the healthy tissues. And this is due to the activity of the sphingomyelinase enzyme present in the healthy cells to lower sphingomyelin concentrations [Wiseman et al., 2005]. There is ongoing research on addressing issues of sensitivity, compound-specific ionization, effects of solvent composition and surface of interrogation on desorption/ionization efficiency. Insight into these experimental variables can improve DESI-based techniques, reproducibility, and allow quantitative information to be obtained.

2.2 Improving capacity of desorption electrospray ionization mass spectrometry

Success in DESI-MS application depends on understanding the desorption/ionization mechanism, which is an active area of investigation. Several distinct processes thus far have been identified. This include droplet pickup of analyte molecule from the surface by charged solvent droplets (Fig 2.1), heterogeneous charge transfer between gas-phase ion and a surface molecular species followed by desorption of the surface derive ion, and desorption of neutral surface species followed by ionization through gas-phase ion/ molecular reaction [Takats et al., 2004; Takats and Wisemen et al., 2005]. In DESI, the desorption and ionization mechanism is critically dependent on the interaction of the electrospray solvent droplet with the surface of interest (see Fig 2.1). It was demonstrated that the DESI desorption/ionization mechanism changes for different analytes, substrates and spray solvents combinations [Takats and Wisemen et al., 2005].

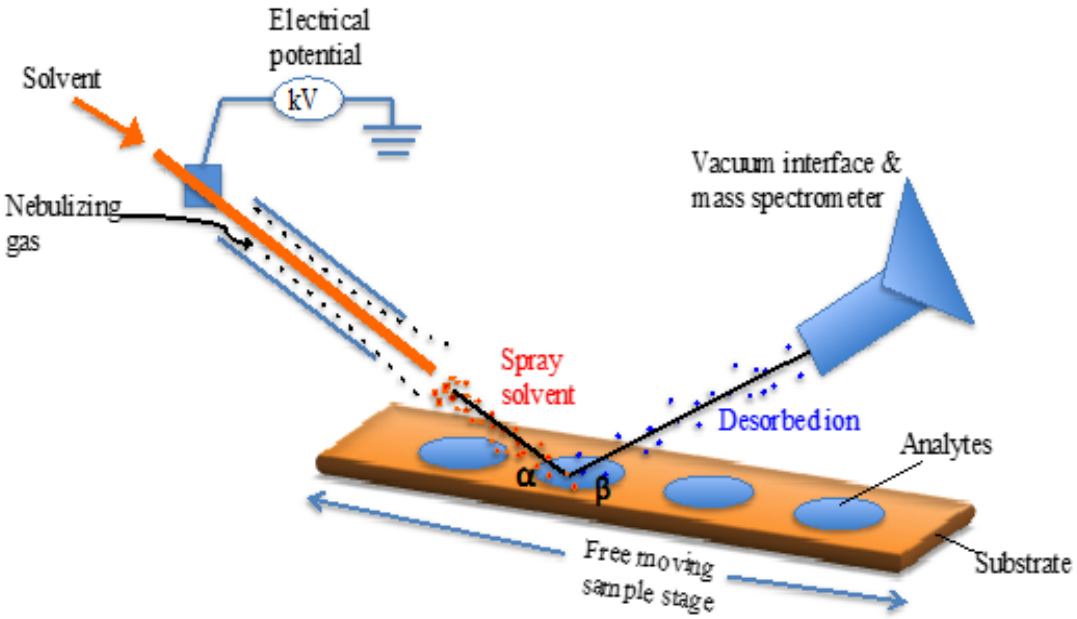

Figure 2.1: Schematic diagram of desorption electrospray ionization (DESI) illustrating the sprayer assembly, and the free moving sample stage (note that only one of the three motion is shown). Indicated is the sprayer angle (α) and the desorption angle (β). Also visible is the vacuum interface of the mass spectrometer and the power supply used to apply a voltage to the spray solvent outlet, adapted from [Cooks, 2006]

The spray solvent chosen plays a key role in the dissolution of the analyte, thereby affecting DESI efficiency. In most DESI experiment, polar protic solvents are typically used regardless of the polarity of the analyte [Ifa et al., 2010]. These solvents are suitable to stabilize the charge of the analyte in the course of solvent evaporation, but may not be best for dissolution of some analytes [Badu-Tawiah et al., 2010]. It was observed that

organic solvent to water ratio of the electrospray mixture affects the erosion diameter i.e., the area wetted by the spray and solubility of analyte. The spray mixture property is also highly dependent on the type of surface employed. The use of higher organic solvent volume fraction in the electrospray lead to decrease in DESI erosion diameter effectively increases wettability and improved DESI efficiency [Green et al., 2010]. Reagents, such as NaCl, HCl, and boric acid, can be added to the spray solvent and can be used for modification of the analyte allowing successful analysis [Ifa et al., 2010; Cotte-Rodrigues et al., 2005]. These are called reactive DESI analysis, whereby addition of reagent to the spray solvent provides specificity, selectivity and improves sample analysis. This is useful for DESI analysis of non-polar analytes like cholesterol and anabolic steroids, which are normally less efficiently desorbed and ionized [Ifa et al., 2010]. For example, when betaine aldehyde is added to the spray solvent strong signals for cholesterol derivative in tissue section analysis are detected. In the absence of this solute, no signal is observed, when for instance typical methanol/water was used as the spray solvent [Wu et al., 2009].

Another example of the usefulness of adding solutes to the spray is for DESI analysis of explosives. In this particular case, the signal was greatly improved by adding NaCl to the spray solvent, which led to the formation of easily detectable explosive salt adducts [Cotte-Rodrigues et al., 2005]. Furthermore, it was reported that addition of surfactant to DESI spray solvent can increase sensitivity and improves limit of detection for food chemicals, and pharmaceuticals. The effect was deduced to be the result of reduced surface tension due to the presence of the surfactants [Badu-Tawiah et al., 2010]. The dissolution of the analyte in the charged microdroplets or thin film of the spray

solvent is essential for the success of DESI analysis. The charged nature of the spray solvent plays a role in the speed of dissolution and, hence, in the effectiveness of the process. It is of interest that the nature of the spray solvent, i.e., added reagents, can enhance ionization and modify analyte for effective analysis [Ifa et al., 2010].

The surface on which the sample is being analyzed by DESI is crucial for ionization of the sample. The chemical composition and the texture of surface affect the ionization process. This occurs by affecting the effective size of crystallization of the analyte deposited on the surface [Takats et al., 2005]. Surfaces with lower affinity to the analyte often display high sensitivity due to easier desorption/ionization of the analyte from the surface. Also of importance, is the electrical conductivity of the surface, which may lead to neutralization of the charge particles and impede the DESI process [Gross, 2011]. Insulating the surface or applying potential to the conductive surface can solve this problem, the potential must be lower than the one applied to the sprayer. Lastly the roughness of the surface also has an effect on ionization efficiency. The roughness was found to increase signal stability, ionization efficiency, and reproducibility [Takats et al., 2005]. It is proposed that the rough surface acts as a barrier for the impacting spray solvent, thereby preventing 'splashing of solvent', whereby samples are promptly removed from the surface by the spray. This effect, which occurs in smooth surfaces generally results in an unstable signal as the spray moves over the sample spot [Badu-Tawiah et al., 2010; Schwab et al., 2014]. Rough surfaces also tend to prevent the "coffee-ring effects" observed on a smooth surface after the analyte spot was sprayed [Douglass et al., 2012]. Volny et al. has suggested that surface energy (wettability) is an important factor controlling droplet behavior on the surface, thereby proposing that

hydrophobic materials have the potential to be excellent DESI substrates [Volny et al., 2008]

DESI analysis can be performed directly from the surface to be analyzed without sample pre-treatment. It has been applied for the analysis of explosives from variety of common surfaces that can be collected from airline passengers and their belongings, such as glass, paper, metal, plastics, cotton swabs [Takats and Cotte-rodriguez et al., 2005; Cotte-rodriguez et al., 2005]. Other surfaces investigated for DESI analysis includes ultra-thin layer chromatography (UTLC) plates, glass slides, tape, polytetrafluoroethylene (PTFE) and polymethylmethacrylate (PMMA). UTLC plates are reported to be useful for the separation of complex mixture prior to detection of analyte by DESI-MS [Kauppila et al., 2006]. It was observed that the use of nanoporous alumina as surface for DESI analysis offers high ion signal intensity, increase peptide detection, improved limit of detection as compared to PMMA, PTFE and glass substrates [Sen et al., 2008].

A big advantage of DESI analysis is its application for imaging of biological molecules. Imaging mass spectrometry (IMS) is becoming widely accepted and a popular tool in scientific research for the detection and identification of a broad range of molecules. This is due to its high specificity, high speed of analysis and high sensitivity [Mcdonnell & Heeren 2007; Wu et al., 2013]. DESI-MS imaging provides chemical and spatial information of a given sample. The capability of DESI-MS imaging of biological tissue has been demonstrated in many studies [Dill et al., 2011; Eberlin and Dill et al., 2010, 2009]. However technical challenges remain, in improving sensitivity, reproducibility, sample preservation and the resolution of the DESI-MS image. All these are affected by the geometry of the DESI ion source [Bennet et al., 2013] and the spray

solvent [Eberlin et al., 2011]. Thus far, imaging of biological tissues, i.e., rat brain tissue, involves two important protocols, which are tissue sectioning and DESI geometric parameter optimization. A frozen tissue is cryosectioned onto a suitable substrate, and it is then imaged. It is crucial that the geometric parameters are kept constant for successful analysis. In collaboration with the group of Dr. Ifa (York University) we are using porous silicon with different pore sizes, and porous silicon facile surface modification as substrates for DESI-MS. The modified porous silicon surfaces will be use to develop a methodology to optimize DESI-MS imaging of biological molecules.

Porous silicon is an interconnected network of voids in crystalline silicon and it is generated by etching of a crystalline silicon wafer [Sailor, 2012]. Uhlirs discovered porous silicon in 1956 while performing electrochemical etching of silicon at Bell laboratory [Uhlirs, 1956]. Interest in porous silicon grew in the 1970s and 1980s with its application in spectroscopic studies due to its high surface area [Sailor, 2012; Dillon et al., 1990]. The discovery of the photoluminescence properties of porous silicon in the 1990s lead to work focused on optoelectronic switches and lasers [Sailor, 2012]. Later, Canham et al. launched the use of porous silicon for optoelectronic applications, i.e., silicon base light emitting diode, and as an optical switch modulating and detecting light [Canham et al., 1996].

However, due to its instability and degradation over time, owing to desorption and adsorption of various chemical compounds, its application in optoelectronics did not amount to much. Other applications of porous silicon include its use as support for growth of single crystal films of other semiconductors, such as PbS and PbTe [Levchenko et al., 1999; Zimin et al., 1999]. As well as applications in the fabrication of

silicon dioxide micro needles for use as electrodes, the fabrication of silicon nanowires for use as solar cells, and lithium ion batteries [Korotchenkov, 2016; Qu et al., 2011; Ge et al., 2012].

Much research on the changes and effect on photoluminescence of porous silicon under different environmental conditions has also been published [Anderson et al., 1990, Blackwood and Akber, 2006]. This research is based on the idea that pore filing and adsorption of molecules on porous silicon strongly affects its various properties, i.e., photoluminescence intensity, conductivity, electrical properties, reflectance coefficient, IR absorption, and resonance frequency of Fabry-pérot interference; allowing to tune the material's properties for a broad range of applications [Korotcenkov and Cho, 2010]. However, one of porous silicon's main application area is as sensors. This is not surprising since porous silicon possesses a high surface area (ca. 200-1000m^2/cm^3), enhanced adsorption effects and facile surface chemistry [Korotcenkov and Cho, 2010]. It use has been demonstrated as biological, gas, electrochemical, mechanical and humidity sensors [Harraz, 2014]. Also, these sensors can be integrated into electronics and used for building sensing arrays necessary for environmental monitoring and laboratory testing, process control, chemical warfare, biochemistry and medicine [Gole et al., 2000; Korotchenkov, 2016].

The unique characteristics of porous silicon, i.e., large surface area, controllable pore size, convenient surface chemistry and biocompatibility also inspired it application in many biological and biomedical base research [Sailor, 1997; Collins et al., 2002; Karlsson et al., 2003; Orosco et al., 2009]. This makes it a suitable medium for growth and analysis of biological cells and tissues [Mayne et al 2000; Kingman, 2001; Buckberry

and Bayliss, 1999]. In addition to its other attributes, it low toxicity makes it suitable for use in therapeutic diagnostics and drug delivery [Anglin et al., 2008; Korotchenkov, 2016]. Porous silicon has also been explored as suitable substrate for small and large molecule analysis by desorption/ionization mass spectrometry (DIOS-MS) [Lewis et al, 2003]. The use of functionalized porous silicon substrate in MALDI-MS has been demonstrated earlier by our group for the analysis of selective binding of protein from complex mixtures [Mengistu et al., 2005]. Mengistu et al. created a monolayer of akyl films as functional groups on porous silicon using hydrosililation chemistry. The modified substrates were then employed for the study of selective binding of protein. The idea being that the functional groups could serve as platforms to selectively capture and sequester large molecules, such as proteins, from complex mixtures for identification and enhancement of low abundant biological molecules.

Silylation chemistry on porous silicon was used to provide ultrahigh sensitivity and analyte specificity with DIOS-MS analysis [Trauger et al., 2004]. Kauppila et al. also studied the application of nanoporous silicon as suitable surface for DESI-MS analysis. They reported that by heating up the nanoporous silicon, they were able to improve the limit of detection on the nanoporous silicon for small molecule analytes. In this thesis we fabricated porous silicon with varying pore size as suitable substrates for the analysis of biological molecules using desorption electrospray ionization mass spectrometry. We functionalized the best suited porous silicon surface with 1-decene and heptadecafluoro-1,1,2,2-tetrahydrodecyl trimethoxysilane (HFTHDTMS), producing a hydrophobic porous silicon substrate for enhancement of DESI efficiency.

Chapter Three

Materials and Methods

3.1 Porous Silicon

Porous silicon is solid single crystalline silicon with voids within. Porous silicon can be fabricated from silicon atoms and silicon base material in a bottom-top technique, or from solid crystalline silicon in a top-down technique. We are interested in the latter technique, which is a traditional method whereby porous silicon is created from solid silicon which itself is created from solid silica [Canham, 2014]. Pure crystalline silicon is a semiconductor with grey metallic appearance. The preparation of silicon involves transformation to silane followed by distillation and adsorption and final retransformation to elemental silicon by chemical vapor deposition [Lehmann, 2002]. Silicon is one of the solid elements produced in pure form; however impurities are purposely introduced by doping with other elements to increase the conductivity of the silicon. Doping of crystalline silicon with elements (such as B, Al, Ga, In) produces what is called p-type silicon. While doping with elements (such as P, As, Sb) produce so-called n-type silicon. Single crystalline silicon is commercially available with different doping levels. Silicon as a semiconductor has two charges carries: electron and defect electrons (holes). Crystalline silicon crystals are often shaped like rods and the rods are then cut in very thin wafers. The wafers are carefully oriented and polished to expose particular crystal orientations that are used in the electronic industry. The most common surface orientations are Si(100) and Si(111) [Lehmann, 2002].

3.1.1 Fabrication of porous silicon

Various techniques are available for the fabrication of porous silicon from crystalline solid. These techniques include electrochemical anodization etching, HNO_3/HF vapor etching, stain etching, photo etching, and metal nanoparticle assisted etching (MACE) [Kolansinski, 2005]. HNO_3/HF vapor etching involves exposing the Si substrate to acid vapors derived from HNO_3 and HF. [Ben Jaballah et al., 2004]. Whereas photo etching requires the silicon substrate, typically n-type silicon wafer to be immersed in an etchant solution of HF while under light illumination (typical light sources are Xe or W lamps) through an optical filter that blocks wavelength shorter than 600nm [Xu and Adachi 2006]. With the metal assisted chemical etching methods, the silicon substrate is partly covered with noble metals and is subjected to an etchant composed of HF and an oxidation agent [Huang et al., 2011]. On the other hand, stain etching involves immersing the silicon substrate in HF solution containing some oxidizing agent [Vazsonyi et al., 2001]. However, the most commonly used technique among the ones listed above is the electrochemical anodization etching. Electrochemical anodization etching involves the introduction of the solid Si wafer into an HF containing electrolyte and a current (galvanostatic mode) or potential (potentiostatic mode) is applied between the wafer and a large area metal electrode. Electrochemical etching is most often performed using the galvanostatic mode because this allows for a better control of the applied current and etching time during pore growth and fabrication.

In an electrochemical cell, two electrodes are required. One electrode the cathode, supplies electrons to the solution, while the anode electrode removes electron from the solution. A schematic of electrochemical cell for etching of silicon is shown in Figure

3.1 illustrating a two-electrode cell. The counter electrode (cathode) in the setup is usually platinum, while the crystalline silicon is the working electrode (anode) where the oxidation reaction occurs. A three-electrode electrochemical setup, which then includes a reference electrode, can be use when the measurement of both the current and potential of the electrochemical reaction simultaneously is required [Sailor, 2012]. The electrochemical cell is designed from HF resistance material, i.e., polyvinyl chloride (PVC), polypropylene (PP) and polytetrafluoroethylene (PTFE). The O-ring seal is used to define the silicon area to be exposed to the electrolyte. The O-ring is made from Viton, which is stable in HF. The backside of the sample is accessible for adding an ohmic contact for better conductivity [Canham, 2014].

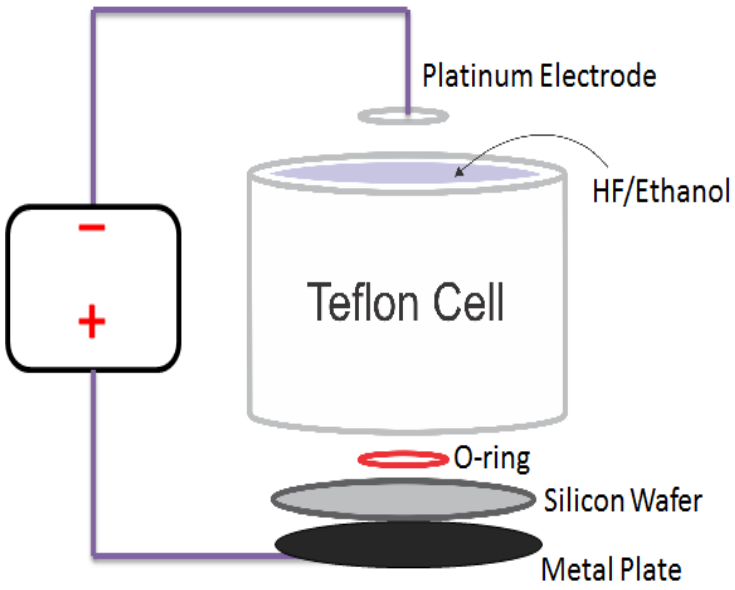

Figure 3.1: Schematic of a two-electrode electrochemical cell used to make porous silicon.

An Ohmic contact is a metal to semiconductor junction, which creates easy charge flow in both direction between the metal and the semiconductor avoiding in this way a resistive contact that could give rise to rectification. When etching silicon a low resistance ohmic contact is required to achieve reproducible pores with uniform morphology [Sailor, 2012]. Commonly used ohmic contacts are aluminum metal foil and metal alloy, such as a gallium indium eutectic mixture. Electrochemical etching of crystalline solid silicon can be performed in aqueous and non-aqueous hydrofluoric acid containing electrolytes. Commercially available hydrofluoric acid comes as a concentrated (40 – 50% HF) aqueous solution. Common electrolytes include mixtures of hydrofluoric acid with ethanol at varying ratios. The presence of ethanol in the electrolyte was observed to reduce the formation of bubbles on the silicon surface leading to a more homogeneous pore formation. Other non-aqueous hydrofluoric acid containing electrolytes have been used in pore formation, i.e. dimethylformamdie (DMF) [Ohji et al., 2000] and acetonitrile [Rieger and Kohl, 1995]. The etching process can be tailored to produce precise pore sizes and morphologies.

3.1.2 Pore Formation Mechanism

The process of controlling pore formation in crystalline silicon involves both physical and chemical factors [Bomchil et al., 1989]. The physical factors include silicon surface orientation, the type and degree of dopant, i.e., sample resistivity. The effect of the wafer orientation on porous silicon formation will be discussed first. The single crystalline silicon can have different reactivity depending on the surface orientation. For example, Si(100) is more reactive and has a higher dissolution rate than Si(111). This is due to the Si(100) surface having atoms that have weaker attachments to the surface and

hence these surface display more reactivity [Zhang, 2004]. This feature of the Si(100) plane also means that pore formation has a high tendency to propagate in the direction perpendicular to the surface [Sailor, 2012]. Other physical factors to consider are the type and degree of dopant, which affects the availability of surface charge carriers. Dopants are a way of increasing the charge carriers in the semiconductor. In p-type silicon, the dopants are usually boron atoms, which have one less electron and donate holes to the silicon lattice when incorporated. While in n-type silicon phosphorous atoms are the dopants, which donate their extra electrons. The doping concentration affects the dissolution rate as well as the size and morphology of the pores formed. The pore size typically increases with increasing doping concentration in p-type whereas, size decreases with increasing doping concentration in n-type silicon samples [Zhang, 2004]. Different pore types and sizes are accessible in electrochemical porous silicon formation. The classification for average pore diameter is as follows; micropores have diameters that are smaller than 10 nm, mesopores have diameters between 10-50 nm, and macropores have diameters larger than 50 nm [Föll et al., 2002]. In this thesis, p-type Si (100) different and doping concentrations were used.

Under anodic conditions, the applied electric field starts the electrochemical process by driving the migration of electron holes to the top of the silicon in the opposite direction of the electron transfer. This leaves the silicon-silicon bond susceptible to nucleophilic attack by the fluoride ions present in the electrolyte. In Figure 3.2 the typical current versus potential curve for a p-type silicon sample in an HF solution is shown. This curve illustrates an exponential increase in current with increase in potential. The current then continues to increase and reaches a maximum before reaching a steady-state

current [Harraz, 2014; Zhang, 2004; Sailor 2012]. Pore formation occurs at low potential, in the exponential regime, i.e., within the pore formation region (I) in Fig. 3.2. Within this region, hydrogen evolution also happens and small bubble formation can be noticed. At high potential, silicon electropolishing (region (III) in Fig. 3.2) takes place, causing dissolution of silicon atoms without pore formation resulting in a smooth surface. The transition region labeled (II) in Fig. 3.2 is the region where pore formation and electropolishing compete [Harraz 2014]. It is important to mention that the current vs. potential curve varies slightly with HF concentration, doping-type and doping concentration [Zhang 2004].

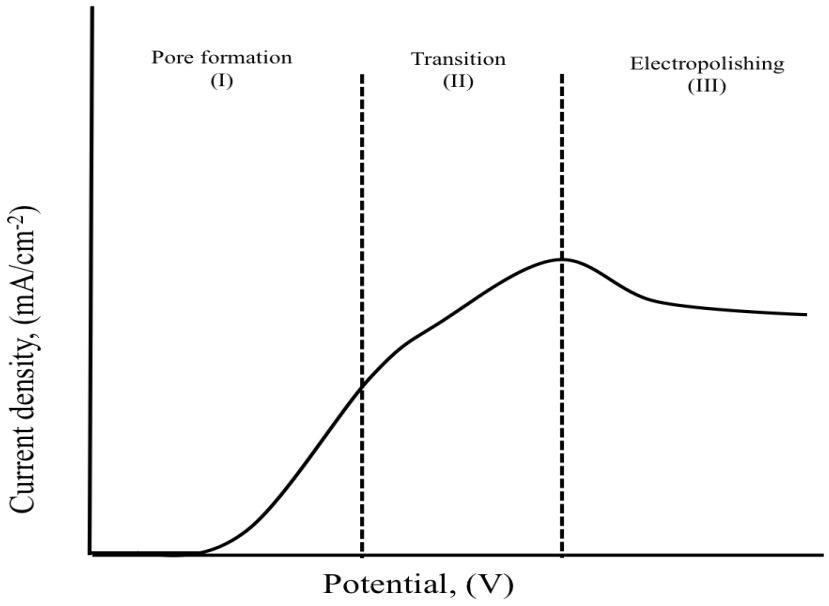

Figure 3.2: Typical anodic current versus potential curve measured on a p- type silicon in a HF solution.

Electrochemical reaction of silicon system in HF containing electrolyte can proceed by a two-electron or four-electron oxidation processes, following equation 3.1 and 3.2 respectively.

$$Si + 6F^- + 2H^+ + 2h^+ \rightarrow SiF_6{}^{2-} + H_2 \quad (3.1)$$

$$Si + 6F^- + 4h^+ \rightarrow SiF_6{}^{2-} \quad (3.2)$$

The reaction in equation 3.1 is the main half reaction governing pore formation of silicon surface at lower applied potential. Conversely, the four-electron process in equation 3.2 dominates when there is lack of fluoride ions at the surface to remove the silicon atoms, which results in electropolishing of the silicon wafer [Sailor 2012]. Pore formation therefore requires dissolving silicon atoms with fluoride ions in aqueous HF electrolyte, leading to formation of stronger Si-F bonds. The silicon atoms dissolves as hexafluoride ion (SiF_6^{2-}) following equation 3.1, and is a stable ion and soluble in water [Sailor, 2012]. As it is etched Si-H bonds passivates the silicon surface because the competing Si-F bonds are highly reactive due to their high electronegativity; consequently pores of silicon surface are hydride terminated. In general, porous silicon formation results from inhomogeneous dissolution of silicon by HF [Kumar and Huber, 2007].

Pore formation also depend on the different parameters such doping, electrolyte and anodization etching conditions. Many mechanism of pore formation have been developed since the discovery of porous silicon. Beale et al. proposed that the material in the porous silicon is depleted of carriers and the presence of a depletion layer is

responsible for current localization at the pore tips where the fields are intensified [Beale et al., 1985]. Smith et al. described the morphology of porous silicon on the hypothesis that the rate of pore growth is limited by the diffusion of holes to the growing pore tip [Smith and Collins, 1992; Smith et al., 1988]. Unagami postulated that that formation of porous silicon is promoted by the deposition of a passive silicic acid on the pore walls resulting in the preferential dissolution at the pore tips [Unagami, 1980]. Alternatively, Parkhutik et al. suggested that a passive film composed of silicon fluoride and silicon oxide exists between the porous silicon and the silicon substrate and that the formation of porous silicon is similar to that of porous alumina [Parkhutik et al., 1983]. By the end of 1980s, Zhang et al. described formation of porous silicon on all types of substrate in terms of current density and HF concentration [Zhang et al, 1989, 2004]. However, the most widely accepted models are the current burst model (CBM) and space charge region model (SCR). In the CBM model, the current mostly flows homogeneously through the Si/HF solution interface both spatially and temporally. Direct dissolution of Si starts the current burst flow, followed by oxidation. At a certain oxide passivation, the current flow stops, consequently the oxide is chemically dissolved. As long as the oxide layer is sufficiently dissolved the cycle repeats, resulting in pore formation [Harraz, 2014; Föll et al., 2002]. In the SCR model, the formation of hydrogen-terminated space charge region acts as the passivation layer and leads to pore formation [Lehmann, 2002].

Different pore diameters are accessible in porous silicon that is a result of different pore formation mechanisms. Micropores are obtained from moderately/low doped p-type silicon, using large HF concentrations. It was recorded that several mechanism are at play in the pore formation. The crystallographic face of Si(100) as

described above is more reactive, because it contains strained Si-H bonds that are more prone to dissolution, in comparison to the Si(111) crystallographic face. Also at play is the high radius of curvature at the tip of the pore that generated a region of enhances electric field that attracts valence band holes [Sailor, 2012; Zhang, 1991]. The increased band gap from quantum confinements excludes the valence band holes from walls of the porous silicon leading to depletion of carries, creating a depletion region and thus stopping the dissolution of silicon during anodization [Sailor 2012; Lehmann and Gosele, 1991]. Mesopores are formed from highly doped p-type silicon wafers. With increase doping there is an increase in electric field strength and a decrease in the width of the depletion region. This, in turn, enables charge carriers to pass through the space charge region (SCR) by band-to-band tunneling [Lehmann, 2002]. Lastly macropores silicon is formed from low-doped p-type and n-type silicon wafers. The formation mechanism that predominates for these samples is an increase in the width of the depletion region/SCR, which increases with decrease dopant density [Sailor, 2012].

There are common general shared features in the mechanism of pore formation for all type of silicon wafers, pore diameter and morphology. These features are: pore nucleates uniformly and with no particular order on the silicon surface except, if the silicon wafer have been pre-patterned. The pore walls become passivated leading to dissolution of silicon primary at the porous silicon/ crystalline silicon substrate interface. Once formed the pores do not redistribute or reconstruct. All samples contain a distribution of pore diameter rather than a single pore size. Existence of mobile charge carriers is a prerequisite for pore formation. A surface region depleted of charge carriers is formed at the silicon/electrolyte interface [Sailor, 2012; Bisi et al., 2000].

3.1.3 Functionalization of porous silicon

The surface chemistry of porous silicon was developed to minimize oxidation reaction of silicon atoms. Oxidation greatly limits porous silicon application as optical biosensors and as suitable substrate for biomolecule analysis [Dancil et al., 1999]. However, there are applications of porous silicon that utilizes it oxidation reaction [Anglin et al., 2008]. As discussed earlier, porous silicon is terminated with hydride when the etching process is completed. However, this surface is unstable and highly reactive. Hence, to increase its surface stability, different surface chemistries have been performed. In this thesis, we will focus on reactions such as oxidation, hydrosilylation and silanol chemistry [Sailor, 2012]. The introduction of carbon directly bonded to silicon yields highly stable porous silicon surface. Porous silicon with Si-C bonds has greater kinetic stability than oxidized porous silicon, due to the low electronegativity of the carbon [Sailor, 2012].

The most commonly used reaction involves the introduction of Si-C bond at the surface of porous silicon using hydrosilylation reactions, as shown in Figure 3.3 below. Hydrosilylation involves the reaction of the unsaturated carbon-carbon bond in alkene or alkyne with the hydrogen terminated silicon. The multiple bonds are usually the terminal bonds of the hydrocarbon chain. Hydrosilylation reaction has been promoted through applying heat [Boukherroub et al., 2002], light [Stewart and Buriak, 1998] mechanical scribing [Niederhauser et al., 2002] and Lewis acid catalysis [Buriak and Allen, 1998]. In this thesis, thermal hydrosilylation was utilized for functionalization of porous silicon with 1-decene. This requires freshly etched porous silicon terminated with hydrogen atoms, and it is performed using a Schlenk line. The Schlenk reaction vessel is

continuously purged with dried argon gas, this prevents oxygen or water from interfering with the surface reaction.

Figure 3.3: Representation of hydrosilylation reaction for introducing Si-C bond to hydrogen terminated porous silicon

Porous silicon is prone to air or water oxidation but, once oxidized, silicon is quite stable. Therefore to produce a stable surface, different chemical and electrochemical processes are used to oxidize porous silicon. Some oxidation method includes: UV/ozone oxidation at room temperature [Dancil et al., 1999], electrochemical oxidation [Letant et al., 2000], organic species oxidation [Boukherroub et al., 2000], thermal annealing [Ogata et al., 2001] and high pressure vapor annealing [Salhi et al., 2007]. All the above methods require extra setup, additional tools that are not frequently accessible.

In this work, we use the most convenient and commonly used methods for oxidizing porous silicon, namely temperature dependent/thermal oxidation and liquid phase/aqueous oxidation. Thermal oxidation can be performed in air, of with gas–phase oxidants [Korotcenkov and Cho, 2010], this produces relatively stable oxide layer [Petrova-koch et al., 1992]. Atmospheric oxidation at different temperature introduces different quantities of hydroxyl species. High temperature, i.e., 900°C with long oxidation times, is required to completely convert the porous silicon skeleton to silicon

oxide [Sailor, 2012]. Thermal oxidation in a tube furnace allows for a better control of the temperature, i.e., it allows the temperature to be increased gradually in order to reduce the stress in the sample, which could cause surface cracking. Liquid phase oxidation is performed using strong oxidants, such as nitric acid and hydrogen peroxide [Xu et al. 2004; Riikonen, 2012]. Mild oxidants, i.e., dimethyl sulfoxide (DMSO) and benzoquinone, can also be used [Sailor, 2012]. It is known that the oxidation process changes the pore structure slightly by reducing the pore volume, the surface area of the material and the pore diameter. This is due to the volume expansion of the porous silicon as oxygen is inserted between adjacent silicon atoms [Riikonen et al., 2012; Pirasteh et al., 2006].

The oxidized surface of porous silicon can be use to perform further chemistry, such as silanization reactions. This involves the reaction of a silane molecule with a surface hydroxyl group to become covalently bonded to the surface by the transfer of a proton from a surface hydroxyl group to the leaving group, thus eliminating an alcohol in the case of a methoxy or ethoxy silanes, or and HCl molecule in the case of chlorosilanes [Coffiner and Boukherroub, 2016]. The effectiveness of this reaction is dependent on the number of OH groups present on the surface. For this reason, the surface must be oxidized immediately before the silanization reaction. Porous silicon can be made to exhibit super hydrophobic properties. Ressine et al. demonstrated that porous silicon with different wetting properties can be fabricated by tuning the anodization etching conditions [Ressine et al., 2007]. Also, silanization chemistry for the functionalization of porous silicon with 1H,1H,2H,2H- perfluorooctyltrichlorosilane has been shown to improve water repellency of porous silicon. The water contact angle of the functionalized

surface was shown to increase from 115°C to 175°C depending on the surface morphology. The obtained structure showed full mechanical and chemical stability and exhibited no decay in months [Ressine et al., 2007]. The super hydrophobicity of the porous silicon can be utilized for application as suitable substrate for mass spectrometry [Wei et al., 1999]. We fabricated a porous silicon surface exhibiting super hydrophobic properties through the functionalization with heptadecafluoro-1,1,2,2-tetrahydrodecyl trimethoxysilane (HFTHDTMS), as illustrated in Figure 3.4.

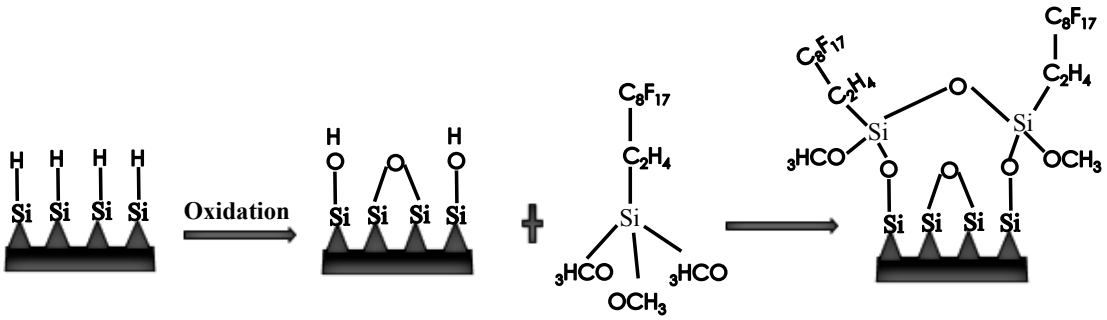

Figure 3.4: Representation of hydrosilylation reaction for introducing Si-C bond to hydrogen terminated porous silicon

3.1.4 Characterization of Porous silicon

In many material science applications, understanding the surface properties and surface chemistry of materials is of great importance. The properties of porous silicon such as pore size and diameter, porosity, and layer thickness can be characterized with various methods. Gas adsorption-desorption technique and gravimetric methods can provide information on pore size, surface area and porosity. Photoluminescence spectroscopy is used for characterization of quantum-confinement of the silicon

nanostructure. However, in this thesis we focus on the general practice that is the use of scanning electron microscopy for quantifying pore size, morphology and layer thickness and characterization of surface chemistry by infrared spectroscopy [Sailor, 2012].

Scanning electron microcopy (SEM) is an essential tool for quantifying pore size, morphology and sample thickness. The advantage of this technique is the high magnification, large depth of focus, great resolution and ease of sample preparation, which is why it is the most commonly used method for porous silicon characterization [Korotcenkov, 2016]. It allows visualization in top-views and cross-section modes. In this thesis secondary electron and backscattered electron microscopy were used for surface characterization of the fabricated porous silicon samples.

Chemical species on porous silicon are typically characterized by Fourier transform infrared (FTIR) spectroscopy. FTIR analysis of porous silicon is acquired at the fingerprint region of the infrared spectrum (4000-200 cm^{-1}) that is characteristic of molecular vibrations of atoms and chemical bonds at the surface [Sailor, 2012]. The FTIR signal of porous silicon is stronger when compared to vibrational spectrum of flat silicon This is due to the large surface area of porous silicon, which place large quantity of the material in the beam path. Porous silicon samples are measured using a diffuse reflectance setup.

3.2 Experimental Conditions

3.2.1 Porous Silicon Etching

To create porous surfaces, silicon crystalline (Virginia semiconductors Inc.) wafers were first etched with a hydrofluoric acid (49%, Sigma aldrich) and anhydrous

ethanol (USP grade commercial alcohol, Sigma Aldrich) mixture in home-made Teflon etch cell galvanostatically using a PAR HD potentiostat-galvanostat. Gallium-indium eutectic was used to create an ohmic contact, and a metal stainless steel for back contact. The counter electrodes for the small and large etch cell are platinum and stainless steel respectively. The freshly etched porous silicon surfaces were washed in ethanol and dried with argon gas.

Experimental small etch cell with diameter of 1.23cm is as follows:

Micropores: 1 Ω cm (100) p-type silicon substrate etching current of 8.3 mA/cm^2 for 30 sec, in 1:1 (HF: Ethanol) solution. The silicon wafers was pre-cleaned with the same etching solution

Mesopores: 1 mΩ cm (100) p-type silicon substrate, etching current of 8.3 mA/cm^2 for 30 sec, in 3:1 (HF: Ethanol) solution. The silicon wafers was pre-cleaned with the same etching solution

Macropores: 15-100 Ω cm (100) p-type silicon substrate, etching current of 8.3 mA/cm^2 for 40 min, in (HF (10%): Ethanol (72%) solution). The silicon wafers was pre-cleaned with the 49% HF solution

All macropores surface were placed in 0.1M KOH to remove micropores with the porous silicon

Experimental conditions for large etch cell with diameter of 3.5cm is as follows:

Micropores: 1 Ω cm (100) p-type silicon substrate etching current of 15 mA/cm^2 for 3 min, in 1:1 (HF: Ethanol)

3.2.2 1-decene functionalization of porous silicon

In order to avoid fast oxidation, freshly etched porous silicon surface, i.e., hydrogen-terminated substrates, were subjected to thermal hydrosilylation without delay. The porous silicon was reacted with 1-decene reagent (Sigma Aldrich, 94%) in schlenk tube under argon leading to the formation of thermally and chemically Si-C bond and creating a hydrophobic surface. The freshly etched porous silicon surface was placed under argon in a schlenk tube containing 1-decene reagent and allowed to react at 150 °C for 3 h. Then, the functionalized surface was rinsed with ethanol (USP grade commercial alcohol, Sigma Aldrich) followed by rinsing with dichloromethane (Caledon, 99.9%). Finally, the sample was dried under a gentle stream of argon (Alphagraz, 99.9%).

3.2.3 Oxidation of porous silicon

Oxidation of porous silicon was performed to produce a stable surface with hydrophilic properties. The reagents HNO_3 (70%) was obtained from Caledon, and H_2O_2 (30%) from Honeywell. The oxidation of the freshly etched porous silicon to produce a hydrophilic surface was performed using thermal oxidation of the freshly etched porous silicon. This oxidation reaction was carried out in a pre-heated beaker at 300 °C for 4 min, in ambient air. Chemical oxidation was performed in oxidizing solution (1:1:5) (H_2O_2 (30%)/HNO_3 (20%)/H_2O) at 80°C for 5 min. The surface was then rinsed with water, and dried with argon gas.

3.2.4 Silylation of porous silicon

This chemical modification process involves the reaction of hydroxyl groups present on the porous silicon surface with heptadecafluoro-1,1,2,2-tetrahydrodecyl trimethoxysilane (HFTHDTMS) (Gelest Inc.). Reagents HNO_3 (70%) was obtained from Caledon, and H_2O_2 (30%) from Honeywell.The oxidation of the freshly etched porous silicon to produce Si-OH groups was performed using thermal oxidation of the freshly etched porous silicon. This oxidation reaction was carried out in a pre-heated beaker at 300 °C for 4 min, in ambient air. Chemical oxidation was performed in oxidizing solution (1:1:5) (H_2O_2 (30%)/HNO_3 (20%)/H_2O) at 80°C for 5 min. Then the oxidized porous silicon surface was exposed to the perfluoro-silane reagent by pipetting 50 μL of the silylating agent solution in ethanol on the sample and allow the reaction to occur at 100 °C for 30 min. The surface was then rinsed with ethanol (USP grade commercial alcohol, Sigma Aldrich)) and dried with argon (Alphagraz, 99.9%).

3.2.5 Scanning Electron Microscopy

Scanning electron microscopy is one of the most widely used instruments for analysis of microstructure morphology and chemical compositions characterization. SEM makes use of an electron gun, to direct focused beam of electrons towards a sample surface. A series of electromagnetic (condenser and objective) lenses act to focus and control the diameter of the incident electron beam. The instrument also contains a series of apertures, which are micro scale holes in metal films that the electron beam passes through and affects the properties of the beam. It also contains the specimen position stage, which controls the (X,Y,Z) position, tilt, rotation and angle of the sample [Zhou et

al., 2007]. The scanning coils are used to control the electron beam for raster scanning of the surface sample. The focused beam hits the surface and interacts with the atoms of the surface producing different electron radiation that can be detected and processed to produce images or spectra.

Two types of electron radiation are detected and used to produce images in scanning electron microscopy; secondary electron and backscattered electron [Zhou et al., 2007; Hofmann et al., 2014]. Secondary electrons are dislodged electrons that emerge from the sample upon interaction of the incident electron beam with the sample. Conversely, backscattered electrons are high-energy electrons that are back scattered at a high angle upon interaction of the incident beam with the atomic nuclei of the sample. The number of detected backscattered electrons is highly dependent on the atomic number of the elements present in the sample. High atomic number atoms are visualized as different contrast in the images produce from backscattered electrons. Other detectors can be coupled to the SEM to obtain and detect other types of electron radiation, i.e., characteristic X-rays (EDX) used for elemental analysis, and cathodeluminsecence used for electronic state analysis [Zhou et al., 2007; Hofmann et al., 2014].

Scanning electron microscopy was used for the characterization of pore diameters, their distribution and their depth. The FEI Quanta 3D Peg is a "dual beam" scanning electron microscope (SEM) that is also equipped with a focused ion beam (FIB) and this instrument was used in this work. SEM images for the pore filling experiments were obtained with an environmental SEM FEI Quanta 250.

3.2.6 Fourier-Transform infrared (FTIR) Spectrometer

FTIR spectrometry makes use of polychromatic light that is emitted into an interferometer. The beam is split into two beams that are reflected back into the point of spit at the interferometer plate. A movable mirror allows the length of both beams to be adjusted and the different between the phases of the two beams as a result of the path length yields an interferogram that has all wavelengths encoded. The beam thus enters the sample compartment where it is either transmitted of reflected off the sample surface depending on the type of analysis being performed [Hofmann et al., 2014]. Transmission mode is the most straightforward and conventional infrared method, whereby absorption of the infrared radiation occurs at a specific wavelength as it pass through the sample. On the other hand, the reflectance mode is used for analysis of samples that are difficult to analyze by transmission mode. Two different approaches can be employed in reflectance mode, namely internal and external reflectance. Internal reflectance measurements can be performed using attenuated total reflectance (ATR), whereby the infrared light passes through a crystal of high optical quality and high refractive index properties [Stuart, 2004]. The infrared beam reflects off the ATR crystal in contact with the sample and forms an evanescent wave that extends into the sample where the absorption of wavelengths occurs. The reflected beam exiting the ATR crystal is detected and used to construct the spectrum.

Also of interest are the external reflectance measurements where two forms of reflectance can occur; specular or diffuse. Specular reflectance tends to occur when the reflectance angle of the radiation is equal to the incidence angle of the beam. Diffuse reflectance spectroscopy (DIRFT) occurs when the radiation that penetrates the sample is

reflected in all directions. The reflected radiation is collected over a wide angle using an ellipsoid or paraboloid mirror and then detected [Stuart, 2004]. DRIFT is ideal for powder and rough samples. Diffuse reflectance and attenuated total reflectance setups can be purchased as accessories that can be inserted into the sample chamber and are available for most commercial FITR spectrometer. A problem that is encounter with FTIR measurement of porous silicon is the Fabry-Pérot interference, that arises from constructive and destructive interferences of the infrared beam in the porous silicon layer. This is observed in the FTIR spectrum as sinusoidal baseline, and can sometimes obscure the peaks of interest [Sailor, 2012]. In this thesis surface chemistry of the fabricated porous silicon was characterized by DRIFT spectroscopy.

Diffuse reflectance FTIR-spectra were recorded for our research with a Thermo Scientific Nicolet 6700 spectrometer equipped with a cricket diffuse reflectance accessory from Harrick scientific Products. Typically 100 scans were acquired per spectrum at resolution 4 cm^{-1}. For freshly etched porous silicon surfaces, a clean untreated Si(100) wafer was used as the reference. For the 1-decene functionalized porous silicon surfaces, the freshly etched porous silicon was used as reference. For sample analyzed by FTIR, etching of Si(100) p-type wafer was performed for 5 min following the etching conditions in section 3.2.1

3.3 DESI-MS Instrumentation and Imaging

The essential aspect of DESI-MS instrumentation involves the ion source, which is comprised of two parts, the solvent sprayer and the surface stage (Fig 3.5). The solvent sprayer is typically constructed from an inner silica capillary inserted in a larger outer capillary tube. The inner capillary tube is usually connected to a stainless steel syringe

which is used to pump the spray solvent. The larger outer capillary tube is connected to the gas tank for transporting the nebulizing gas, typically nitrogen [Venter et al., 2006]. A high voltage of 3-5 kV is applied to the needle of the syringe containing the solvent. The sprayer assembly expels the electrospray onto the sample surface at an incident angle (α) (Fig 3.5). On the sample stage, the desorbed analyte ions are transported away from the sample stage in secondary droplets at an angle (β). The incident angle must be optimized for most DESI analysis, however the reported range is from 35°- 90° [Douglass et al., 2012]. For most DESI experiments, the sprayer to surface distance (d_1) is in the range of 1 to 5 mm [Douglass et al., 2012]. It is also reported that the ideal collection angle (β) of secondary droplets is 10°, and the MS orifice to surface distance (d_2) of 1 mm for most DESI experiments [Takats and Wisemen et al., 2005].

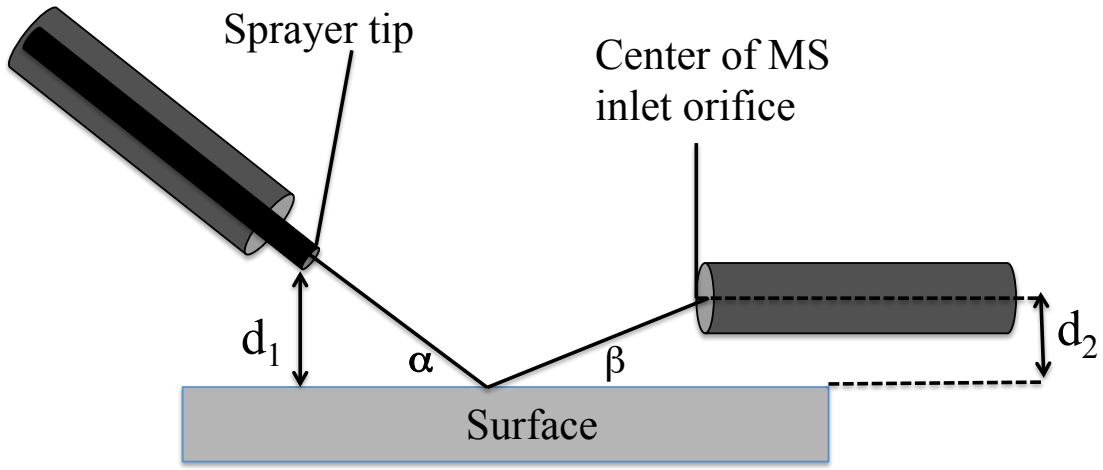

Figure 3.5: Schematic diagram illustrating DESI-MS setup. Indicated is the sprayer angle (α), the collection angle (β, the tip to surface height (d_1) and the MS orifice height (d_2). Adapted from [Takats and Wisemen et al., 2005].

The sample stage can move in 3-dimensions allowing for adjustment of the sprayer to surface distance as well as the surface to mass spectrometer inlet distance. In addition, the 3-dimension moving stage controls the movement of the sample to be analyzed as well as provides the scanning motion of the sample, which is required for DESI mass spectrometry imaging [Takats et al., 2005]. Aspects of the instrumentation that greatly affect the DESI experiment are the nature of the spray solvent, sprayer to surface distance, impact and desorption angles and the type of surface employed. All of these parameters need to be optimized for each DESI experiment to ensure effective desorption/ionization.

Mass spectrometry imaging provides information on the spatial distribution and amount of chemical constituents of a given sample, which can later be process and visualized as a chemical image [Wu et al., 2013]. Imaging mass spectrometry of MALDI has found success in life science for imaging large biomolecules due to its high mass capability [Stoeckli et al., 2001]. MALDI has also been used for pathological studies, i.e., analysis of glioblastoma tissue sections revealing different protein localized in different area of a tumor [Stoeckli et al., 2001]. SIMS, which traditionally was limited to low mass molecular analysis has also found its place in imaging of large biomolecules with higher resolution [Mcdonnell and Heeren, 2007]. Ambient ionization imaging mass spectrometry in which ionization occurs at atmospheric pressure is an advantageous technique compare to those described above, for its does not require sample preparation and matrix addition [Wu et al., 2013]. DESI-MS imaging is a member of the ambient ionization mass spectrometry-imaging group of techniques. DESI-MS imaging allows for

imaging of samples with reduced fragmentation relative to SIMS, and does not require chemical matrix for ionization needed in MALDI [Wiseman et al., 2008].

DESI-MS imaging makes use of the DESI sprayer assembly to raster scan the surface, providing the mass spectral and spatial information of the sample surface pixel by pixel. The product of the sampling rate of the MS and the surface velocity determines the pixel length in the x-direction, whereas the pixel width in the y- direction is defined by the step size of the motion system. Therefore the whole surface of the sample is divided into small areas (pixels) and these areas are scanned individually and sequentially in time. The data of a pixel is normally represented by a single mass spectrum or an average of two or more mass spectra acquired at a specific spot or while continuously rastering the surface with the sprayer [Wu et al., 2013]. The molecular ion image is reconstructed from the collected mass spectra after completion of the experiment [Macdonnell & Heeren, 2007; Wu et al., 2013]. The spatial resolution depends on the spot size, but the spray solvent, velocities, and carryover between pixels can also limit it. For DESI-MS imaging, different solvents have been utilized as the sprayer solvent. Non-aqueous solvent, i.e., methanol (MeOH), dimethylformamide:acetonirtrile (DMF:ACN) and dimethylformamide:ethanol (DMF:EtOH) were shown to provide abundant signal and high quality images for biological tissue. Moreover these solvents were also able to pick up even small protein molecules [Emberlin et al., 2011]. A small spray spot is achieved by adjusting the distance between the spray tip and the substrate, and/or by adjusting the distance between the surface and the inlet of the mass analyzer; both improve the image quality [Wu et al., 2013].

It was reported that a sprayer angle of 52° provides a higher signal intensity, which is ideal for DESI-MS imaging. The typical spatial resolution in DESI is ~200 μm, but it can be reduced to as low as ~40 μm under particular operating conditions [Wu et al., 2013]. It is notable that the signal intensity decreases with an increase in spatial resolution, leading to an increase in the time needed to acquire an image. The general rule in this field is to use the minimum resolution possible to obtain the best information for the sample of interest at a reasonable speed [Wu et al., 2013]. The 2D imaging capabilities of DESI were originally developed with an automatic lab-built moving stage [Wiseman et al., 2006]. 3D models can be constructed from a series of 2D cross-sections images [Wu et al., 2013; Eberlin and Ifa et al., 2010]. The mass analyzer used also has a strong effect on the spectral resolution and detection limits. Several mass analyzers have been used for DESI-MS imaging, such as triple quadruple, orbitrap and FT-ICR. Tandem MS is also used when one wants to obtain the distribution of ions with same nominal mass [Ifa et al., 2009].

3.3.1 DESI Technique

All experiments were conducted using Finnigan LTQ linear ion trap mass spectrometer (Thermo Scientific)) coupled to a lab-built DESI source with a 2D moving stage. The LTQ operating parameters are: a voltage of 5 kV, MS injection time of 150 ms, the automatic gain control (AGC) was turned on, and 2 microscans were summed to create each spectrum. The DESI source conditions are: nitrogen sheath gas pressure of 100 psi; spray solvent was delivered at the flow rate of 3 μl/min; the sprayer to surface distance was 2 mm; the sprayer to surface incident angle was 51°; and the tip to inlet distance was 5-7mm.

3.3.2 Small molecules sample preparation

Stock solutions of propranolol, angiotensin, acetylcholine, testosterone, verapamil, roxithomycin, angiotensin, ibuprofen, and chloramphenicol were purchased from Sigma Aldrich, and diazepam, cocaine, oxycodone from Cerilliant (Round Rock, Texas). The solutions were prepared in deionized water LC-MS grade at concentration of 1 μg/mL and employed for serial dilutions in water providing final concentration of 0.5, 1, 10, and 100 ng/mL. All the spotted samples on the porous silicon surfaces were allowed to dry at room temperature prior to analysis. Methanol was used as spray solvent. The cleaning process was carried out by sonication of all porous and nonporous silicon wafers in methanol and air-drying when used for DESI-MS experiments.

3.3.3 Rat brain tissue sample

Frozen rat brain was sectioned into 20μm thick section using a Shandon Cryotome FE (thermo Fischer Scientific). The tissue slice was mounted onto the functionalized porous silicon surface, and was stored at -40°C. The sample was brought back to room temperature before analysis. DESI sprayer solvent for rat brain tissue imaging was pure methanol.

3.3.4 DESI-MS imaging

All experiments were conducted using Finnigan LTQ linear ion trap mass spectrometer (Thermo Scientific)) coupled to a lab-built DESI source with a 2D moving stage. The LTQ operating parameters are: voltage of 5 kV, MS injection time of 150 ms, the automatic gain control (AGC) was turned off and 2 microscans were summed to

create each spectrum**.** The DESI source conditions are: a nitrogen gas pressure of 100 psi; and the spray solvent was delivered at the flow rate of 5 μL/min. The sprayer to surface distance, inlet to surface distance and the sprayer to surface incident angle were optimized for each surface. The scan range for this experiment was from 200 m/z to 1000 m/z. The image was obtained by continuously scanning the spray across the x-direction and each y-direction step was 200 μm. While scanning the rat brain tissue, 45 lines were analyzed by DESI at a spatial resolution of 200 μm. Ion images were obtained using a lab built software names ImgCreator that converted the mass spectra files into a format that is compatible with Biomap.

Chapter Four

Porous Silicon Characterization Results and Discussion

4.1 SEM Results of Fabricated Porous Silicon

Porous silicon is an attractive material for biological application owing to its high surface area, ease of surface chemistry for attaching biomaterials, and biocompatibility. By tuning the different parameters such as doping, electrolyte and anodization conditions, porous silicon with different pore sizes and depth can be fashioned. Figure 4.1 shows the scanning electron micrographs of the pore morphologies for each of the three investigated freshly etched surfaces. The moderately doped silicon surface (1 Ω cm) etched with 1:1 HF: EtOH was used for the fabrication of the microporous surfaces (see example in Fig 4.1a), these conditions yielded porous surfaces with pore with less than 10 nm in diameter. Highly doped crystalline silicon surfaces (1 mΩ cm) etch with 3:1 HF: EtOH were used for the fabrication of the mesoporous silicon samples (see example in Fig 4.1b). These conditions produced surfaces with pore diameters in the range of 10 to 50 nm. Finally, low-doped silicon surfaces (ca. 15-100 Ω cm) were used to fabricate the macroporous surfaces that yielded pore diameters greater than 50 nm (see example in Fig 4.1c). Other factors affecting the morphology of the pores are the concentration of hydrofluoric acid in the electrolyte, the applied current and the etching time. Therefore, different percentages of HF were used for the formation of the three surfaces investigated. In general, the etching time affects mainly the depth of the pores formed.

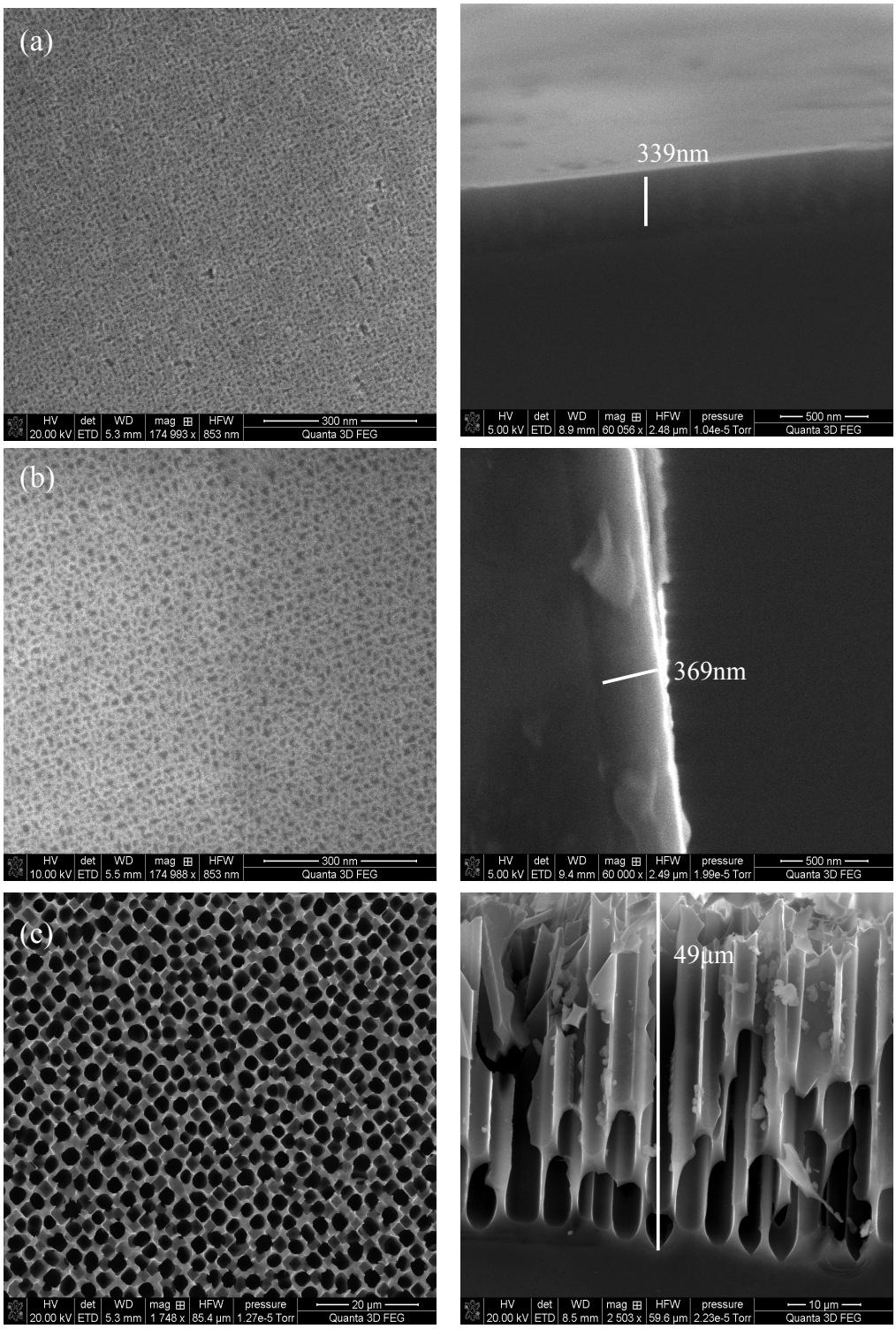

Figure 4.1: Plain and cross-sectional views acquired using SEM of (a) microporous, b) mesoporous, and (c) macroporous silicon films.

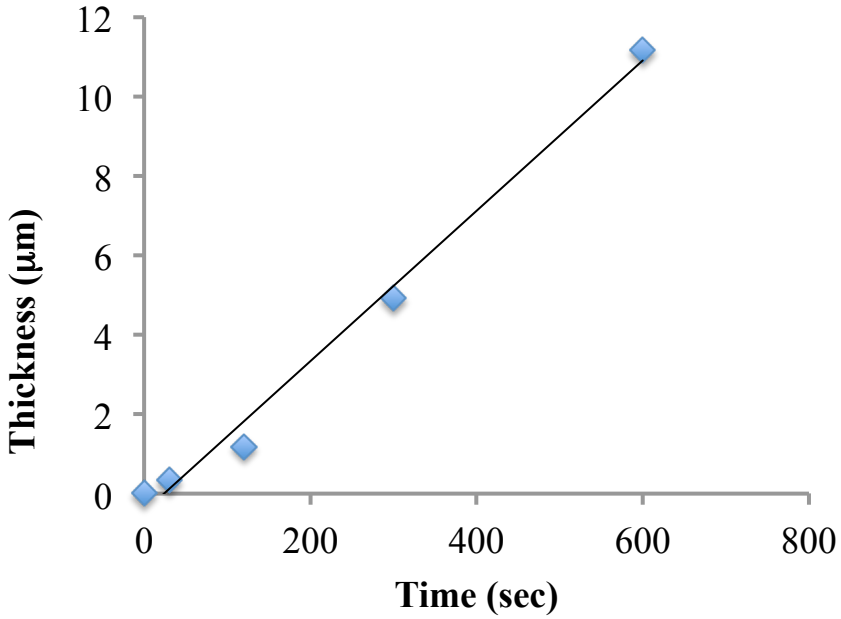

Figure 4.2: Thickness of porous silicon etched at 8.3 mA/cm^2 in (1:1) HF/EtOH mixture solution, as a function of etching time

This was verified in this work and the results are shown in Fig. 4.2. We noticed that increasing the etch time while keeping the current and HF concentration constant, mainly increases the thickness of the porous layer. A linear correlation displaying the thickness enhancement from 0.339 µm to 11.18 µm with an increasing in etching time can be observed (Fig 4.2). Such a trend is in agreement with the literate [Kumar and Huber, 2007]. The corresponding SEM images of the cross-section view of the porous silicon illustrating the difference in thickness of the porous layer for the different etch time (see Fig. 4.3). In this section we have shown that we were able to fabricate porous silicon in a controlled way with different pore sizes and thicknesses. The most reproducible parameters were then used to produce materials with controlled pore sizes for further experiment in this thesis.

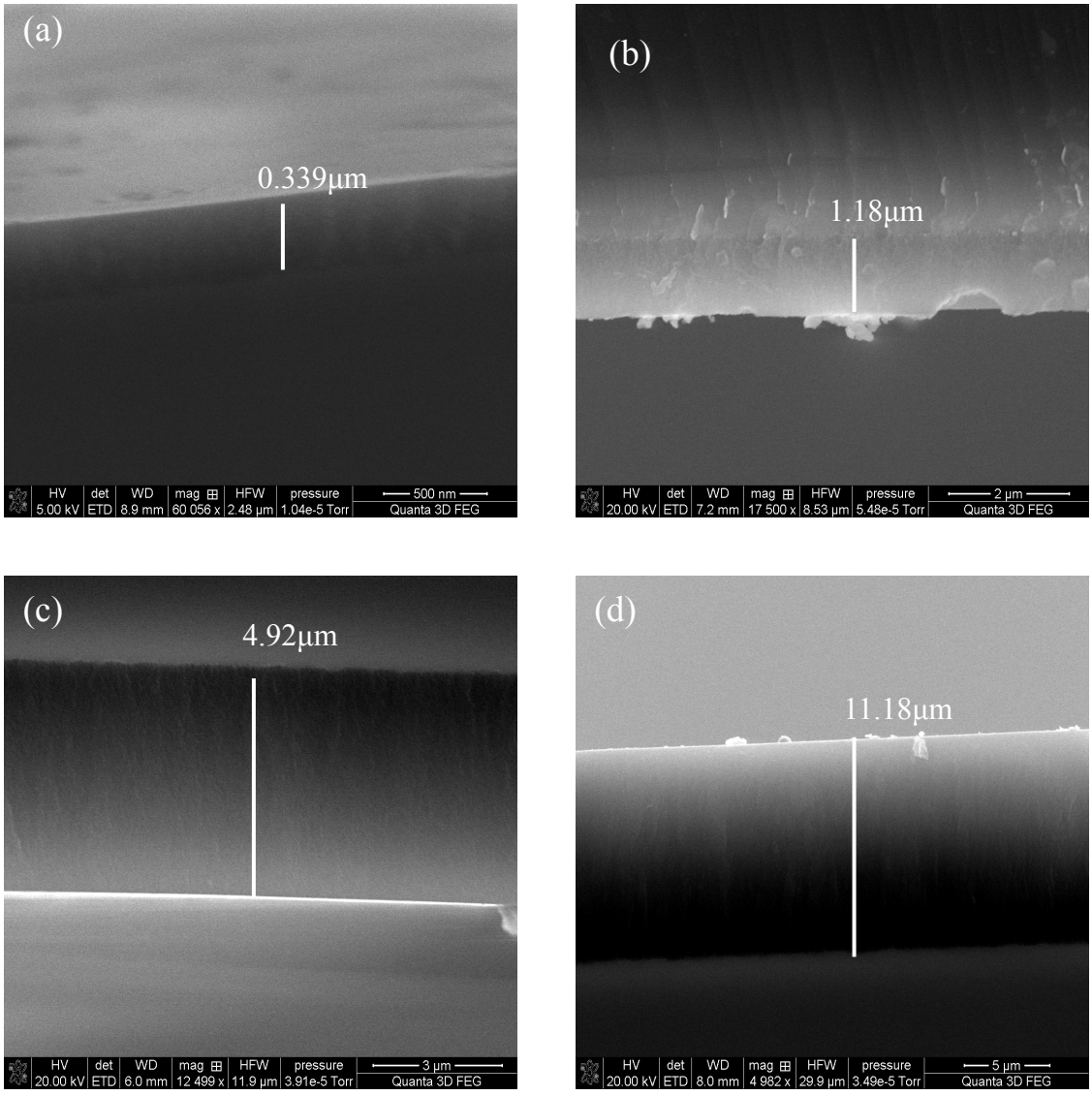

Figure 4.3: Cross-sectional SEM images of micro-porous silicon surface etched in (1:1) (HF:EtOH) at 8.3 mA/cm^2 at different etch timed (a) 30 sec (b) 2 min (c) 5 min and (d) 10 min

4.2 Functionalization of Porous silicon

Freshly etched silicon surfaces are silicon-hydride terminated and exhibit strong hydrophobic properties. However, they are unstable surfaces that are prone to oxidation. A thermal hydrosilylation surface reaction with 1-decene was performed to passivate the investigated porous silicon substrates. This not only provides surface stability towards an aqueous environment but it also produces a more hydrophobic surface of known surface chemistry. This procedure is performed by, first etching the crystalline silicon surface to produce the porous surface; the sample is then rinse with ethanol, and then drying with argon gas. The drying eliminates excess water and ethanol that can also react with Si-H bonds when trapped in the pores. The surface is then placed right away into a schlenk tube containing 1-decene pure reagent. The reagent was purged with argon prior to the addition of the sample and during the reaction. The porous silicon sample is allowed to react with 1-decene for 3 hr at 150ºC. Once the reaction is completed, the surface is rinsed gently with several portions of ethanol and dichloromethane to protect the integrity of the porous structure. The surface is finally dried with argon gas. Once the preparation is completed a highly hydrophobic surface with a dense monolayer of alkyl species is obtained. Diffuse reflectance Fourier transform infrared spectroscopy (DRIFT) was used as a characterization method for the functionalized surfaces.

It is important to note that the spectra background (which is acquired by recording the transmittance of the sample and that of a reference such as porous silicon hydride (see page 35 for details) were not further corrected nor normalized; the waviness of the spectra is due to slight variation in thickness between the sample used to record the background and the sample itself, which could not be avoided. For DRIFT analysis, the

etch time for fabrication of the porous silicon was increased to 5 min. At five minutes, as previously discussed, pore depth increases thus allowing light to penetrate through the surface pores, which in turn improves light absorption and ease of identifying the bonds that are present. In Figure 4.4 is a representative DRIFT-IR spectrum of a freshly etched microporous silicon surface. The obtained FTIR spectrum in Fig. 4.4 shows a transmittance peak at 2080-2190 cm^{-1} characteristics of the Si-H_x bond. The peaks correspond to υSi-H_1 at 2088 cm^{-1}, υSi-H_2 at 2117 cm^{-1}, υSi-H_3 at 2138 cm^{-1}. The Transmittance peaks at 918 $cm^{-1,}$ 634 cm^{-1}, and 698 $cm^{-1}$are representative Si-H_x scissor modes.

In Figure 4.5 is DRIFT-IR spectra of the porous silicon surfaces functionalized with 1-decene. In the 1-decene functionalized surfaces (Fig. 4.5), the FTIR spectra show a transmittance peak at 2854-2960 cm^{-1} characteristics of the carbon-hydrogen bonds. The peaks correspond to alkyl C-H stretch are at ~2856 cm^{-1} and ~ 2927 cm^{-1}, are in agreement with literature values [Mengistu et al., 2005]. Also visible is subtracted Si-H transmittance peak at 2080-2190 cm^{-1} which is shown as inverted peaks. The inverted peak signifies the disappearance of the Si-H bonds and the success of the functionalization, whereby the Si-C bonds have replaced the Si-H bonds. Modification of porous silicon with 1-decene exhibit hydrophobic properties, and Ruminski et al. obtained a contact angle of 119 ±2° for 1-dodecene modified porous silicon surface [Ruminski et al., 2010]. Several methods have been shown to be successful in introduce monolayer of organic groups through Si-C attachment. Boukherroub et al. have shown that thermal hydrosilyation of porous silicon following our method, produces an alkyl modified surface that is robust.

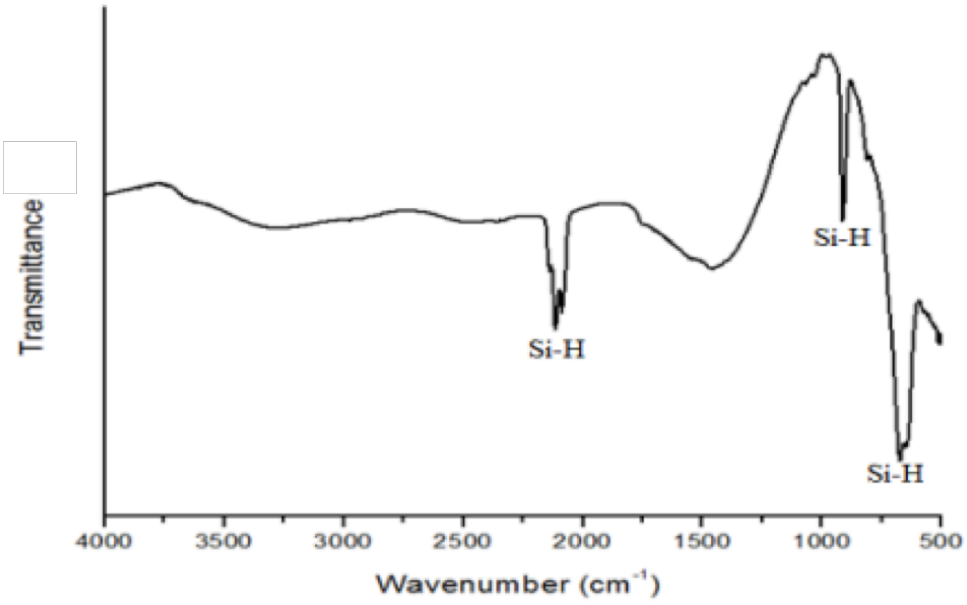

Figure 4.4: DRIFT-IR spectrum of porous silicon Si-H terminated microporous surface, nonporous silicon surface was used as reference background. 100 scans were acquired per spectrum at resolution 4 cm^{-1}. For samples analyzed by DRIFT-IR etching of Si (100) p-type wafer was etched in HF/Ethanol mixture with current density of 8:3 mA/cm for 5 min

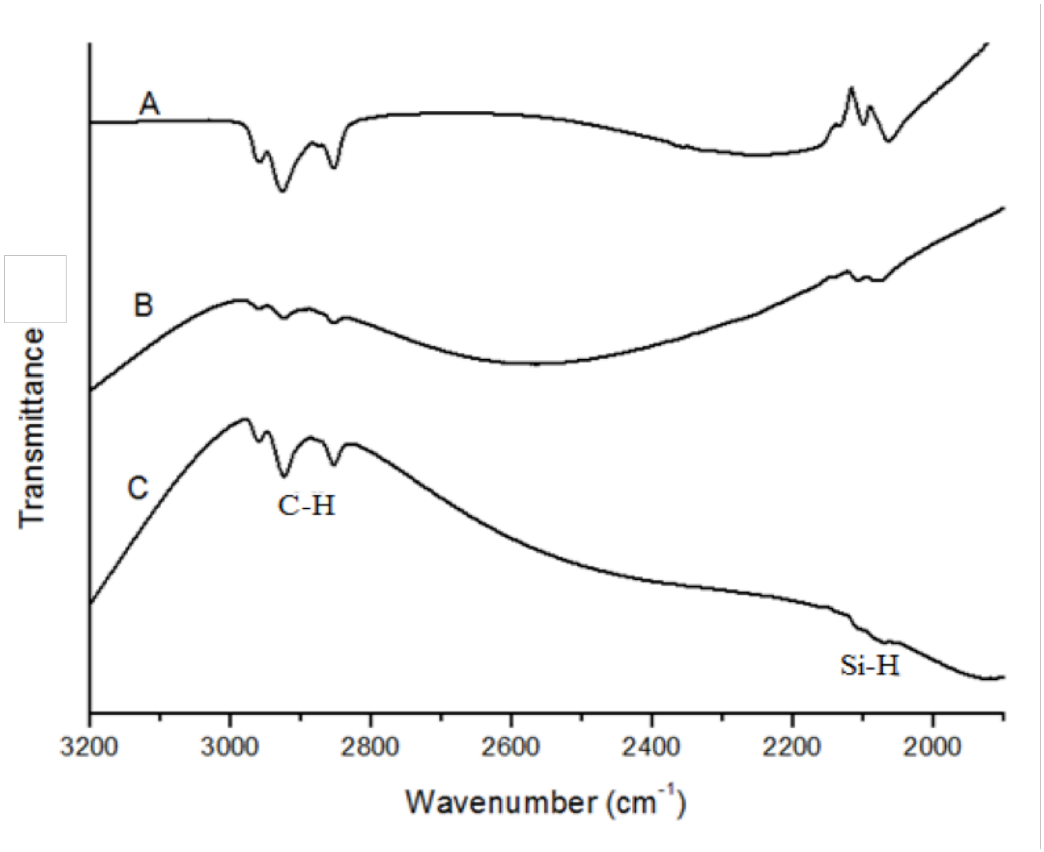

Figure 4.5: Diffuse reflectance FTIR spectra of A) micro-porous, B) macro-porous, and C) meso-porous surfaces functionalized with 1-decene. Porous silicon surface Si-H terminated was used as reference background. 100 scans were acquired per spectrum at resolution 4 cm^{-1}. For samples analyzed by DRIFT-IR etching of Si (100) p-type wafer was etched in HF/Ethanol mixture with current density of 8:3 mA/cm for 5 min

The efficiency of the reaction was determined to be 30-50% depending on the method of preparation of the porous silicon. As well, this group discussed that these method not only allow modification of the Si-H bond terminating the porous silicon surface it also allows for uniform modification of the pores [Boukherroub et al., 2001]. They also demonstrated that the modification of the porous surface did not alter the porous silicon structure of the modified surface. This was confirmed by subjecting the surface to extreme conditions and the result demonstrated the extreme stability of the modified surface to harsh environments. As well, the photoluminescence of the modified surface was preserved and found to be stable during an aging process that could completely destroyed an unfunctionalized H-terminated porous silicon sample [Boukherroub et al., 2001].

The next functionalization performed is with heptadecafluoro-1,1,2,2-tetrahydrodecyl trimethoxysilane (HFTHDTMS) by silanization process (Fig. 3.4). This reagent is known to exhibit high hydrophobic characteristic owing to it high order of fluorinated carbon chains. Functionalization by the silanization process requires available Si-OH bonds, which are attained by oxidation of freshly etched porous silicon. Riikonen et al. explored different methods for oxidation of porous silicon surfaces [Riikonen et al., 2012]. We performed porous silicon oxidation through thermal and aqueous oxidation steps. Firstly, thermal oxidation occurs by heating up the freshly etched porous silicon at 300ºC for 4 min while exposed to atmospheric oxygen. We then continued the oxidation process with aqueous oxidation in an oxidizing solution at 80°C for 5 min. The detailed composition of this solution is given in section 3.3.3. Figure 4.6 is the DRIFT-IR spectrum of the porous silicon surface obtained after the complete oxidation process.

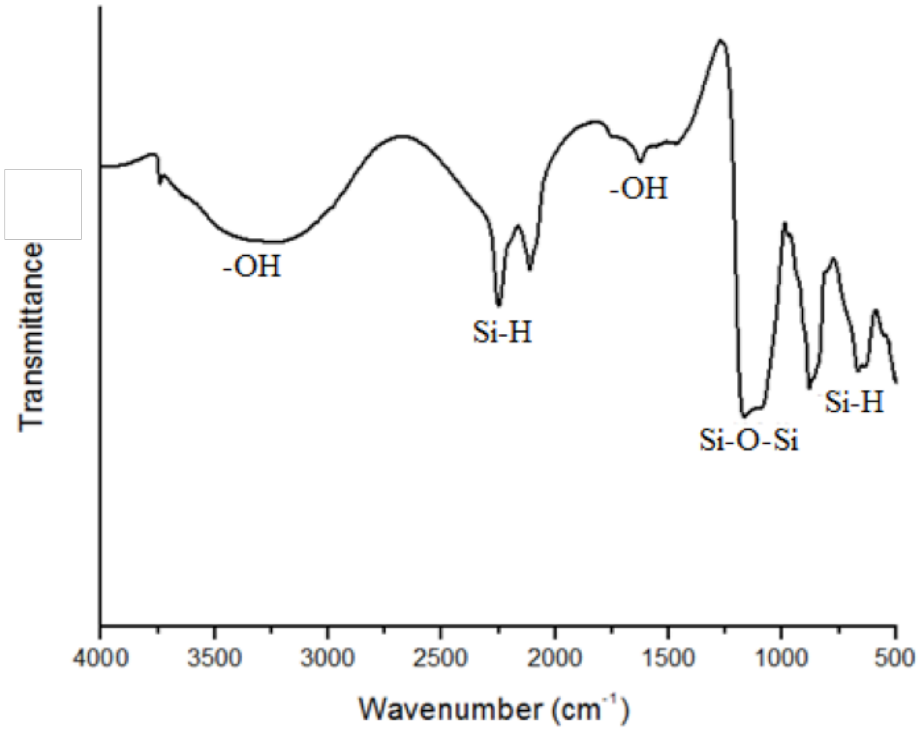

Figure 4.6: Diffuse reflectance FTIR spectrum of oxidized microporous silicon surface. Porous silicon surface Si-H terminated was used as reference background. 100 scans were acquired per spectrum at resolution 4 cm^{-1}. For samples analyzed by DRIFT-IR etching of Si (100) p-type wafer was etched in HF/Ethanol mixture with current density of 8:3 mA/cm for 5 min

The oxidized surface showed strong broad transmittance peak for surface bonded hydroxyl group at Si-OH at 3000-3700 cm^{-1}, a small peak at 3740 cm^{-1} corresponding to surface hydroxyl group, and peak at 1640 cm^{-1} corresponding to the value stated in literature [Riikonen et al., 2012]. Also visible is a strong Si-O-Si peak at 1020 cm^{-1}, and Si-H absorption peaks as labeled in Figure 4.6.

The Si-H peak at 2250 cm^{-1} (Fig 4.6) contains Si-O-Si backbone within the porous silicon layer. Functionalization with fluoroalkyl silane was performed by exposing the oxidized porous surface of the HFTHDTMS reagent solution. In Figure 4.7 the DRIFT-IR spectra of microporous surface functionalized with the fluoroalkyl silane obtained after the modification procedure is shown. The transmittance peak of 600 to 1300 cm^{-1} represent characteristics peaks for the fluoroalkyl surface modifier.

The peaks at 1250, 1000, 704 and 623cm^{-1} represent C-F_2 and C-F_3 bonds, these values correspond to that listed in literature for a similar nanoparticle modification [Brassard et al., 2012]. The broad transmittance peak at 1150-1200cm^{-1} is associated to the formation of the Si-O-C bond. Other visible peaks are at ca. 1124 cm^{-1} and 895cm^{-1} representing the Si-O-Si bonds, and C-H bonds, respectively. Porous silicon surfaces modified with fluorocarbon are known to exhibit super hydrophobic properties with water contact angle greater than 150° [Ressine et al., 2008; Cao et al., 2008].

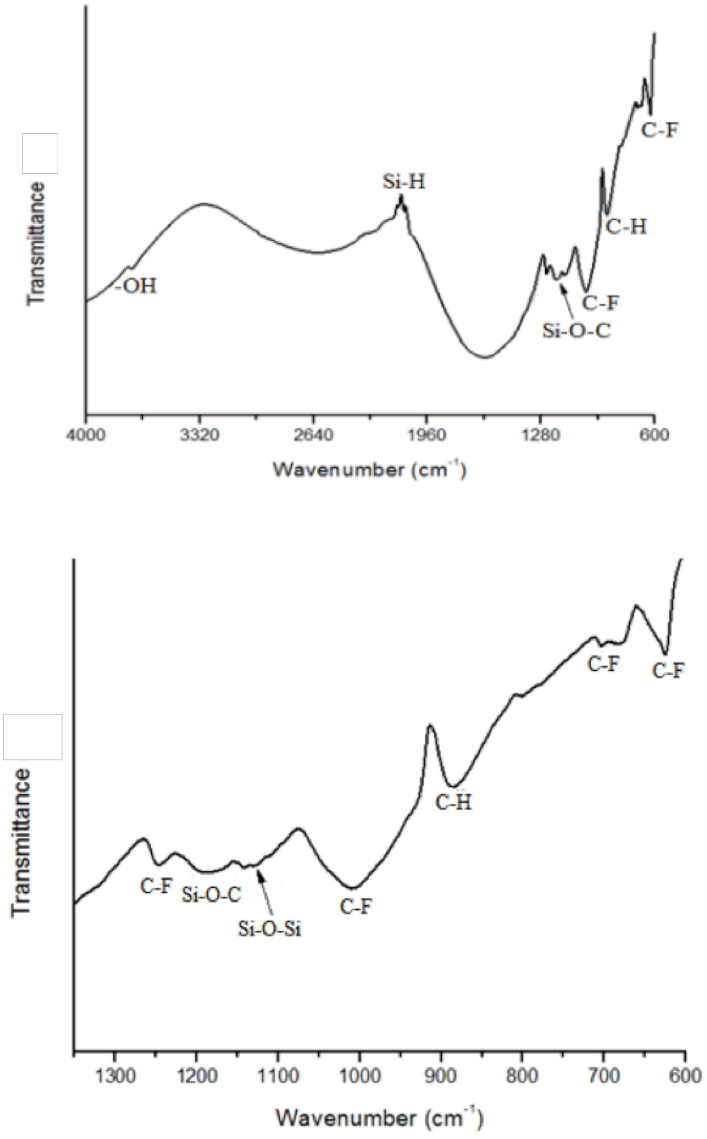

Figure 4.7: DRIFT-IR spectra of porous silicon Si-H terminated micro-porous surface functionalized with heptadecafluoro-1,1,2,2-tetrahydrodecyl trimethoxysilane. Porous Si-H terminated surface was used as reference background. 100 scans were acquired per spectrum at resolution 4 cm^{-1}. For samples analyzed by DRIFT-IR etching of Si (100) p-type wafer was etched in (1:1) HF/Ethanol mixture with current density of 8:3 mA/cm for 5 min

4.3 Pore wetting of porous silicon

The commonly used method for measuring the pore size of nanomaterials, specifically porous silicon materials, is through gas absorption. This involves monitoring gas condensation in the porous structure as a function of the gas pressure and with this one can obtain pore size, surface area and free volume of the porous structure [Groen et al., 2003]. Pore fillings of porous silicon with other compounds have been utilized for applications other than to gain knowledge about its porosity. Porous silicon can be filled for example with metals through an electrochemical process, conducting polymers, and also other materials for gas detection and as biosensors [Ogata et al., 2006]. In this work, we studied the interaction of the porous surface with a salt aqueous solution to better understand wettability, and mechanism of interaction of the porous silicon surfaces with an aqueous medium, upon drying we were also able to visualize how the pores are filled. These experiments were carried out with phosphotungstic acid hydrate (PTA). This is an electron dense compound that is sometimes used as a staining agent for biological tissues imaging using scanning and transmission electron microscopy techniques.

In Figure 4.8 are the secondary electron micrographs of the porous silicon surfaces functionalized with HFTHDTMS after adding 2 x 20 μL of a 2% PTA aqueous solution. What we observed was that there was no pore filling when the PTA was applied on the HFTHDTMS functionalized micro, meso and macro porous silicon surfaces. This suggests that the perflouro alkyl functionalities act as an excellent barrier to pore wetting limiting the deposition of PTA molecules to the surface of the porous film.

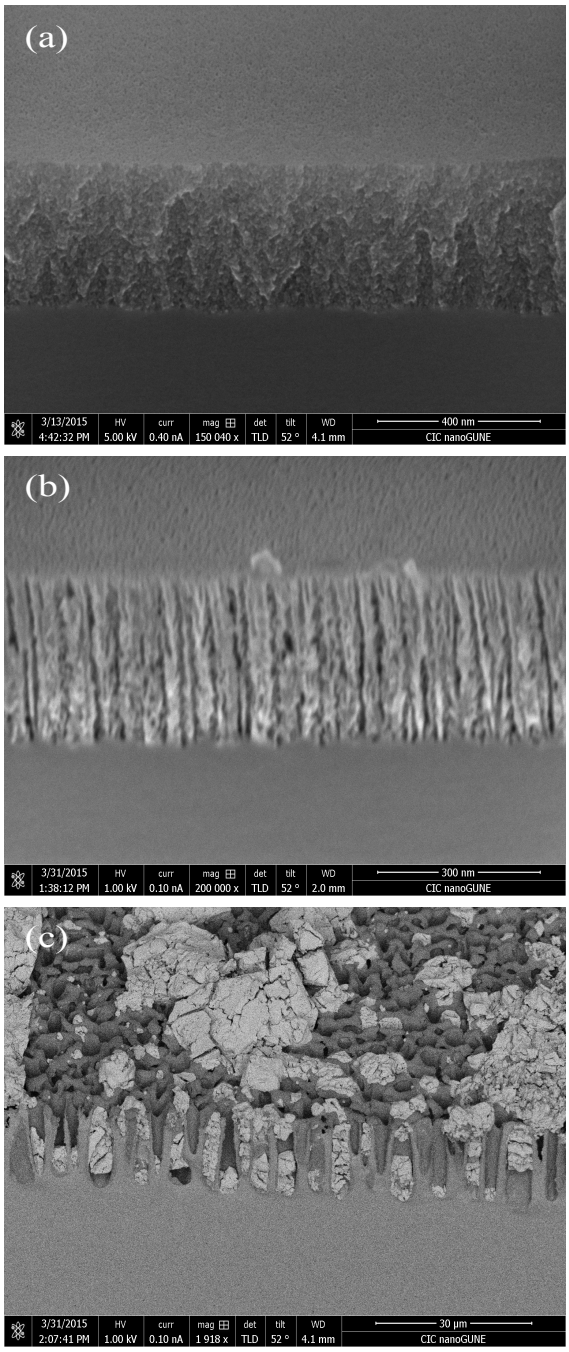

Figure 4.8: Scanning electron micrographs of cross sectional regions of HFTHDTMS functionalized a) microporous b) mesoporous c) macropores silicon after the application of 2 x 20 µL of a 2% PTA solution to the porous silicon surfaces followed by drying in air.

In the case of the macroporous silicon material it appears that the drying PTA collapsed into the larger pores (see Figure 4.8c). These findings are very important because they tell us that for the HFTHDTMS functionalized porous surfaces used in DESI the pores are not expected to play an important role in storing or retaining the analyte but they may still play an important role in how the spray is interacting at the surface and how this may in turn affect the desorption/ionization process. This will be discussed further in the next section.

Oxidized porous silicon surfaces were also analyzed in a similar way using a ca. 2% PTA aqueous solution. However, due to the high hydrophilicity of the material the samples were immersed over night in the PTA solution. But following this procedure the pores were not completely full. Hence, 2 times 20 μL of PTA were applied on top of the samples the following day and they were left to dry overnight. Figure 4.9 shows an SEM image acquired using secondary electron of an oxidized microporous silicon surface exposed to PTA, and its corresponding backscattered electron image. The images shown in Fig. 4.9b) shows clearly the bottom-up filling of the pores when the samples were exposed to PTA a second time. One should also notice how uniform the pore filling occurred. In Figure 4.10 are the secondary electron image of an oxidized mesoporous silicon surface, and its corresponding backscattered electron image. For this pore size, the second application of PTA resulted in the formation of small PTA nanoparticles in the pores. The even distribution of these particles indicates that the pores were fully accessible to the solution upon wetting. Further analysis of this sample will be presented below.

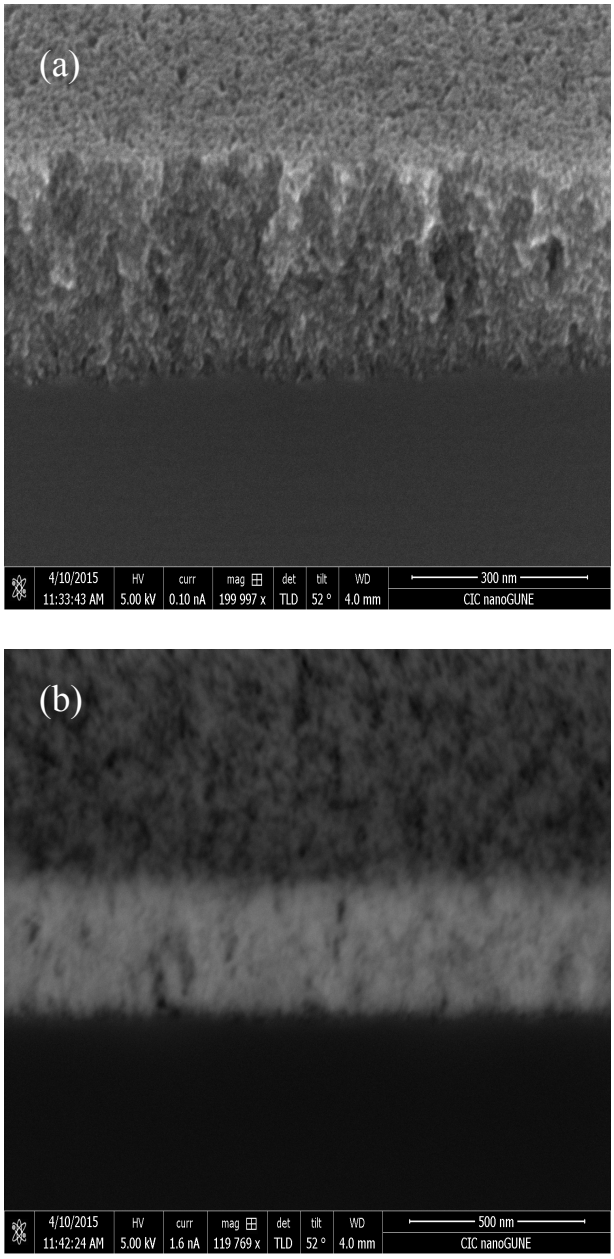

Figure 4.9: Scanning electron micrographs of cross sectional region of oxidized microporous silicon, a) using secondary electron, b) using backscattered electron after immersion of the surface in PTA solution overnight and application of 2 x 20 µL of a 2% PTA solution to the same porous silicon surfaces followed by drying in air overnight.

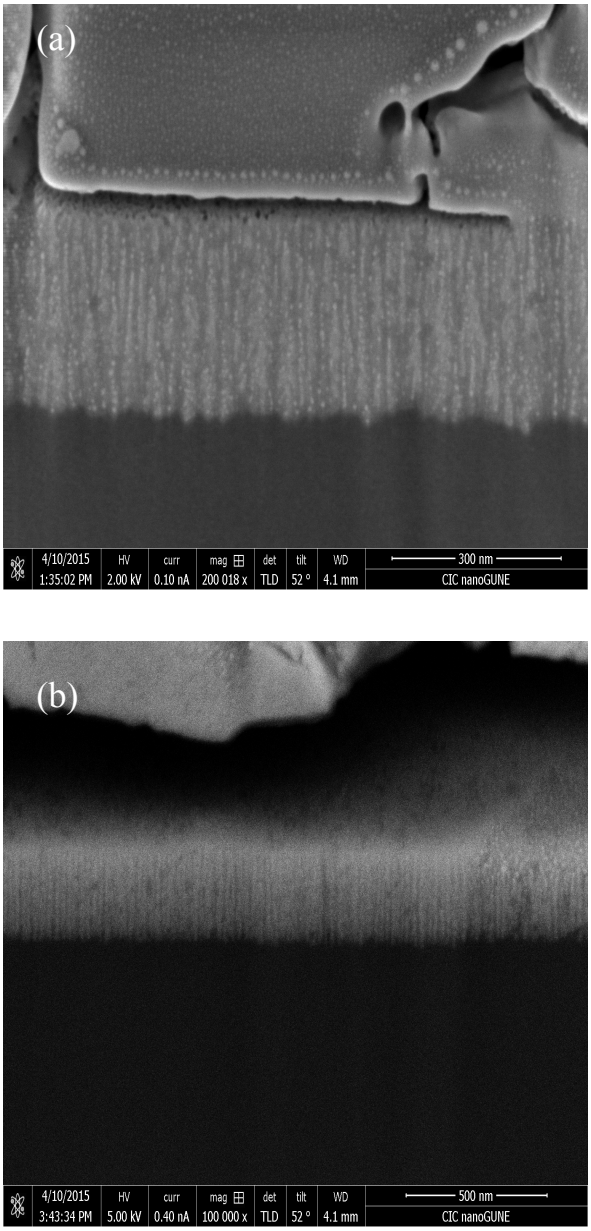

Figure 4.10: Scanning electron micrographs of cross sectional region of oxidized mesoporous silicon, a) using secondary electron, b) using backscattered electron after immersion of the surface in PTA solution overnight and application of 2 x 20 µL of a 2% PTA solution to the same porous silicon surfaces followed by drying in air overnight.

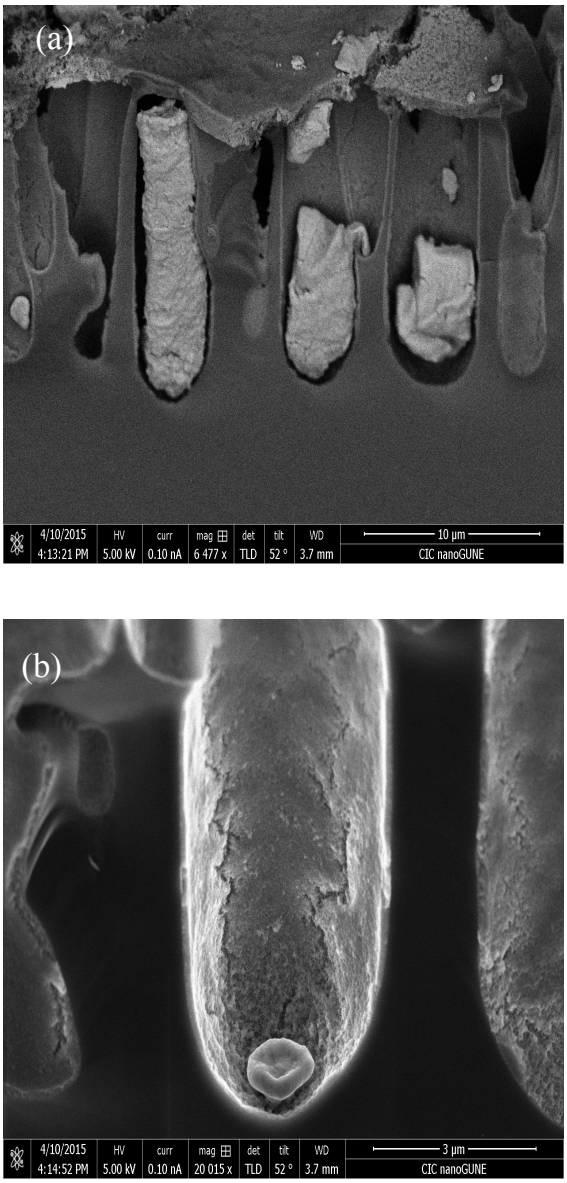

Figure 4.11: Scanning electron micrographs of cross sectional region of oxidized macroporous silicon, a) using secondary electron, b) using backscattered electron after immersion of the surface in PTA solution overnight and application of 2 x 20 µL of a 2% PTA solution to the same porous silicon surfaces followed by drying in air overnight

And in Figure 4.11 are the images corresponding to the oxidized macroporous silicon filled with PTA. Visible in all these image are the pore filling of the porous silicon with the PTA molecules, and this is marked by the brighter color in the backscattered electron micrograph which represent the higher electron dense PTA molecules. For the macroporous sample one can see the thin PTA coating on the surface of the pore resulting from the immersion in PTA (Fig. 4.11b) and the incomplete pore filling resulting from the second application of PTA directly on top of the sample (Fig. 4.11a). However, in the case of the macroporous sample the pore filling resulting from the second PTA application is rather uneven.

Furthermore, deposition of PTA into the pores allows us to obtain the size distribution of the mesoporous and microporous materials prepared in this work. A software package Image J was used for this purpose. The secondary electron image, the image of the isolated PTA particles and the graph illustrating the distribution of the PTA particles in the microporous and mesoporous materials are shown in Figures 4.12 and 4.13, respectively. In the analysis we assumed that the particle size of PTA corresponds to the width of the pores. Hence, a determination of the PTA particle size distribution would yield the pore size diameter distribution of the pores. Careful analysis of the SEM images such as the one reported in Figs. 4.12a) and 4.13a) supports this assumption. Using the secondary electron images and the Image J software package, isolated PTA particles could be carefully identified and the graph illustrating the pore size distribution (i.e., PTA particle size distribution) generated Figs. 4.12d) and 4.13d).

The distributions shows that the average pore sizes are 7 ± 4 nm and that 72 % of the pores have diameters between 2 and 10 nm and 9 ± 4 nm and that 81 % of the pores

have diameters between 5 and 20 nm in the microporous and mesoporous materials, respectively. The distribution supports the conclusion that we are indeed preparing micro- and meso- porous materials. As noted before, there was not enough PTA in the applied solution to fully fill the macroporous materials. However, pore size distribution is less relevant in the case of this material due to the ease with which they can be visualized.

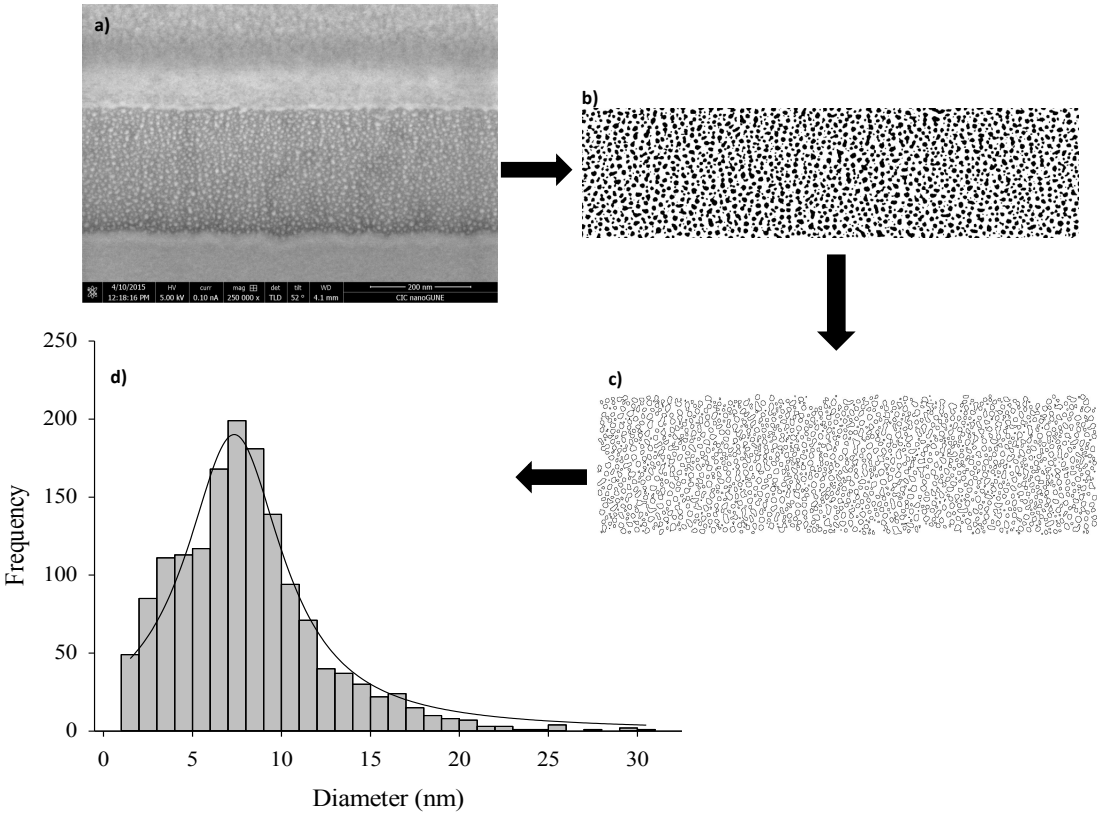

Figure 4.12: Scanning electron microscope images of oxidized microporous silicon with pores filled with PTA, a) using secondary electrons, b &c) illustration of isolated PTA particle, d) graph showing particle size distribution.

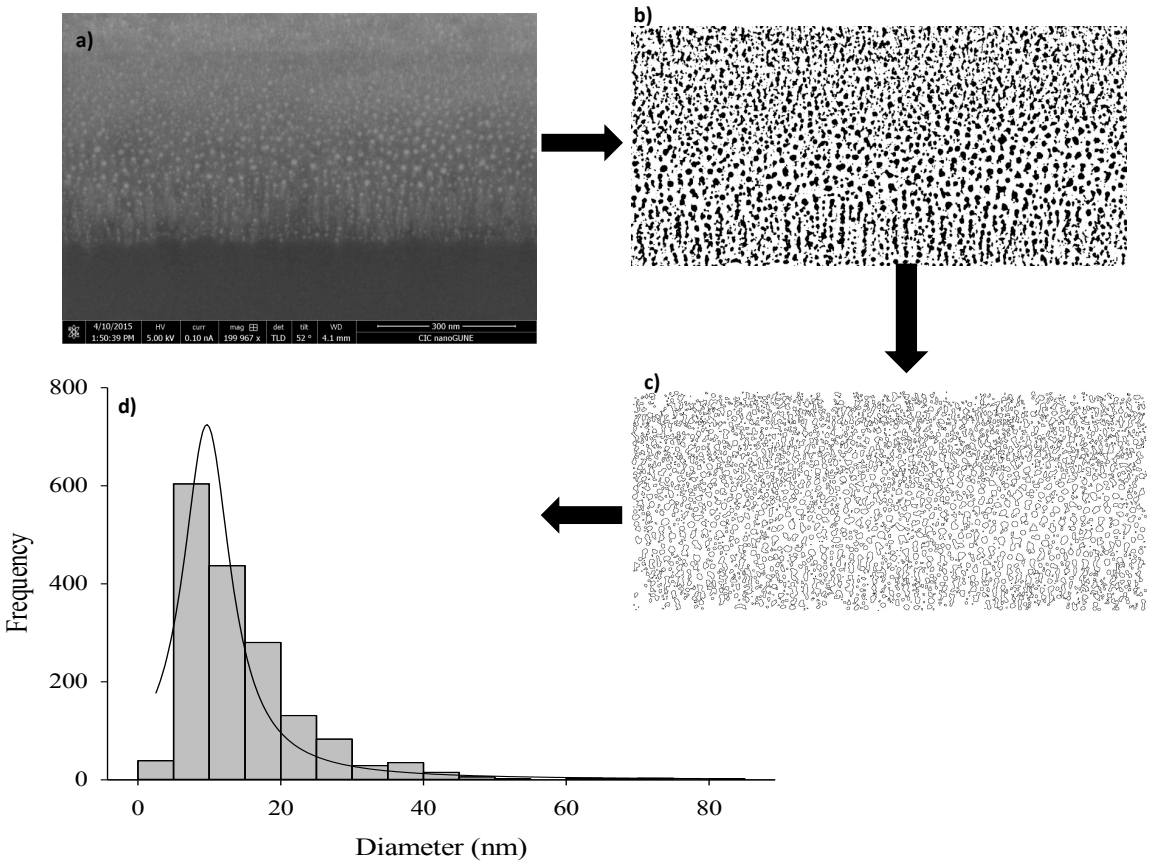

Figure 4.13: Scanning electron microscope images of oxidized mesoporous silicon with pores filled with PTA, a) using secondary electrons, b &c) illustration of isolated PTA particle, d) graph showing particle size distribution.

Chapter Five

DESI-MS Analysis of Small Molecules on Porous Silicon

Results and Discussion

5.1 Signal stability of porous silicon

To evaluate the efficiency of porous silicon surfaces as suitable substrates for DESI-MS analysis, porous silicon surfaces with different pore size diameters were fabricated. The three porous surfaces terminated with alkyl groups from functionalization with 1-decene were compared using criteria that are important for DESI-MS analysis. Figure 5.1 illustrates the signal stability comparison of the different surface, performed from a dried spots of 5 μL of Cocaine and of Chloramphenicol solutions both at a concentration of 1 μg/mL. The test involves measuring the same line ten times, in triplicate using the moving stage at 800 μm/s. The highest intensities per replicate of the base peak from each compound were used to evaluate the signal stability. The desorption/ionization signal intensities were evaluated in the positive ion mode for cocaine and in the negative ion mode for chloramphenicol.

From the graph it is obvious that all the porous silicon surfaces display the best signal stability for both compounds than the flat (nonporous) silicon surface. The amount of sample desorbed from the flat (nonporous) silicon surface decreases exponentially, whereas the porous silicon surfaces had minimal change after ten repetitions. It was observed that all the porous silicon surfaces including the oxidized microporous silicon (Fig. 5.2) display very good signal stability in the positive ion mode.

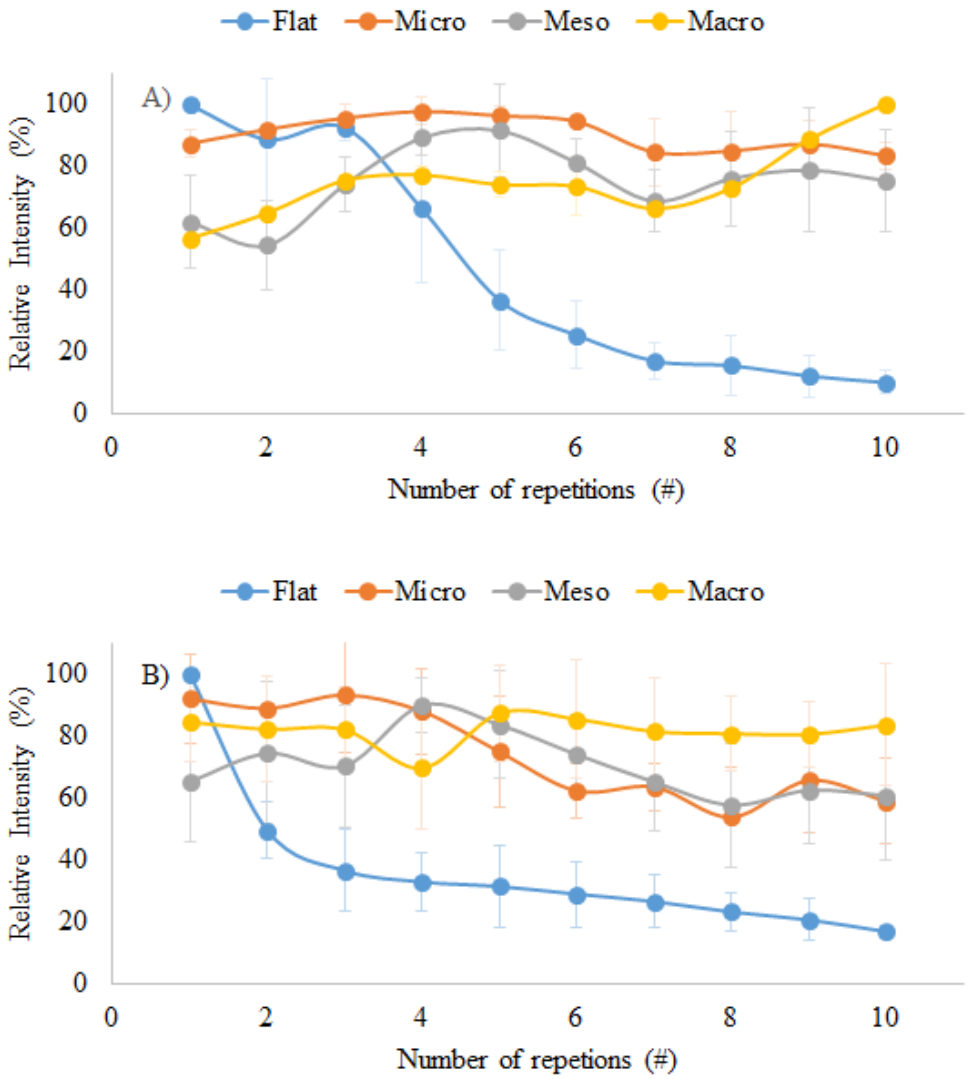

Figure 5.1: Signal stability analysis of an aliquot of 5 µl of a 1 µg/mL (A) cocaine and (B) chloramphenicol solution ran 10 times per line in triplicate. Each point represents triplicate analysis of the highest intensities per repetition of the compounds ion peaks. The vertical bars represent standard errors.

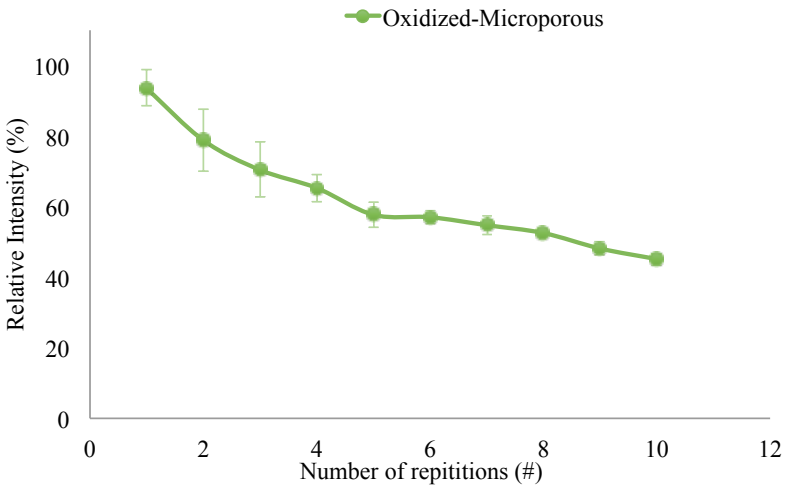

Figure 5.2: Signal stability analysis of an aliquot of 5µl of a 1µg/mL acetylcholine solution ran10 times per line in triplicate. Each point represents triplicate analysis of the highest intensities per repetition of the compounds ion peaks. The vertical bars represent standard errors.

We hypothesized that the electrospray solvent, in this case methanol, directed towards the sample surface creates pools. The solvent pool is then pushed against the pores of the porous silicon surfaces by succeeding spray droplets without entering the pores due to the hydrophobicity of the surface, including that of the pore walls. This process would create turbulence in the pool improving the solubility of the analyte previously crystalized on the surface. This mechanism is shown to improve the desorption/ionization efficacy without fast removal of the sample, therefore maintaining high signal strength and stability for longer period of time. However, for the flat nonporous silicon surfaces, the opposite occurred whereby an unstable signal could be

due to quick removal of the sample from the surface. Furthermore, for the oxidized porous silicon surface it was difficult to obtain good signal, the DESI flow rate parameter of the spray solvent had to be highly increased (15 μm/min versus 3 μm/min) before a signal was obtained in positive ion mode. However, with the increase flow rate, we still were not able to achieve good ion signal in the negative ion mode because the analyte was not desorbing efficiently when the same parameters were employed. This could be caused by the analyte's ability to penetrate into the pores of the oxidized porous silicon materials causing a drastic decrease of the signal intensity.

5.2 Cross-contamination test of porous silicon

In the DESI-MS experiment, factor such as cross contamination is of importance and prominent when the thin layer of solvent containing dissolved analytes is pushed or splashed along the surface. This was evaluated for our porous surfaces using 4 different small molecule analytes. The test was performed by pipetting 1 μL of the different analytes all at 1 μg/mL concentrations in a line with around 1 mm distance between each droplet. The sample was left to dry at room temperature and was scanned by DESI at a scan rate of 350 μm/s. In Figure 5.3 is the extracted-ion chromatogram obtained to evaluate the degree of cross contamination. The carry-over or tailing effect for the 4 different compounds is clearly prominent for the oxidized microporous and flat (nonporous) silicon substrates compared to the other porous silicon surfaces (see Fig 5.3). This is visible by the overlap between the peaks for the flat (nonporous) surface and the oxidized microporous surface, whereas the effect was minimal for the other porous silicon surfaces. The carryover of analyte between the dried analyte spots on the flat nonporous surface is due to solvent splashing as observed in figure 5.4.

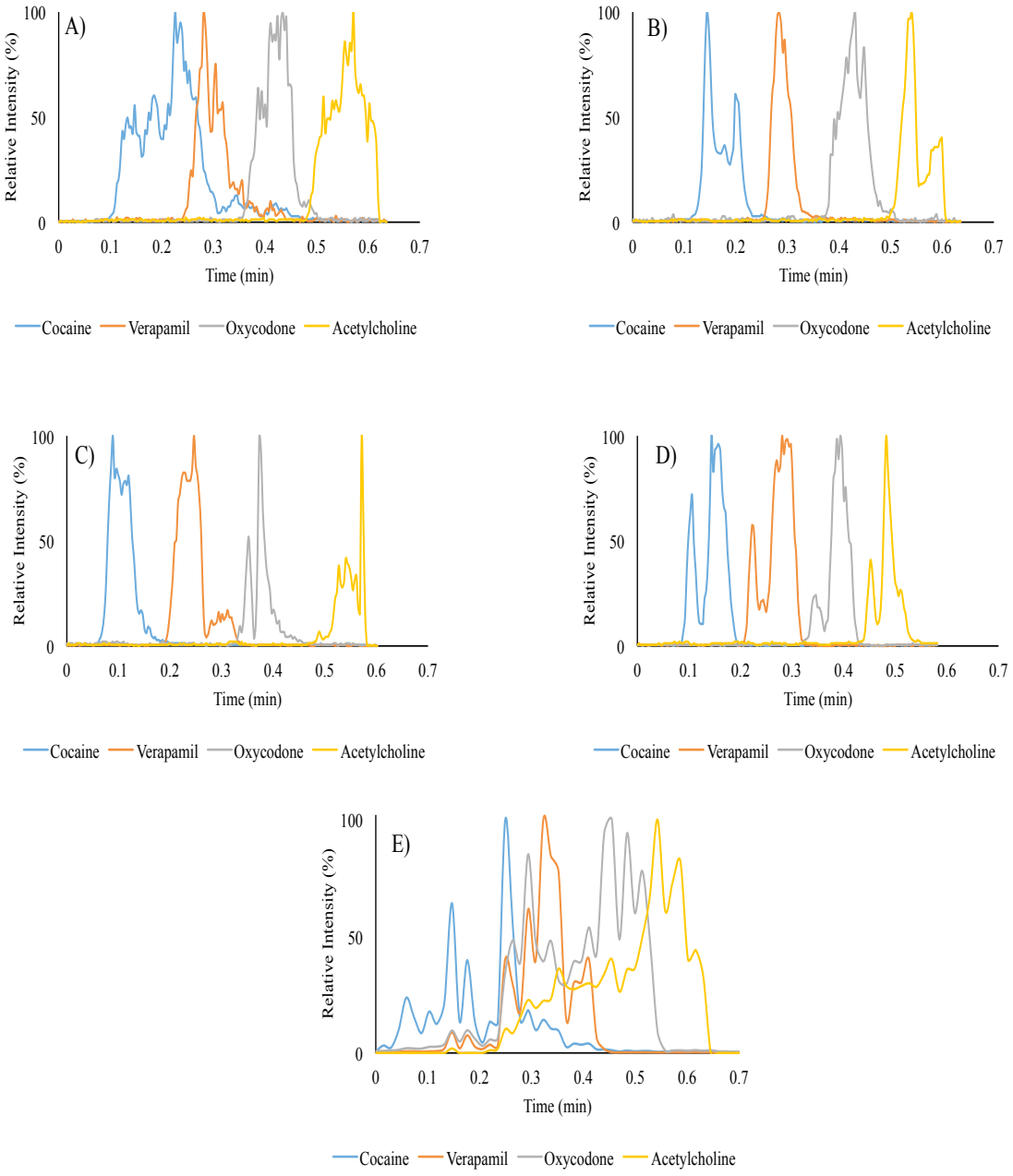

Figure 5.3. Extracted-ion chromatogram intensities of Cocaine, Verapamil, Oxycodone and Acetylcholine solution at 1 µg/mL. Aliquots (1 µL of each solution) were deposited in a straight line about 1 mm apart on A) nonporous, B) 1-decene-microporous C) 1-decene-mesoporous D) 1-decene-macroporous and E) oxidized-microporous silicon surfaces.

The functionality of the surface has a huge effect on carryover, as observed for the oxidized-microporous silicon surface. Unlike the hydrophobic surface, where the droplets could be separated (see Figure 5.4), on the oxidized surface, the droplets were widely distributed and mixed with each other upon deposition on the surface. As well, the carryover is also caused by mixing of the dried samples due to the spray solvent spreading over a larger area upon interaction with the hydrophilic surface. The hydrophobicity of the other porous surface kept the dried spot to a small sampling area, limiting any cross contamination effect. Also The roughness/porosity of the porous silicon surfaces and the hydrophobicity act as barrier hindering the spreading of both the spray solvent and the analyte therefore decreasing carryover, this was reported for porous PTFE as well [Ifa et al. 2008].

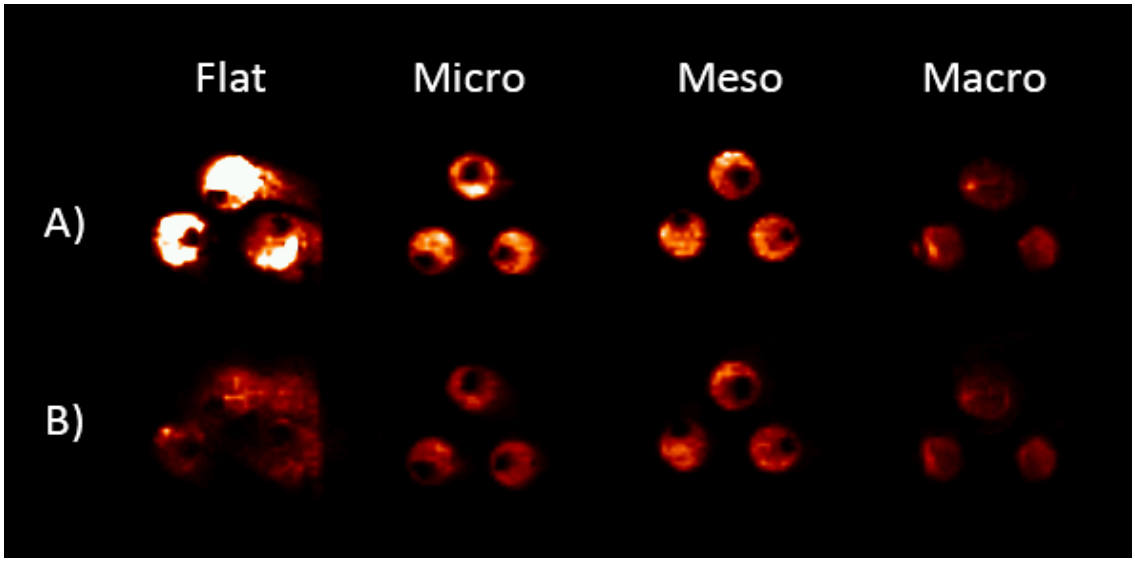

Figure 5.4: Dried spot DESI imaging of 1µg/ml of propranolol ($[M+H]^+$, *m/z* 260) on flat (nonporous), 1-decene functionalized micro-, meso-, and macro-porous silicon; and B) imaging of the same samples after images shown in A) were recorded.

5.3 Ion efficiency analysis of porous silicon

Investigation of effect of the different pore sizes on the ionization efficiency in DESI was carried out using a mixture of four different small molecule compounds (cocaine, acetylcholine, verapamil, and oxycodone) with final concentration of 200ng/mL for each compound. Aliquots of 1μL of the final solution were deposited on each surface and left to dry at room temperature. The highest signal intensity was chosen to compare the desorption/ionization efficiencies. The signal intensity tabulated in Table 5.1, shows that the porous silicon did provide better signal intensities under same condition compare to the flat (nonporous) silicon. The microporous silicon provided the highest signal intensity of 9.42×10^3. These show that there is significant improvement in sample ionization on porous silicon surfaces. Functionalization of the porous silicon with 1-decene helps to increase the analytical signal of the molecules due to hydrophobicity. At the same time the porosity of the surface appears to delay the quick removal of samples leading to better signal stability. Figure 5.5 is the mass spectra of the three surfaces functionalized with 1-decene, we obtain for the four small molecule compound

Table 5.1: The highest total ion current observed for analysis of small molecule mixture of (cocaine, acetylcholine, verapamil, and oxycodone) on the different porous silicon surfaces functionalized with 1-decene

Surfaces	Pore diameter	Signal intensity
Microporous	(2 - 10nm)	9.42×10^3
Mesoporous	(10 - 50nm)	4.40×10^3
Macroporous	(2 - 4μm)	5.11×10^3

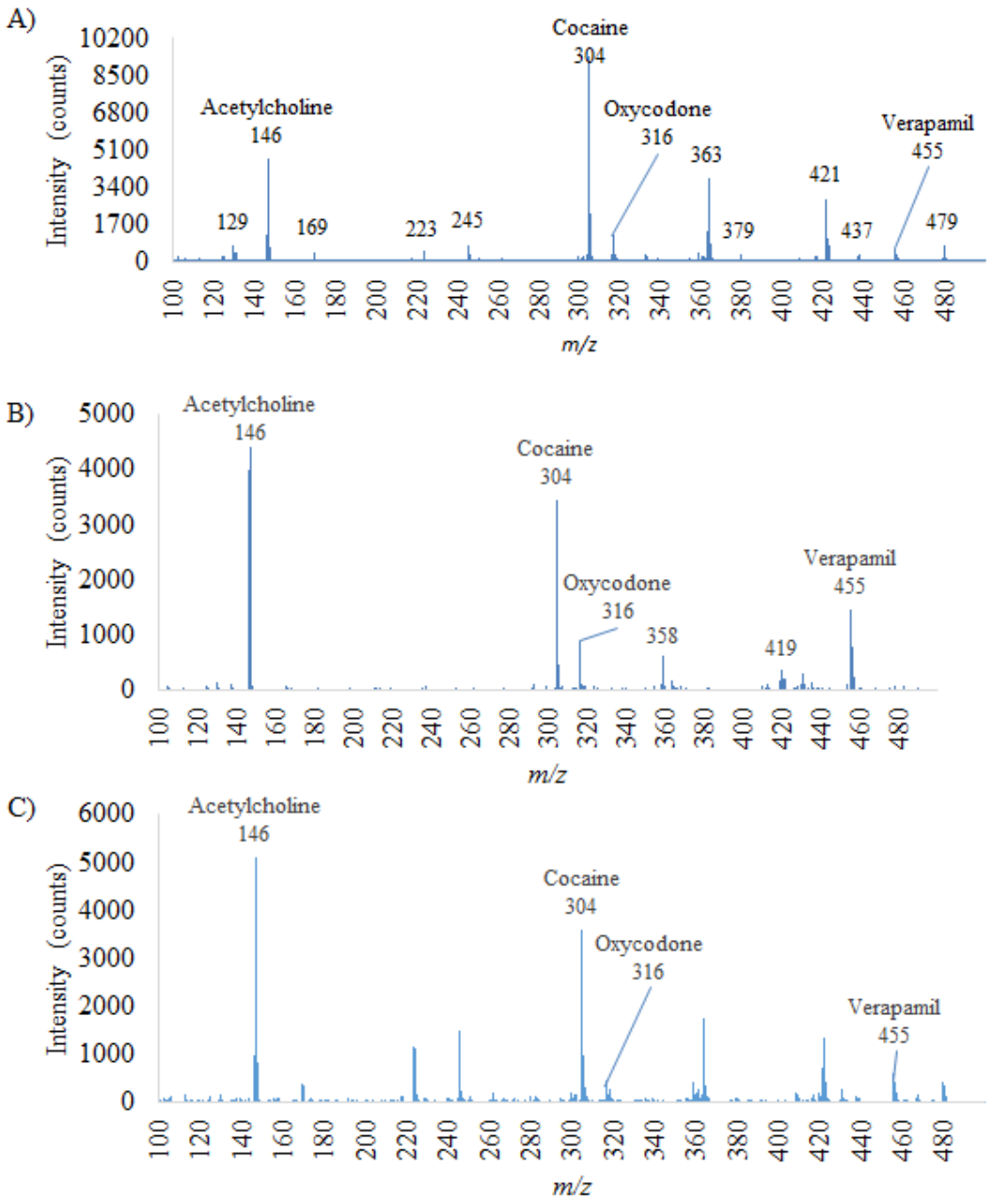

Figure 5.5: DESI-MS spectra in positive mode for a mixed solution containing Acetylcholine, Cocaine, Oxycodone and Verapamil at a final concentration of 200ng/mL for each component of the mixture acquired on 1-decene functionalized A) microporous B) mesoporous and C) macroporous-silicon surfaces.

We evaluated effects of modifying the porous silicon, mainly the microporous with oxidation and HFTHDTMS using a sillanization process. The etching conditions for the microporous film was chosen based on previous experiments and the results showed that the microporous sample produced higher signal intensities (see Table 5.1) and signal stability (see Fig 5.1). Thermal and aqueous oxidation of freshly etched microporous silicon surface was performed to provide oxidized microporous silicon. The same oxidation process was used to produce hydroxyl groups for the silylation process following deposition of the silylating reagent and heating for 30 min. The HFTHDTMS consist of flouro-alkyl groups that express a higher hydrophobic behaviour than 1-decene.

To evaluate the ionization efficiency of the oxidized and HFTHDTMS-microporous silicon surface, a sample of four different compounds (cocaine, propranolol, verapamil, and acetylcholine) with final concentration of 200 ng/mL for each compound were analyzed. Aliquots of 1 μL of the mixed sample were deposited on each surfaces, and left to dry at room temperature. The spot was scanned with DESI at rate of 350 μm/s. The extracted mass spectra are displayed in Figure 5.6, which shows a comparison of oxidized microporous silicon, HFTHDTMS microporous silicon, and flat (nonporous) silicon. The HFTHDTMS-microporous silicon surface gave the highest ion intensity (3.39×10^4) of all the surfaces employed and also when compared to ionization efficiencies of common surfaces used for DESI analysis, i.e., polymethylmethacrylate (PMMA), and porous polytetrafluoroethylene (PTFE) (see Table 5.2 for signal intensity data and (Fig. 5.7 for the corresponding mass spectra). In addition, the oxidized microporous silicon (Fig 5.6) produces the lowest ion intensity (7.21×10^1).

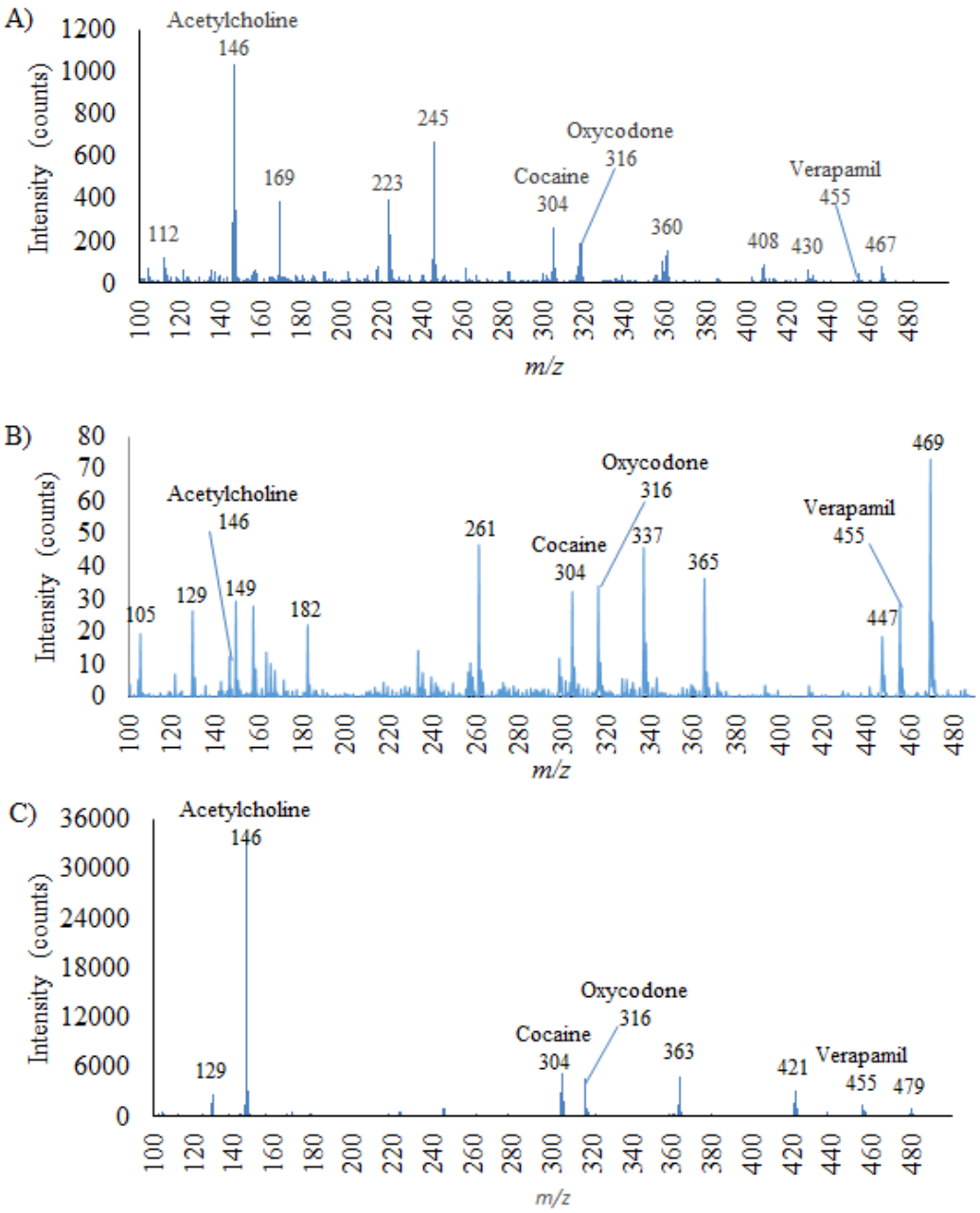

Figure 5.6: DESI-MS spectra in positive mode for a mix solution contain Acetylcholine, Cocaine, Oxycodone and Verapamil at final concentration of 200ng/mL for each component of the mixture acquired on A) flat (non porous) B) Oxidized-microporous and C) HFTHDTMS-microporous silicon surfaces.

This further provides evidence that desorption/ionization is improved by an increase in the hydrophobicity of the surface, since the most hydrophobic surface provided us with the highest signal intensities. The hydrophobicity of the HFTHDTMS-microporous silicon appears to be reducing spreading of both the solvent and dissolved analytes resulting in the analytes being more concentrated on the surface. Furthermore, the hydrophobic surface prevent pore filling with the sample whereas the sample can penetrate into the pores of the oxidized porous silicon surfaces (Fig 4.8) in our wetting experiment using PTA. This explanation is consistent with the improved ion intensity observed with the hydrophobic surfaces, and the poor performance of the oxidize porous surface.

Table 5.2: The highest total ion current observed for analysis of small molecule mixture (cocaine, propranolol, verapamil, and acetylcholine) on different surfaces

Surfaces	Signal intensity
Flat nonporous silicon	1.03×10^{3}
1-Decene Microporous	9.42×10^{3}
HFTHDTMS-microporous	$\mathbf{3.39} \times 10^{4}$
Oxidized microporous	7.21×10^{1}
polymethylmethacrylate (PMMA)	3.12×10^{3}
Porous polytetrafluoroethylene (PTFE)	5.67×10^{2}
Porous PTFE: (water: methanol solvent)	6.10×10^{3}

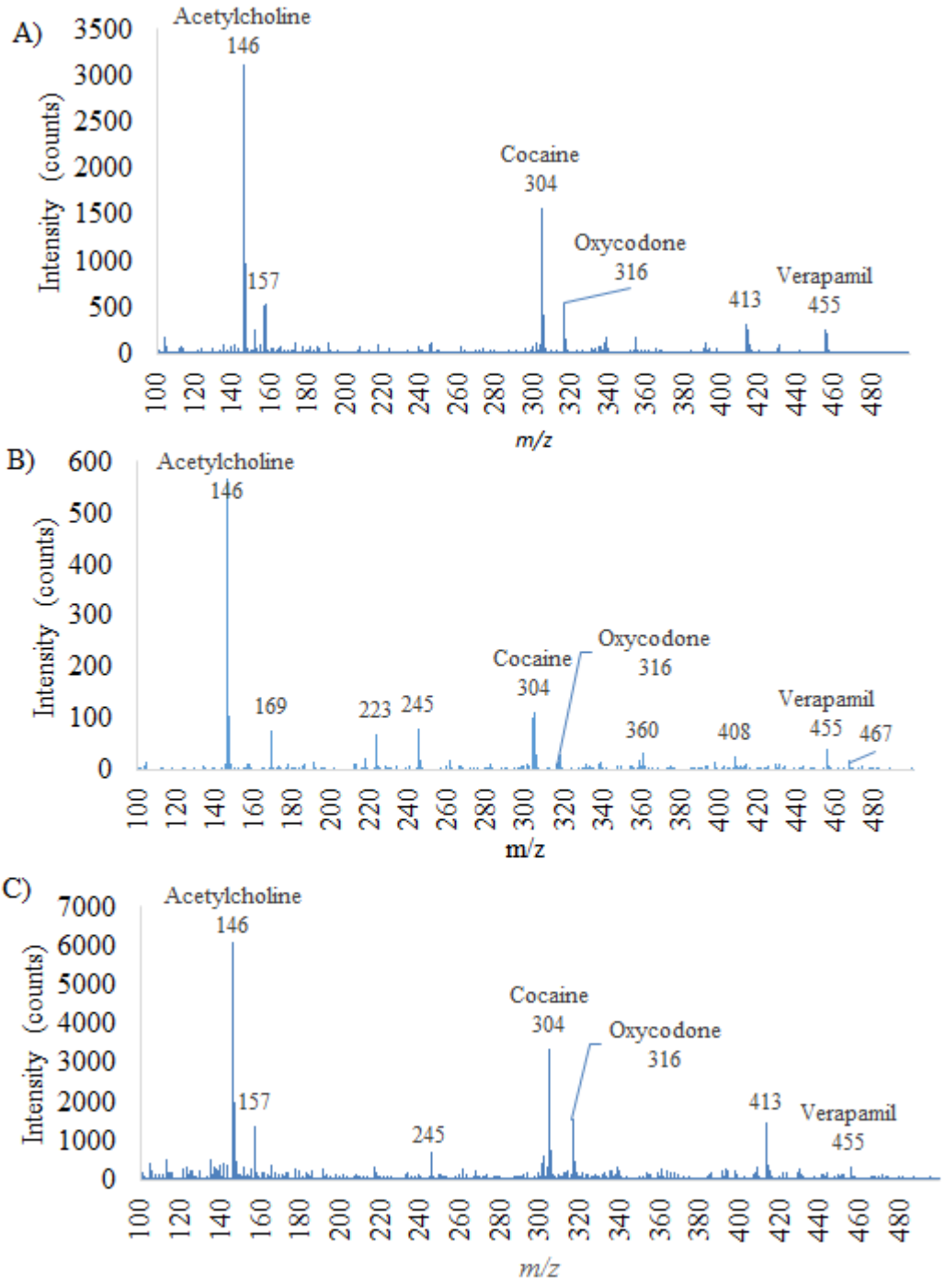

Figure 5.7: DESI-MS spectra in positive mode for a mix solution contain Acetylcholine, Cocaine, Oxycodone and Verapamil at final concentration of 200 ng/mL for each compound acquired on A) PMMA, B) Porous PTFE and C) Porous PTFE (water: methanol) surfaces

5.4 Limit of detection of small molecule analyte on porous silicon

In Table 5.3 is the comparison of the lowest concentration detected (LOD) for the different analytes. In this experiment, eleven different common pharmaceutical and biologically important analytes were studied in five different concentrations, ranging from 0.5 ng/mL to 1 μg/mL. The analytes were deposited in a straight line and scanned by DESI across the dried spots. MS/MS was used as the detection method and the ion current used for data analysis. The flat (nonporous) silicon surface showed the highest LOD values for all compounds, while the porous surface provides similar LOD for most of the compounds (see Table 5.3). The HFTHDTMS-microporous silicon provided better LOD for four of the compound tested (Acetylcholine, Diazepam, Roxithomycin, Chloramphenicol)

Our results showed that the porous silicon surfaces are appropriate for analysis of small amount of molecules. This can be very useful in the study and detection of small amount of analyte in real samples. The HFTHDTMS-microporous silicon surface displays the highest total ion count (TIC), and the best LOD. This is related to the highly hydrophobic characteristic of the flouro-akyl group, with the ability to concentrate the sample in a small area. The presence of pores enhances desorption of the secondary ions, by preventing splashing of the spray solvent. The prepared 1-decene functionalized porous surfaces and HFTHDTMS-microporous silicon surface exhibited much lower LOD than that of porous PTFE substrate published in the literature for the same compounds and concentrations [Ifa et al., 2008]. The lowest LOD for the porous PTFE were of the order of 10 ng/mL, whereas the lowest LOD for our porous silicon substrate was 0.5 ng/mL. Out of all our investigated surfaces, it can be concluded that the

HFTHDTMS-microporous silicon is the best for analysis small molecule analyte. However DESI-MS analysis is also highly dependent on the spray solvent, which must be tailored to the analyte of investigation.

Table 5.3. Lowest concentrations detected for representative compounds on different surfaces

Compound	**Polarity**	**Collision Energy**	**Precursor → Product (*m/z*)**	**LOD (ng/mL)**		
				Flat Silicon Wafer	1-decene-microporous silicon	HFTHDMS-microporous silicon
Acetylcholine	+	30	146 $[M+H]^+$ → 87	100	1	**0.5**
Propranolol	+	27	260 $[M+H]^+$ → 183	1	0.5	0.5
Testosterone	+	20	289 $[M+H]^+$ → 253	1000	10	10
Diazepam	+	22	285 $[M+H]^+$ → 257	100	10	**1**
Cocaine	+	14	304 $[M+H]^+$ → 182	10	0.5	0.5
Oxycodone	+	30	316 $[M+H]^+$ → 298	1	0.5	0.5
Verapamil	+	23	455 $[M+H]^+$ → 182	100	1	1
Roxithomycin	+	20	837 $[M+H]^+$ → 679	10	1	**0.5**
Angiotensin	+	20	524 $[M+H]^{2+}$ → 784	100	10	10
Ibuprofen	-	20	205 $[M-H]^-$ → 161	1000	100	100
Chloramphenicol	-	27	321 $[M-H]^-$ → 257	10	10	**1**

Chapter Six

DESI-MS Imaging Results and Discussion

6.1 DESI-MS imaging of rat brain tissue

We investigated the DESI-MS imaging of biological molecules using our functionalized porous silicon surface. We made use of rat brain tissue as a model sample for identification of the presence of lipids in the tissue. Lipids are easily ionized and measured by DESI-MS. Lipids are diverse group of molecules with different structures and plays important roles in cellular process. DESI-MS has been used for direct analysis of different lipid classes including fatty acids (FA), glycerol phospholipids (GP), sphigolipids (SP) and sterol lipids (ST) [Eberlin et al., 2011]. DESI has also been used for imaging of a variety of tissues. DESI-MS imaging of canine bladder tissue was used for characterization of lipids for distinguishing tumor cells from normal tissue cells [Dill et al., 2009]. Traditional surfaces of choice for DESI-MS imaging include polytetrafluoroethylene printed glass (PTFE) and glass slides. Biological tissue imaging has been performed using porous silicon as substrate with different mass spectrometry techniques. Yanes et al. performed matrix-free tissue mass spectrometry imaging on functionalized porous silicon using the nanostructured initiator mass spectrometry (NIMS) method [Yanes et al., 2009]. Tissue attachment was performed by cryosectioning of ultrathin tissue slices (<5 μm) mounted on the functionalized porous silicon surface. Cutting of an ultra thin tissue slice is a challenging and time consuming task, therefore Ronci et al. made use of another method called contact printing of tissue, which require a tissue slice of normal thickness to be mounted on the surface, which allows to interact

before its removal. The surface that was in contact with the tissue is then scanned by NIMS imaging [Ronci et al., 2012]. DESI-MS imaging allows analysis of the tissues with much shorter preparation steps and without any additional treatment of the sample.

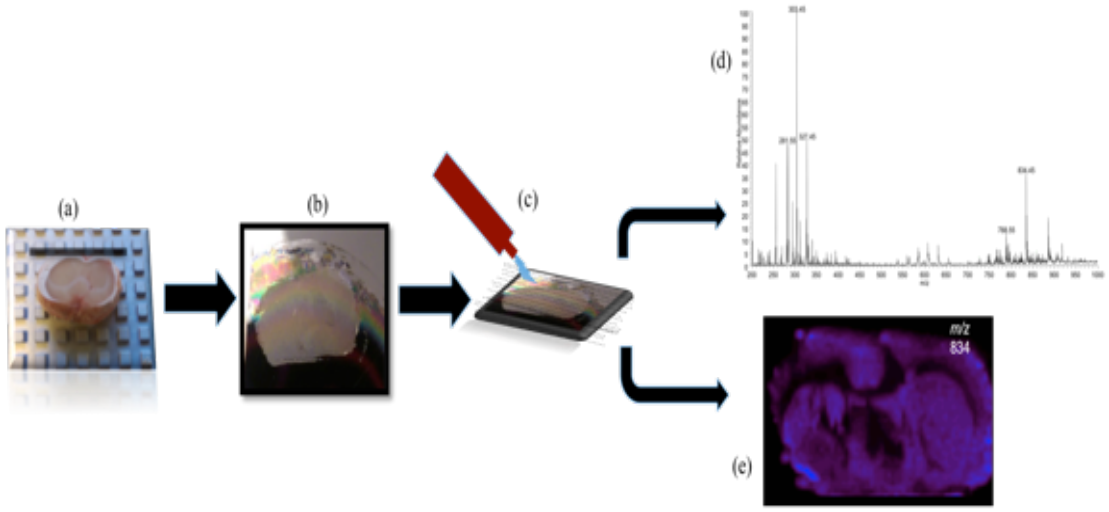

Figure 6.1: Schematic representation of DESI-MS imaging of rat brain tissue. (a) Rat brain tissue sample are cryosectioned, (b) thawed tissue sections are mounted on the substrate, (c) then directly analyzed by DESI-MS imaging. (d) Obtained mass spectra of tissue characterization based on lipid profile and (e) DESI ion spectra of specific lipid

In this thesis we embark on developing a methodology for DESI-MS imaging biological samples that would allow sample preservation, reduce contamination and allow for successive analysis to be performed on the same samples. Our preliminary results were obtained by preforming direct analysis of the cryosectioned tissue on porous silicon surface with different surface chemistry following the protocol in Figure 6.1. We made use of oxidized microporous silicon as a hydrophilic substrate, HFTHDTMS

functionalized microporous silicon as a hydrophobic substrate and compared their performance with that of the traditional glass slide substrates.

In Figure 6.2 are the average DESI negative ion mass spectra obtained from each substrate demonstrating the distribution of the lipids. The negative ions detected from the tissues were deprotonated molecules of the form [M-H$^-$]. In Figure 6.2, the low mass charge region (m/z <400) corresponds to deprotonated free fatty acids; the high mass region (m/z >600) ions correspond to various deprotonated lipids. Lipids detected directly from the tissue have been confirmed by tandem mass spectrometry (MS/MS) [Wiseman et al., 2006]. In our investigation, the ions of importance are, oleic acid (18:1), at *m/z* 281.5, arachidonic acid (20:4) at *m/z* 303.4, decosohexaenoate (22:6) *m/z* 327, phosphotidyl serine (36:1), at *m/z* 788.6, phosphotidyl serine (40:6) at *m/z* 834.4 and sulfatide (24:1) at *m/z* 888.5 [Wiseman et al., 2006]. The obtained mass spectra for the three surfaces provide similar ions as shown in Figure 6.2. The only difference is the ion intensity. The total ion cout for the oxidized and HFTHDTMS functionalized porous silicon are 40.5 and 38.3 respectively after optimization of the parameters for the surfaces. It is obvious that both the porous silicon surfaces produce similar ion intensity, which is slightly lower when compared to that of the traditional glass slide with intensity of 80.3 (see Fig. 6.2) .We were able to obtain the images of the lipids within the tissue cell because, this analyte do not penetrate into the pores of the oxidized porous silicon, and therefore they could be easily desorbed and ionized. However the ion intensity were still on the lower side compare to that for the small molecule analysis, and this can be rationalized that the analyte were still strongly attached within the tissue thereby fewer molecules were transferred from the surface resulting in a diminished overall signal.

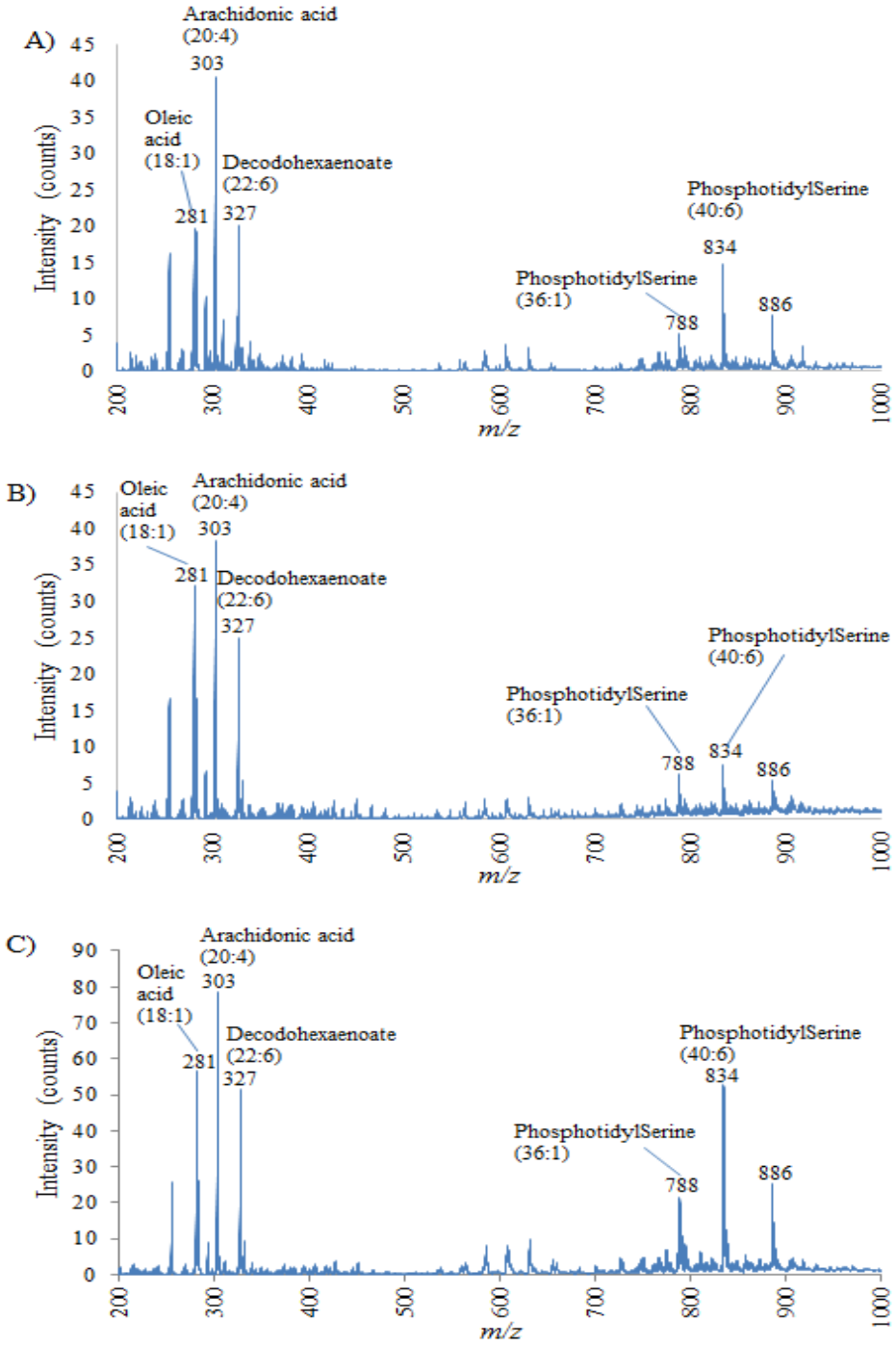

Figure 6.2: The average DESI mass spectra of rat brain tissue slice obtained on A) oxidized micro-porous silicon, B) HFTHDTMS-micro-porous silicon, C) glass slide showing the distribution of fatty acids and phospholipids

The corresponding DESI chemical ion image of the lipids obtained on the oxidized microporous silicon and HFTHDTMS microporous silicon is shown in Figure 6.3. The chemical images were obtained by mapping of the spatial distribution of lipids with peaks at *m/z 281*, *m/z* 303, *m/z* 327 and *m/z* 834 with high ion intensities enough to obtain a chemical image. Images from both surfaces, i.e., oxidized and HFTHDTMS functionalized are of the same quality with similar ion signal intensity. The resolution was set to 200 μm for these images. In Figure 6.4 A) and B) the first frame of each series is the optical image of the rat brain tissue slices. The subsequent images were obtained DESI-MS chemical ion images of same lipids as mentioned above, obtained on A) an oxidized- microporous silicon, compared with B) the traditional glass slide surface used for DESI imaging.

The images quality is also very similar for these two substrates i.e., oxidized porous silicon and glass slide, apart from the ion signal intensity, which is visible from the color scale. This is evident in the mass spectra obtained for the rat brain tissue where the absolute ion intensity for the traditional glass slide is slightly higher than that of the functionalized porous surface (see Fig 6.2). For instance, the ion intensity of the peak m/z 303 is higher in the spectrum for the glass slide than the porous silicon (see fig 6.2) that is corresponding to the greater ion distribution observed in the chemical ion images. It can be concluded that porous silicon surface can be use as substrate for DESI-MS imaging

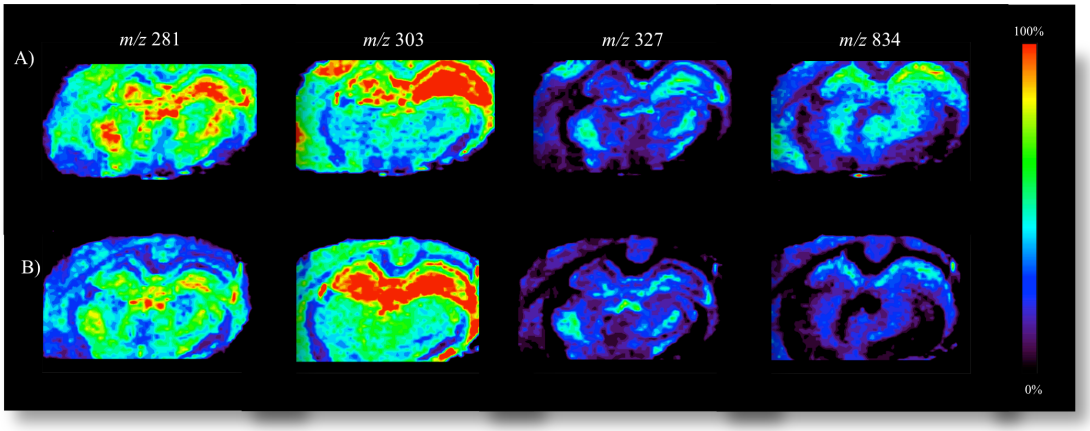

Figure 6.3: DESI ion images of selected lipid ion obtained from 20microns tissue section of rat brain; A) HFTHDTMS-porous silicon B) oxidized porous silicon surface.

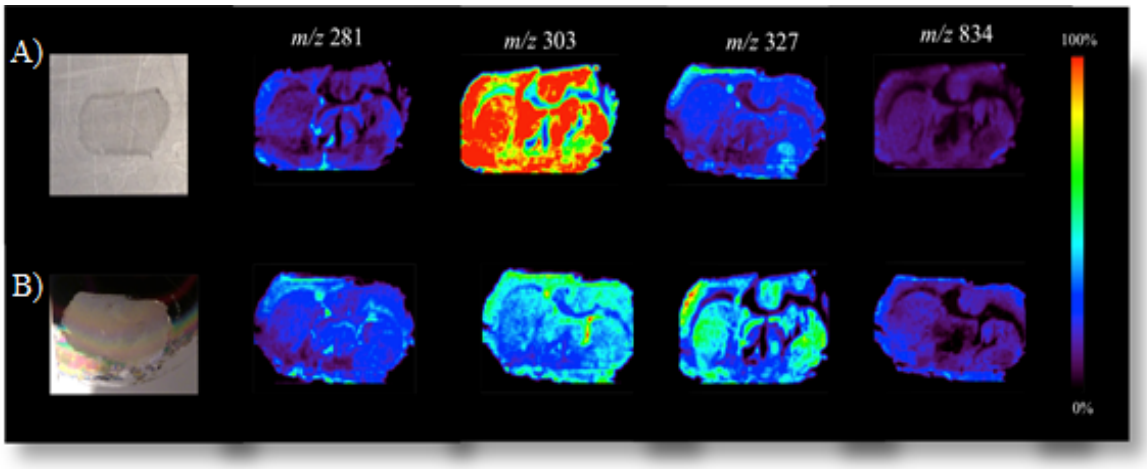

Figure 6.4: Optical images and DESI ion images of selected lipid ion obtained from 20microns tissue section of rat brain on A) glass slide B) oxidized porous silicon surface

Our aim was to make use of contact printing method, whereby the rat brain tissue is sliced onto the functionalized porous silicon, allowing time for interaction before removal of the tissue slice from the surface. The adsorbed analyte on the surface can then be analyzed by DESI-MS imaging. This process will provide analysis of the biological molecules, while keep the geometric parameter constant leading to improved spectral quality and reproducibility. What is required is a protocol for the removal of the tissue slice from the porous silicon surface, while avoiding contamination and elimination of the deposited analytes. This work is on going.

Chapter Seven

Conclusion

The porous surface exhibit great signal stability, no matter what the functional groups are, i.e., either fluoro-akyl or hydroxyl, which produce hydrophobic or hydrophilic surfaces, respectively. This could be due to the pore wells acting as a barrier from the spray solvent splashing. On the other hand, the functional group is crucial for the desorption/ionization, whereby the most polar surface HFTHDTMS–microporous silicon produce the highest ion intensity compare to all other surfaces peviously investigated by DESI. The oxidized porous silicon surface gave the lowest ionization efficiency compare to all the surfaces, even when compared to the flat nonporous silicon surface, which helped us to conclude that the ionization efficiency is affected by both the porosity and the surface chemistry.

Hydrophobicity allows the droplet to be concentrated on small sampling area, which increases the amount of the sample that is desorbed and ionized by DESI. Conversely, the oxidized porous silicon surface, the sample droplet spread into wide sampling area causing only small amount of the sample to be desorbed and ionized. Also from our pore wetting/filling experiments, we detected that no pore filling occurred for the hydrophobic surface, which means that the small molecules are concentrated at the top of the substrate and are easily desorbed by the spray solvent. This also means that the majority of the sample will be desorbed and ionized into secondary droplets, transferred into the inlet and then detected by the mass spectrometer. Hence we obtained the highest signal intensity along with the lowest limit of detection for the samples with

HFTHDTMS microporous silicon surface. However we observed that the small molecule drugs can and will penetrate into the pores of the hydrophilic surface, and this can also account for the requirement for high flow rate for the spray solvent, and the low ionization efficiency detected. This is due to the fact that most of the sample are in the pores and are not easily desorbed and ionized for detection. It is important to note that for DESI-MS imaging, a methodology is required for analysis of soft biological molecules on our functionalized porous silicon surfaces. This methodology can include imprinting or blotting of the tissue onto our functionalized porous surface, which can also allow direct analysis of the deposited analyte. Ability to transfer the analyte onto the porous silicon surface and their stability over long period of time will make it an ideal substrate for DESI-MS imaging. However, successful fungi imprinting on our porous silicon surface yielded the highest signal intensity when employing an unmodified mesoporous silicon, compared to all other investigated surfaces [Tata et al., 2015]

The surface chemistry of the porous silicon can be tailored to improve selectivity and sensitivity of DESI-MS analysis. This would also require tailoring the spray solvent to the analyte on the surface. Whereby hydrophilic spray solvent will desorb and ionize hydrophilic analyte, however the spray solvent might have a stronger interaction with surface depending on the surface chemistry. Therefore determining the optimal combination of surface chemistry of the porous silicon to analyte and to spray solvent that will lead to successful DESI-analysis is a critical aspect of using this technique.

Reference

Anderson, R.C., Muller, R.S., Tobias, C.W. *Sens. Actuators, A.* 21-23: 835-839 (1990).

Anglin, E.J., Cheng, L., Freeman, W.R; Sailor, M.J. *Adv. Drug. Deliv. Rev*. 60: 1266-1277 (2008).

Badu-Tawiah, A., Bland, C., Campbell, D., Cooks, R.G. *J Am Soc Mass Spectrom*. 21: 572-579 (2010).

Badu-Tawiah, A., Cooks, R.G. *J Am Soc Mass Spectrom.* 21: 1423-1431 (2010).

Bahr, U., Deepe, A., Karas, M., Hillenkamp, F, Giessmann, A. *Anal chem*. 64: 2866-2869 (1992).

Beale, M.I.J., Benjamin, J.D., Uren, M.J., Chew, N.G., Cullis, A.G. *J. Cryst. Growth*. 73: 622-636 (1985).

Ben Jaballah, A., Saadoun, M., Hajji, M., Ezzaouia, H., Bessais, B. *Appl. Surf. Sci.* 238: 199-203 (2004)

Bennet, R.V., Gamage, C.M., Fernandez, F.M. *J Vis Exp.* 77: e50575 (2013)

Bisi, O., Ossicini, S., Pavesi, L. *Surface. Science. Reports.* 38: 1-126 (2000).

Blackwood, D.J., Akber, M.F.B.M. *J. Electrochem. Soc.* 153,11: G976-G980 (2006).

Bomchill, G., Halimaoui, A., Herino, R. *Appl. Surf. Sci.* 41-42: 604-613 (1989).

Boukherroub, R., Wojtyk, J.T.C., Wayner, D.D.M. J. *Electrochem, Soc.* 149,3: 59-63 (2002).

Boukherroub, R., Morin, S., Wayner, D.D.M., Lockwood, D.J. *Phys. Stat. Sol.* 182: 117-121 (2000).

Boukherroub, R., Morin, S., Wayner, D.D.M., Bensebaa, F., Sproule, G.I., Baribeau, J.M., Lockwood, D.J. *Chem. Mater.* 13: 2002-2011 (2001).

Brassard, J. D., Sarkar, D. K., Perron, J. *Appl. Sci*. 2: 453-464 (2012).

Buckberry, L., Bayliss, S. *Mater. World,* 7,4: 213-215 (1999).

Buriak, J.M., Allen, M.J. *J. Am. Chem. Soc.* 120,6: 1339-1340 (1998).

Coa, L., Price, T., Weiss, M., Gao, D. *Langmuir.* 24: 1640-1643 (2008).

Canham. L. Handbook of porous silicon: Routes of formation for porous silicon. Springer international publishing. Switzerland. (2014).

Canham, L.T., Cox, T.I., Loni, A., Simons, A.J. *Appl. Surf. Sci*. 102: 4436-441 (1996).

Chen, H., Pan, Z., Talaty, N., Raftery, D., Cooks, R.G. *Rapid Commun. Mass. Spectrom*. 20,10: 1577-1584 (2006).

Chen, H., Talaty, N.N. Takats, Z., Cooks, R.G. *Anal. Chem*. 77: 6915-6927 (2005).

Chen, H., Zenobi, R. *Chimia.* 61: 843-843 (2007).

Coffinier, Y., Boukherroub, R. Surface chemistry of porous silicon. Taylor & Francis Group. (2016).

Cooks, R.G., Ouyang, Z., Takats, Z., Wiseman, J.M. *Science.* 311: 1566-1570 (2006).

Cooks, R.G., Ifa, D.R., Sharma, G., Tadjimukhamedov, F.K., Ouyang, Z. *Eur. J. Mass Spectrom.* 16: 283-300 (2011).

Cotte-Rodriguez, I., Takats, Z., Talaty, N, Chen H.; Gologan, B., Cooks, R.G. *Anal chem*. 77: 6755-6764 (2005).

Dancil, K.P.S., Greiner, D.P., Sailor, M.J. *J. Am. Chem. Soc.* 121,34: 7925-7930 (1999).

Dill, A.L., Eberlin, L.S., Zheng, C., Costa, A.B., Ifa, D.R., Chen, L.A., Masterson, T.A., Koch, M.O., Vitek, O., Cooks, R.G. *Chem. Eur. J.* 17: 2897-2902 (2011).

Dill, A.L., Ifa. D.R., Manicke, N.E., Costa, A.B., Ramos-Vara, J.A., Knaapp, D.W., Cooks, R.G. *Anal. Chem.* 81: 8758-8764 (2009).

Dillon, A.C., Gupta, P., Robinson, M.B., Bracker, A.S., George, S.M. *J. Electron. Spectrosc. Relat. Phenom*. 54-55: 1085-1095 (1990).

Douglass, K.A., Jain, S., Brandt, W.R., Venter, A.R. *J. Am. Soc. Mass Spectrom*. 23,11: 1896-1902 (2012).

Eberlin, L.S., Dill, A.L., Golby, A.J., Ligon, K.L., Wiseman, J.M., Cooks, R.G. *Angew Chem Int Ed.* 49: 5953-5956 (2010).

Eberlin, L.S., Ifa, D.R., Wu, C., Cooks, R.G. *Angew Chem Int Ed*. 49: 873-876 (2010).

Eberlin, L.S., Ferreira, C.R., Dill, A.L., Ifa, D. R., Cooks, R.G. *Biochimica et Biophysica Acta*. 1811: 946-960 (2011).

Fenn, J. B., Mann, M., Meng, C.K., Wong, S.F., Whitehouse, C.M. *Mass spectrometry reviews*. 9: 37-70 (1990).

Föll, H., Christophersen, M., Carstensen, J., Hasse, G. *Mater. Sci. Eng*. R39: 93-141 (2002).

Ge, M., Rong, J., Fang, X., Zhou, C. *Nano Lett.* 12: 2318-2323 (2012).

Gole, J.L., Seals, L.T., Lillehei, P.T. *J. Electrochem. Soc.* 147,10: 3785-3789 (2000).

Green, F.M., Salter, T.L., Gilmore, I.S., Stokes, P., O'Connor, G. *Analyst.* 135: 731-737 (2010).

Groen, J.C., Preffer, L.A.A., Perez-Ramirez, J. *Microporous and Mesoporous Materials.* 60, 1-17 (2003).

Gross, J.H. Mass spectrometry: 13 Ambient Mass Spectrometry, 2nd edition, springer-Verlag Berlin Heidelberg, 621-649 (2011).

Haapala, M., Pol, J., Saarela, V., Arvola, V., Kotiaho, T., Ketola, R.A., Franssila, S., Kauppila, T.J., Kostiainen, R. *Anal Chem*. 79: 7867-7872 (2007).

Haddad, R., Sparrapan, R., Eberlin, M.N. *Rapid Commun. Mass Spectrom.* 20: 2901-2905 (2006)

Harraz, F.A. *Sensors and Actuators B.* 202: 897-912 (2014).

Hofmann, A., Simon, A., Grkovic, T., Jones, M. *Methods of Molecular Analysis in Life Science*. Cambridge University Press. Cambridge. (2014).

Huang, Z., Geyer, N., Werner, P., Boor, J., Gosele, U. *Adv. Mater.* 23: 285-308 (2011).

Ifa, D.R., Eberlin, L.S. *Clinical Chem.* 62,1: 111-123 (2016).

Ifa, D.R., Wu, C., Ouyang, Z., Cooks, R.G. *Analyst.* 135,4: 669-681 (2010).

Ifa, D.M; Srimany, A., Eberlin, L.S., Naik, H.R., Bhat, V., Cooks, R.G., Pradeep, T. *Analytical Methods*. 3: 1910-1912 (2011).

Ifa, D.R., Jackson, A.U., Paglia, G., Cooks, R.G. *Anal. and Bioanl. Chem*. 394,8: 1995-2008 (2009).

Ifa, D.R., Manicke, N.E., Dill, A.L., Cooks, R. G. *Science*. 321: 805-805 (2008).

Justes, D.R., Talaty, N., Cotte-Rodriguez, I., Cooks, G.R. *Chem. Commun.* 21: 2142-2144 (2007).

Karlsson, L.M., Tengvall, P., Lundstrom, I., Arwin, H. *J. Colloid Interface Sci*. 266: 40-47 (2003).

Kauppila, T. J., Talaty, N, Salo, P.K., Kotiaho, T., Kostiainen, R., Cooks, R.G. *Rapid Commun. Mass Spectrom*. 20: 2143-2150 (2006).

Kingman, S. *Drug Dicovery Today*. 6, 23: 1186-1187 (2001).

Korotchenkov, G. *Porous silicon characterization and application.* Taylor & Francis Group. (2016).

Korotchenkov, G., Cho, B.K. *Crit. Rev. Sol. St. Mater. Sci.* 35,3: 153-260 (2010).

Kumar, P., Huber, P. *J. Nanomaterials.* Vol. 2007, Article ID 89718, 4 pages (2007).

Lehmann, V. *Electrochemistry of Silicon., Instrumentation, Science, Materials and Applications*. Wiley-VCH. Weinheim. Germany, (2002).

Lehmann, V., Gosele, U. *Appl. Phys. Lett.* 58: 856, (1991).

Letant, S.E., Content, S., Tan, T.T., Zenhausern, F., Sailor, M.J. *Sen. Actuator B.* 69,1-2: 193-198 (2000).

Levchenko, V.I., Postrova, L.T., Vorozov, N.N., Yakovtseva, V.S., Dolgyi, L.N*., Thin Solid Films*. 348: 141-144 (1999).

Lewis, W.G., Shen, Z., Finn, M.G., Siuzdak, G. *Int. J.Mass spectrum*. 226: 107-116 (2003).

Manickem, N.E., Wiseman, J.M, Ifa, D.R., Cooks G.R. *J Am Soc Mass Spectrom*. 19: 531-543 (2008).

Mayne, A.H., Bayliss, S.C., Barr, P., Tobin, M., Backberry, L.D. *Phys. Stat. Sol. (a)* 182: 505-513 (2000).

McDonnell, L.A., Heeren, R.M.A. *Mass Spectrom Rev*. 26: 606-643 (2007).

McDonnell, L.A*.,* Heeren R.M.A*.,* De Lange, R.P.J*.,* Fletcher, I.W. *J Am Soc Mass Spectrom.* 17*:* 1195-1202 (2006).

McEwen, C.N., Mckay, R.G., Larsen, B. S. *Analytical Chemistry*. 77: 7826-7831 (2005).

Mengistu, T.Z, DeSouza, L., Morin, S. *Chem. Commun*. 5659-5661 (2005).

Mirabelli, M.F., Ifa, D.R., Sindona, G, Tagarelli, A. *J. Mass Spectrom.* 50: 749-755 (2015).

Neiderhauser, T.L., Lua, Y.Y., Sun, Y., Jiang, G.L., Strossman, G.S., Pianetta, P.,

Lindford, M.R. *Chem. Mater.* 14, 1: 27-29 (2002).

Nemes, P.; Vertes, A. *Analytical Chemistry*, 79: 8098-8106 (2007).

Ogata, Y.H., Yoshimi, N., Yasuda, R., Tsuboi, T., Sakka, T., Otsuki, A. *J. Appl. Phys.* 90: 6487-6492 (2001).

Ohji, H., French, P.J., Tsutsumi, K. *Sesns Actuator*. 82: 1254-1258 (2000).

Orosco, M.M., Pacholski, C., Sailor, M.J. *Nature Nanotech.* 4: 255-258 (2009).

Ovchinnikova, O.S., Nikiforov, M.P., Bradshaw, J.A. Jesse, S., Van Berkel, G.J. *ACS Nano*. 5:5526-5531 (2011)

Parkhutik, V.P., Glinenko, L.K., Labunov, V.A. *Surf. Technol.* 20: 265 (1983).

Petrova-Koch, V., Muschink, T., Kux, A., Meyer, B.K., Koch, F., Lehmann, V. *Appl. Phys. Lett*. 61: 943-945 (1992).

Pirasteh, P., Charrier, J., Soltani, A., Haesaert, S., Haji, L., Godon, C., Errien, N. *Appl. Surf. Sci.* 253, 1999-2002 (2006).

Qu, Y., Zhou, H., Duan, X. *Nanoscale.* 3: 4060-4068 (2011).

Ratcliffe, L.V.; Rutten, F.J.M.: Barrett, D.A.; Whitmore, T.; Seymour, D.; Greenwood, C.; Aranda-Gonzalvo, Y.; Robinson, S.; McCoustrat, M. Analytical chemistry, 79: 6094-6101 (2007).

Ressine, A., Marko-Varga, G., Laurell, T. *Biotechnol. Ann. Rev*. 13: 1-52 (2007).

Rieger, M.M., Kohl, P.A. *J. Electrochem. Soc*. 142: 1490-1495 (1995).

Riikonen, J., Salomaki, M., Van Wonderen,J., Kemell, M., Xu, W., Korhonen, O., Ritala, M., Macmillan, F., Salonen, J., Lehto, V. *Langmuir*. 28: 10573-10583 (2012).

Ronci, M., Rudd, D., Guinan, T., Bennkendorff, K., Voelcker, N.H. *Anal chem.* 84: 8996-9001 (2012).

Ruminski, A.M, King, B.H., Salonen, J., Snyder, J.L., Sailor, M.J. *Adv. Funct. Mater.* 20, 17: 2874-2883 (2010).

Sailor, M.J. Porous silicon in Practice Wiley-VCH, Weinheim. (2012).

Salhi, B., gelloz, B., Koshida, N., Patriarche, G., Boukherroub, R. *Phys. Status. Solidi A-Appl. Mater.* 204,5: 1302-1306 (2007).

Sampson, J.S.; Haawkridge, A.M; Muddiman, D.C. *Journal of the American society for mass spectrometry*. 17: 1712-1716 (2006).

Schwab, N.V., Ore, M.O., Eberlin, M.N., Morin, S., Ifa, D.R. *Anal Chem.* 86: 11722-11726 (2014)

Sen, A. K., Nayak, R., Darabi, J., Knapp, D. R. *Biomed Microdevices.*10: 531-538 (2008).

Shiea, J.; Huang, M.Z.; Hsu, H.J.; Lee, C.Y.; Yuan, C.H.; Beech, I.; Sunner, J. *Rapid comm in mass spec*. 19: 3701-3704 (2005).

Smith, R.L., Collins, S.D. *J. Appl. Phys. Lett*. 71: 1 (1992).

Smith, R.L., Chuang, S.F., Collins, S.D. *J. Electron. Mater.* 17: 228 (1988).

Stuart, H.B. Infrared Spectroscopy: Fundamentals and Applications. John Wiley & Sins Ltd. England. (2004).

Stoeckli, M., Staab, D., Schweitzer, A. *Int J Mass Spectrom.* 260: 195-202 (2007)

Stoeckli, M., Farmer, T.B., Caprioli, R.B. *J Am Soc Mass Spectrom.* 10: 67-71 (1999)

Stweart, M.P., Buriak, J.M. *Angew. Chem. Int. Ed. Engl.* 37,23: 3257-3260 (1998).

Takats, Z., Cotte-Rodriguez, I., Talaty, N., Chen, H., Cooks, R.G. *Chem commun*. 1950-1952 (2005).

Takats, Z., Wiseman, J.M, Cooks, R.G. *J. Mass Spectrom.* 40: 1261-1275 (2005).

Takats, Z., Wiseman, J.M., Gologan, B., Cooks, R.G. *Science.* 306: 471-473 (2004).

Talaty, N., Takats, Z., Cooks, R.G. *Analyst.* 130: 1624-1633 (2005).

Tata, A., Perez, C.J., Ore, M.O., Lostun, D., Passas, A., Morin, S., Ifa, D.R. *RSC Adv*. 5: 75458-75464 (2015).

Trauger, S.A., Go, E.P., SHen, Z., Apon, J.V., Compton, B.J., Bouvier, E.S.P., Finn, M.G., Siuzdak, G. *Anal. Chem.* 76: 4484-4489 (2004)

Uhlir Jr, A. *Bell Syst. Tech. J.* 35: 333-347 (1956).

Unagami, T. *J. Electrochem. Soc.* 127: 476 (1980).

Vazsonyi, E., Szilagyi , E., Petrik , P., Horvath, Z.E., Lohner, T., Fried, M., Jalsovszky, G. *Thin Solid Films.* 388: 295-302 (2001).

Venter, A., Sojka, P.E., Cooks R.G. *Anal Chem.* 78: 8549-8555 (2006).

Venter, A., Cooks, R.G. *Anal Chem.* 79: 6398-6403 (2007).

Wei, J., Buriak, J.M., Siuzdak, G. *Nature,* 20: 243-246 (1999).

Wiseman, J.M., Ifa, D.R., Song, Q.Y., Cooks, R.G. *Angew Chem Unt Ed.* 45: 7188-7192 (2006).

Wiseman, M., Laughlin, B.C. *Current separation*. 22: 11-14 (2007).

Wiseman, M., Puolitaival, M., Takats, Z., Cooks, R.G., Capriolli, R.M. *Angew. Chem.* 117: 7256-7259 (2005).

Wiseman, J.M., Ifa, D.R. Zhu, Y., Kissinger, C.B., Manicke, N.E., Kissinger, P.T., Cooks, R.G. *PNAS.* 105,47: 18120-18125 (2008).

Wu, C.P., Dill, A.L., Eberlin, L.S., Cooks, R.G., Ifa D.R. *Mass. Spec. Rev*. 32, 3: 218-243 (2013).

Wu, C.P., Ifa, D.R., Manicke, N.E., Cooks, R.G. *Anal Chem*. 81: 7618-7624 (2009).

Xu, Y.K., Adachi, S. J. Phys. D: Appl. Phys. 39: 4572-4577 (2006).

Xu, S., Pan C., Hu, L., Zhang, Y., Guo, Z., Li, X., Zou, H. *Electrophoresis*. 25: 3669-3676 (2004).

Yanes, O., Woo, H., Northen, T.R., Oppenheimer, S.R., Shriver, L., Qpon, J., Estrada, M.N., Potchoiba, M.J, Steenwyk, R., Manchester, M., Siuzdak,G. *Anal Che*m. 81,8: 2969-2975 (2009)

Zhang, X.G. *J. Electrochem. Soc.* 151,1: 69-80 (2004).

Zhang, X.G., Collins, S.D., Smith, R.L. *J. Electrochem. Soc.*136: 1561 (1989).

Zhang, X.G. *J. Electrochem. Soc*. 138: 370 (1991).

Zhou, W., Apkarian, R.P., Wang, Z.L., Joy, D. Fundamentals of Scanning Electron Microscopy, Chapter 1, in Zhou, W., Wang, Z.L. *Scanning Microscopy for nanotechnology; Techniques and Applications.* Springer New York. (2007).

Zimin, S.P., Preobrazhensky, M.N., Zimin, D.S., Zaykina, R.F., Borzova, G.A., Naumov, V.V. *Infrared. Phys. & Technology.* 40: 337-342 (1999).

Part II: Atomic Force Microscopy Investigation of Biological Molecules

Chapter Eight

Introduction

8.1 Analytical Methods for Study of Biological Molecules

Different analytical techniques have been developed and are suitable for the analysis of biomolecules. Most of these techniques require sample preparation and treatment, which can alter the structure and hence the function of the molecules of interest. The technique utilized the most by biochemist involves electrophoresis separation of DNA molecules, proteins, RNA molecules and protein-DNA complexes. The separation is based on size, molecular weight and charge. Two common methods are electro mobility shift assay (EMSA), which separates loose DNA and proteins from protein-DNA complexes through electrophoresis, while DNase 1 footprint allows the determination of base recognition of DNA binding proteins. DNase I enzymes digest DNA fragments, while the sites bound by the protein are protected from degradation, and appear as a gap in the continuous array of bands of digested DNA fragments [Dey et al., 2012].

Other analytical techniques for analysis of molecules include nuclear magnetic resonance (NMR), which requires atoms with ½ spin nuclei for detection. Also popular in the field of bioanlaysis is the use of ultraviolet/visible spectroscopy (UV/Vis), however

this depends largely on the molecule of interest containing chromophores. On the other hand fluorescence spectroscopy/microscopy involves treatment of the molecule of interest with fluorophores for detection [Hofmann et al., 2014, Dey et al., 2012]. Other methods such as centrifugation, light scattering, and isothermal titration calorimetric can allow investigation of molecules in solution. However, the concentrations required might exceed the range that would be considered biologically relevant [Dey et al., 2012]. Other techniques, such as X-ray crystallography, and electron microscopy require extensive sample preparations. In addition, surface sensitive techniques such as surface plasmon resonance require molecules to be tethered to the surface [Hofmann et al., 2014]. Most studies of biomolecules, including proteins and DNA, using techniques like X-ray crystallography and NMR have provided vast amount of information. However understanding protein structure and function in biological processes requires studying of it dynamic function, i.e. complex processes, such as DNA interactions. These dynamic processes are extremely hard to obtain via the above mention techniques, which also does not allow for investigation of the protein in its near-native environment.

Atomic force microscopy is a technique that can allow analysis of samples with minimal sample preparation. It allows investigation of biological molecules in near-native conditions. AFM is a remarkable technique that allows one to visualize and measure surface features with extraordinary resolution. It is a force-based technique that makes use of a sharp tip attached to a flexible cantilever to scan over the surface of the sample.

The greatest advantage of AFM is the ability to image almost all types of sample, from hard metallic surfaces, to soft biological molecules [Gahlin and Jacobson, 1998; Yang et al., 2003]. AFM allows us to obtain images of samples ranging from individual

atoms, to a whole array of cells [Rode et al., 2009; Alessandrini and Facci, 2005; Jalili and Laxminarayana, 2004]. AFM is not only an imaging tool, but it is a technique that comes with spectroscopy modes for measuring other important properties of a surface such as adhesion forces and elasticity [Alessandrini and Facci, 2005].

Binning, Quate and Gerber first introduced AFM in 1986 as another member of the scanning probe microscopy (SPM) family that first included a technique known as scanning tunnel microscopy (STM) [Binning et al., 1986]. SPM instruments make use of interactions between a probe and a surface to produce the topography of the sample surface. The predecessor of AFM, scanning tunnelling microscope requires the sample and the probe to be conductive or semi-conductive, which is a limitation towards all other types of samples. The AFM does not require conductive sample or probe and are built with the capability to provide much more information than just topography. This is why it has become a universal instrument being utilized in many areas of science. When compared to other microscopy techniques, such as optical microscopy, transmission and scanning electron microscopy, AFM covers the disadvantages of all these techniques: extensive sample preparation, limitation on sample that can be investigated, requirement of expensive coating, high vacuum and low spatial resolution. In addition, AFM can be operated in air, vacuum and in liquids, it requires little to no sample preparation, it can characterize biological sample in-vitro under physiological conditions and yield good topographic contrast [Yang et al., 2003]. AFM provides high-resolution structural images when compared to all the other techniques.

Atomic force microscopy is becoming a powerful tool for obtaining structural details and biomechanical properties of biomolecules and cells [Vahabi et al., 2013].

AFM have been used for imaging of bacteria cells [Miller et al., 2006; Del sol et al., 2007], plant virus morphology such as tobacco mosaic virus and other viruses [Kuznetsov et al., 2008, 2011]. The effect of antibiotic beta-lactam on bacteria was also studied by AFM [Yang et al,. 2006]. One of the biological molecules most visualized by AFM is DNA [Rivetti et al., 1996, 1999; Bustamante et al., 1992, 1993, 1996; Erie et al., 1994, Guthold et al., 1999; Leung et al., 2012]. An interesting aspect of DNA investigation is the use of DNA self-assembly ability to form different structures, such as DNA tiles [Seeman, 1998], and also as nano machinery such as rotaxanes [Ackermann et al., 2012]. In addition, AFM has been used to study chromatin and chromosome structures in solution. [Hoshi and Ushiki, 2011]

Besides its use to elucidate structures, AFM has been employed to study specific and non-specific protein-DNA interactions [Hansma et al., 1993]. Mapping of protein binding location along DNA, and measurement of DNA bend angle were performed by AFM [Erie et al., 1994]. DNA wrapping by the bound protein was implied indirectly by comparison of length of free DNA with DNA complexes [Rivetti et al., 1999]. Looping of long strand DNA due to binding of NtrC transcription factor was visualized by AFM [Wyman et al., 1997]. Development of high speed AFM allowed for real-time observation of protein-DNA interaction [Rajendra et al., 2014]. This included the association and dissociation of streptavidin with biotinylated DNA strand [Kobayashi et al., 2007], and DNA digestion by the restriction endonuclease enzyme ApaI [Yokokawa et al., 2006]. Investigation of *Escherichia coli* RNA polymerase (RNAP) transcription activity shows that upon addition of nucleoside triphosphate, a new strand of DNA sliding through the protein bound to mica was observed [Guthold et al., 1999].

AFM have been also used for the investigation of living cells and tissue conditions. It allows investigation of mRNA expression in living cell without causing cell death. This method involves the insertion of the AFM tip into the living cell, and extraction of the mRNA [Uehara et al., 2004]. AFM was used for study specific interactions between RNA molecules, such as circularization of single strand RNA overhang of dengue virus genomic RNA. The method used was to introduce double stranded RNA in the middle of the strand while leaving the edges as single stranded RNA [Alvarez et al., 2005]. As well for probing of kissing loop interaction due to RNA-RNA base pairing [Hansma et al., 2003]. It was also used for visualization of genomic RNA molecule [Kuznetsov et al., 2005]. In addition, AFM base force spectroscopy is a powerful tool to study the rupture of molecular bond, unfolding of proteins [Fernandez and Li, 2004], and nucleic acid [Krautbauer et al., 2003]. It has also been used in biomedical applications [Carvalho and Santos, 2012], and for investigation of the degree of stiffness in cancer cells [Cross et al., 2007]. Researchers are utilizing many benefits of AFM, i.e., its high resolution, minimal sample preparation, real time investigation, and non-destructive imaging, and ability to image in liquids to investigate various biomolecules and biomaterials [Vahabi et al., 2013]. In this thesis, a similar approach was employed to investigate biomolecules from two different pathogens, namely *Staphylococcus aureus* and tomato bushy stunt virus (TBSV), which are discussed in next section.

8.2 A two-component signaling transduction system mediates antibiotic resistance in *Staphylococcus Aureus*.

In the early 2000's, there were reports of vancomycin resistant *staphylococcus aureus* (VRSA) being isolated in various parts of the world. This was of great concern because the bacteria (VRSA) exhibited complete resistance to the antibiotics use as treatment for inhibition of cell wall synthesis. The vancomycin resistance of VRSA Mu50, the strain with high resistance towards the antibiotic was reported to include extensive cell wall thickening through the increase peptidoglycan production [Hanaki, 1993; Hiramatsu, 2001]. Extensive studies were carried out on vancomycin resistance of *S. aureus* to elucidate the genetic basis of the resistance. It was proposed that *S. aureus* responds to inhibition of the cell wall biosynthesis by increasing regulation of a unique set of genes, leading to overproduction of proteins involved in a different step of bacteria cell wall biosynthesis [Kuroda et al., 2000].

Kuroda et al. has identified an increase and decrease in expression of the novel gene in *S. aureus* Mu3 and Mu50. The increase in regulation of novel genes designated vancomycin resistant associated gene (*vra)* is what is of interest, specifically the vancomycin resistant associated regulatory protein gene (*vraR*). The discovery of over-expression of a novel two-component system (TCS) designated as *vraSR gene* lead to an essential insight into the resistance mechanism utilized by *S. aureus.* Introduction of a sub-clone of this gene into a vancomycin susceptible cell was observed to raise the resistance level of the cell to vancomycin [Kuroda et al., 2000]. It was later discovered that VraSR (vancomycin-resistance associates sensor/regulator) coordinated the genetic

response to antibiotic resistance in *S. aureus* via two-component phosphotransfer-signaling pathway [Kuroda et al., 2003; Yin et al., 2006].

It is well know that bacteria utilize sensing and signal transduction machineries to adapt to changes in their environment. In addition, two-component signal transduction systems are wide spread in different organisms, such as bacteria, archae, yeast and plants [Casino et al., 2010]. Bacteria, including antibiotic resistant ones, also make use of two-component system to sense and respond adequately to the presence of stimuli, such as antibiotics. Typically, a two-component system is composed of a sensor kinase and a response regulator. A sensory kinase is a membrane-bound histidine kinase that senses stimuli. The response regulator is a cytoplasmic protein, which mediates the output of the signal generally a regulation of novel gene expression. Two-component signal transduction occurs through phosphorylation and dephosphorylation processes between the histidine kinase and the response regulator [Jung et al., 2012].

The two-component system identified for vancomycin resistance *staphylococcus aureus* are labeled as vancomycin resistant associated regulatory (VraR) and sensory (VraS) proteins. VraR catalyzes the transfer of phosphoryl group from phosphorylated histidine residue of VraS to a conserved aspartate residue in its own regulatory domain. VraR can also transfer phosphoryl groups from small molecules, such as acetyl phosphate [Belcheva et al., 2008]. However, the rates are much slower than the transfer of phosphoryl group from its cognate pair VraS. Others make use of beryllium fluoride, a compound that binds tightly to VraR and mimics phosphorylation [Donaldson, 2008,;Leonard et al., 2013]. The phosphorylation site of VraR was confirmed to be aspartate 55 residue, and upon phosphorylation the equilibrium shifts towards the active

state (ON) as shown in Figure 8.1; hence facilitating specific DNA interactions [Belcheva et al., 2008, 2009]. VraSR two-component system regulates expression of 40 different genes in *S. aureus* among those are genes exposed to cell wall biosynthesis inhibitors [Kuroda et al 2003].

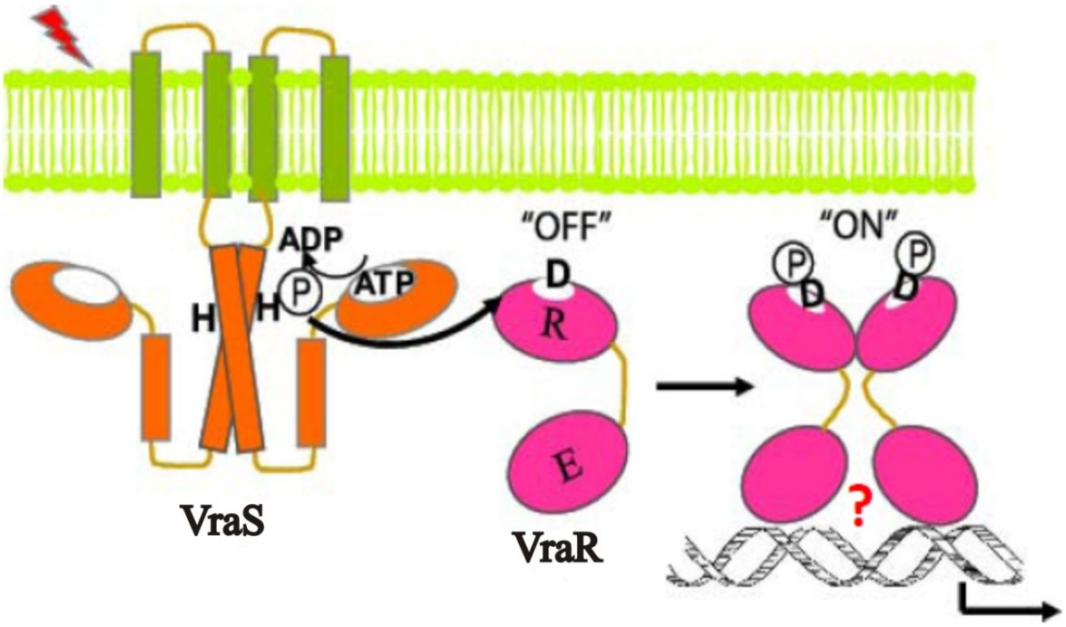

Figure 8.1: Schematic representation of the two-component system VraS and VraR phosphotransfer mediated signaling pathway. Illustrated is the N-terminal spanning domain, the C-terminal dimerization domain containing the ATP-binding domain and conserved histidine residue of VraS (HK) as well the regulatory domain (R) and effector domain (E) of VraR (RR). Also illustrated are the two-phosphorylation process and the conformation change from OFF to ON state of VraR [Belcheva *et al* 2008].

VraR response regulatory protein is known to regulate its own gene expression by binding to the *vraSR* operon, which is a group of genes physically linked and under the control of same promoter as shown in Figure 8.2. VraR binds to DNA sequence within the region of the transcription start point (tsp) (Fig 8.2). It has been shown that unphosphorylated VraR is able to bind to the DNA control region of *vraSR* operon, suggesting that DNA binding is phosphorylation independent [Belcheva et al., 2009]. Sequence comparison of VraR with other response regulatory protein and NMR studies suggests that this protein belongs to the NarL/FixJ subfamily of protein [Donaldson, 2008]. This protein is believed to use helix-turn-helix motif to bind DNA. Each member of the subfamily recognized unique DNA sequence and utilizes different regulatory strategies. Using AFM we have recently demonstrated direct visualization of VraR binding to the *vraSR* promoter operon control region (*vraSRp*). Controlled experiments show that these are site-specific interactions, because no binding was observed for VraR with mutated DNA at the binding site [Ore, 2010].

Figure 8.2: A representation of the *vraSR* operon composition in the *of S. aureus* strain Mu50. One can see the control region for the operon, the transcription start point (tsp), and *vraS*, *vraR* gene. Shown also are the neighboring *map* gene adapted from [Belcheva et al., 2008].

In this thesis our research was to understand binding of phosphorylated VraR with the *vraSR* operon control region, since *in vivo*, gene regulation by VraR involves phosphorylation. Atomic force microscopy was used for direct visualization of the DNA interaction of phosphorylated VraR to further understand the gene regulation mechanism utilized by VraR protein from *S. aureus*. Knowing the regulatory mechanism utilized by VraR protein is essential to understanding the antibiotic resistance mechanism of *S. aureus*.

8.3 Global organization of tomato bushy stunt viral RNA

Viruses are infectious pathogens that can only survive by depending on living cells as host for replication. The simplest viruses are composed of small pieces of nucleic acid surrounded by a protein coat. The complete intact virus particle is called a virion. Viruses also store their genetic information in their nucleic acids, which can either be a deoxyribonucleic acid (DNA) or ribonucleic acid (RNA). Positive-strand RNA viruses are significant pathogens, which comprise over one-third of all virus genera [Ahlquist et al., 2003]. Upon entry into host cell, the positive strand RNA virus genome is translated into essential viral proteins, subsequently it acts as template for genome RNA replication for new progeny viral genomes [Gamarnik and Andino, 1998]. In the genome of positive stranded RNA virus is the gene that encodes for RNA dependent RNA polymerase (RdRp), which is required for genomic replication. Therefore, replication of positive stranded RNA virus cannot commence until the genomic RNA is translated to produce RNA polymerase protein. It has been revealed that several host factors (HF) are involved in the replication process of the viral genome [Ahlquist et al., 2003].

Tomato bushy stunt virus (TBSV) is a positive sense RNA virus with replication processes similar to other viruses, such as humans and animal viruses [Pogany et al., 2003]. This makes it a suitable candidate for study of viral infection process. TBSV form an isometric particle and has a spherical structure, which is based on icosahedron. Tomato bushy stunt virus infects plants, specifically tomatoes. It causes stunting in the growth of leaf and deformed or absent fruits. TBSV genomic RNA consists of coding regions, which serve as blue print for viral RNA replication, and for vital viral proteins [Wu et al., 2013]. The genome of TBSV is a single-stranded positive-sense RNA of ~4.8kb [Hearne, 1990; Oster et al., 1998]. TBSV genome illustrated in Figure 8.3, is known to encode five functional proteins. The p33 codes for a 33kDa protein revealed to be involved in the viral RNA replication. The coding region p92 codes for a larger protein of 92kDa, which is the viral RNA-dependent RNA polymerase (RdRp). The p33 and p92 are translated directly from the viral genome, whereas the other coding regions labeled as p41, p22, and p19 are translated from two sub-genomic (Sg) mRNAs that are transcribed during infections. The smaller Sg2 mRNA is produced first and serves as template for translation of p22 and p19, the movement protein and the suppressor of gene silencing [Oster et al 1998; Fabian and White, 2004]. The Sg1 mRNA is transcribed later in the infection and it directs translation of 41kDa coat protein [White and Nagy, 2004].

Viral RNA is single stranded, however, due to short and long range RNA-RNA interactions, the structural concept of a functional viral RNA genome is shifting from that of a “linear” molecule to one that is three dimensional. Our collaborator Prof. A. White (Biology, York University) revealed RNA-RNA interactions occur within the TBSV

RNA, and has proposed a high-order structure involving, six long-range interactions [Wu et al., 2009].

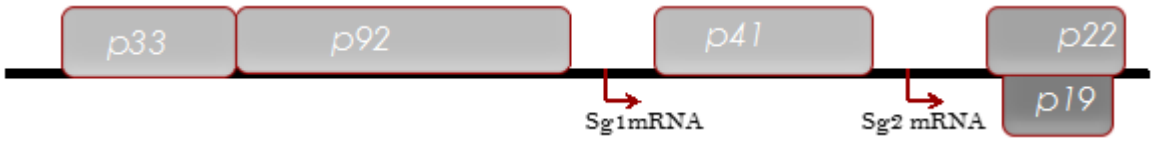

Figure 8.3: Schematic representation of tomato bushy stunt viral genome. The genome is the thick horizontal line, with coding regions depicted as boxes, which included the approximate molecular weight in kDa of the encoded proteins adapted from [Nicholson and White, 2014]

Two of the long-range RNA-RNA interactions are involved in translation to proteins (p92 and p33). These two proteins form the viral replicase complex of the tomato bushy stunt virus. One long-range interaction domain is essential for the full genomic replication. The last three long-range interaction domains lead to transcription of two different types of sub-genomic messenger RNA (mRNA) [Wu et al., 2009]. We investigated the genome architecture of TBSV using high resolution AFM, in order to gain a better understanding of how the multiple long-range interactions are accommodated and functionally integrated within the genome. Imaging and visualization of the genomic structure of the viral RNA is important to understanding the function of the 3D structure.

Chapter Nine

Materials and Methods

9.1 DNA preparation

All material used for DNA preparation was provided by Prof. Golemi-Kotra's lab. The genome of *S. aureus* was obtained from ATCC. The PCR primers were purchase from Sigma. THE ATP was purchased from BioLabs. All other chemical were purchased from Fisher or Sigma. The material preparations that follow was performed by me with initial guidance from Antoaneta Belcheva from Prof. Golemi-Kotra's research group.

The DNA (*vraSRp)* with sequence from region -456 to +150 of *vraSR* operon with theoretical length of 208 nm for a 612bp assuming 0.34nm/bp for a B-form DNA was amplified by polymerase chain reaction (PCR). With PCR, we are able to work with minuscule amount of starting DNA to make over a million copies within 30 cycles. To carry out a PCR experiment, the target DNA sequence is mixed with desired DNA polymerase, a pair of oligonucleotide primers, and a supply of mixture of (ATP, CTP, GTP, and TTP) nucleotides.

PCR reaction for vraSRp is as follows: 34 µL of double distilled water, 5 µL of pfu buffer 10x, 5 µL of dNTP, 2 µL of both the direct and reverse primers, 1 µL of DNA template (50ng) and 1 µL of *pfu* Turbo^{Tm} DNA polymerase. The final volume of the sample reaction is 50 µL and the components were added in order. The reaction condition for *pfu* PCR is as follows; denaturation of template DNA at 95ºC for 150 sec, followed by annealing of the primers to the beginning of the DNA at 65ºC. At 72ºC, this is the

optimum temperature for function of *pfu* polymerase to add the necessary nucleotides. The 612 base pair PCR product was purified from 1% agarose gel and QIAquick Gel extraction Kit (Qiagen). Concentration of DNA was measured at 260 nm using spectrophotometer (Cary 100, Varian Inc.).

9.2 Protein Purification

All material used for the protein expression, purification and protein phosphorylation was provided by Prof. Golemi-Kotra's lab. The chemicals where purchase from Fisher unless otherwise stated. The Growth media were acquired from Fisher. The *E coli* Bl21 (DE3) strains as well as the cloning expression plasmids were purchased from Novagen. The isopropyl β-D-thiogalactopyranoside (IPTG) used fro expression was obtained from Sigma. The Chromatography media and columns were purchase from GE Healthcare. I performed the protein purification process described below with initial guidance from Antoaneta Belcheva from Prof. Golemi-Kotra's research group.

A seed culture of *E. coli* BL21 (DE3) carrying the appropriate expression vector pET26b::*vraR* was added to a 5 mL Luria bertani (LB) medium in presence of kanamycin at final concentration of 50 μg/mL. The seed culture medium was grown overnight. From the seed culture, 1 mL was used to inoculate 600 mL of terrific broth medium containing 50 μg/mL kanamycin. The medium culture was grown for 3 hr at 120 rpm speed, 37°C. At 0.6 OD, protein expression was induced with addition of 0.4mM isopropyl β-D-thiogalactopyranoside. The cells were allowed to express the target protein for 16 hr at 25°C. Cell were harvested by low speed centrifugation at 2,500 xg for 10min and the resulting pellet dissolved in 30 mL of 20 mM Tris pH 7.0 buffer and 5 mM $MgCl_2$. The

cell content was released by sonication and cell debris was removed by centrifugation at 25,000 xg for 60 min. The resulting supernatant was loaded onto a DEAE Sepharose column equilibrated with 20 mM Tris buffer, pH 7.0, 5 mM $MgCl_2$. Target protein (VraR) was eluted between 20-30% of a linear gradient of 500 mM Tris buffer, pH 7.0 and 5 mM $MgCl_2$. Fractions containing the VraR protein were collected and concentrated by Amicon ultracentrifugation membrane (Centriprep Ultracel YM-3, Amicon). The buffer from the protein was exchange with 20 mM Tris buffer, pH 7.0 and 5 mM $MgCl_2$ using desalting column. The protein solution was loaded into a heparin-sepherose affinity column. The target protein (VraR) was eluted from the column with a linear gradient of 50 mM Tris buffer, pH 7.0, and 5 mM $MgCl_2$ between 40-60% of the elution buffer. Sodium dodecyl sulfate polyacrylamide gel electrophoresis (SDS-PAGE) method was used to examine the effectiveness of the purification step for isolation and purity of target protein. Due to the size of the target protein 23.4KDa used for this experiment, a 15% SDS-PAGE gel was prepared.

9.3 Phosphorylation of VraR (VraR-P)

Protein phosphorylation involves the use of a 20 µL solution of 40 µM VraR that was prepared in a phosphate buffer (50 mM Tris-base, pH 7.4, 50 mM KCl, and 20 mM $MgCl_2$) and was supplemented with 50mM lithium potassium acetyl phosphate (Sigma). The reaction was incubated at 37°C for 1hr. The extent of phosphorylation of VraR was monitored by HPLC (Varian Inc.) using a ProSphere^{Tm} HP C4 reverse phase column (5 µm, 300 Å, 4.6 x250 mm). The elution of the protein was carried out between 40-48% of linear gradient of acetonitrile and 0.1% Trifluoroacetic acid (TFA) over 40 min at flow rate 1mL/min. Approximately 65% of the VraR was phosphorylated; this was obtained by

integrating the surface area under the peak corresponding to VraR-P and comparing it with that of the VraR in the absence of phosphorylation. The VraR-P solution was first diluted 40-fold. To prepare the VraR-P sample for imaging with tapping mode AFM in air, the sample was then diluted another 50 fold resulting in a 20 nM VraR-P solution, deposited on freshly cleaved mica surface.

9.4 Sample preparation for AFM

9.4.1 Dilution of DNA and Protein

vraSRp DNA was diluted to desired the concentration by adding deposition buffer (10 mM $MgCl_2$, 20 mM NaCl, 10 mM Tris buffer pH 7.4) to a total volume of 20 µL. For VraR, several dilutions of 50 nM, 25 nM, 10 nM and 5 nM were carried out by adding deposition buffer to obtain less than a monolayer of protein on the surface. Total volume of sample was either 10 µL or 20 µL**.**

9.4.2 Binding reaction

Protocol I: Complex formation on mica surface: The binding reaction of VraR to *vraSRp* was performed in two steps: first a deposition of 20 µL of the *vraSRp* on freshly cleaved mica followed by imaging with the AFM. Then 20 µl of 20 nM VraR on the same mica surface containing the deposited DNA, and was reimaged using the AFM. Depending on the DNA PCR sample, complex formation was also performed*,* 2 nM *vraSRp* with 50 nM VraR and 5 nM *vraSRp* with 50 nM VraR.

Protocol II: Complex formation in solution prior to deposition on mica: Binding reaction (10 µl) was prepared in binding buffer (100 mM Tris buffer, pH 7.5, 50 mM

KCl, and 10 mM DTT) supplemented with 5 mM $MgCl_2$. The binding reaction was incubated for 25 min at 37ºC and 5 µL of binding reaction was quickly diluted to 20 µL with deposition buffer.

9.5 Sample preparation of TBSV genomic RNA

RNA samples were obtained from Prof. White's lab

The RNA sample was diluted to 1.5 ng/µl in deposition buffer (20 mM Hepes, 10 mM $MgCl_2$). 20µl of the diluted RNA sample was deposited on freshly cleaved mica for 30 sec to 1min at room temperature. The sample was rinsed with double distilled water, dried with gently stream of nitrogen gas, and images under AFM tapping mode in air.

9.6 Deposition of sample on mica surface

The deposition protocol for this research is as follow: the sample was first diluted to the desired concentration with the deposition buffer containing Mg^{2+}. Next, a fresh mica surface was prepared by peeling layers of the surface using a sticky tape. The mica utilized in this research was potassium aluminum silicate hydroxide $KAl_2(AlSi_3O_{10})(OH)_2$. The mica was AFM grade red muscovite purchased from Novascan technologies Inc. When immersed in water the K^+ ions diffused away revealing a surface covered with oxygen atoms rendering the mica surface negatively charged. Working with DNA, which has negatively charge backbone of phosphate ion, it will not bind to mica due to the repulsion force. Therefore it is essential to overcome the electrostatic repulsion between the DNA and the mica surface. Mica substrate is the most preferred substrate for imaging because it is easy to cleave and produces atomically smooth surface each time. Weak electrostatic attachment of DNA to mica is achieved by

using divalent cations in buffer. Lyubchenko et al. have also extensively studied DNA deposited on functionalized mica. They specialized in functionalization of mica with silane chemistry as suitable substrate for deposition of biomolecule for AFM imaging. Their main chemical compound is 3-aminopropyl-trietoxy silane (APTES) functionalized mica [Lyubechenko et al. 1992, 2011].

The samples is then deposited onto the fresh mica surface and allowed to incubate for a desired period of time. For our research all sample were incubated on mica for 1min, unless stated otherwise. This time interval has been shown to provide sufficient DNA/RNA coverage from nanomolar concentration. The mica surface containing the sample was rinsed with double distilled water thoroughly to remove salt and loosely bound DNA/RNA, then dried under gently stream of argon to remove remaining water on surface. Once dried, the samples were ready for AFM imaging in air.

9.7 Atomic Force microscopy

9.7.1 Principle and Basic Setup of Atomic Force Microscopy

Atomic force microscopy principle is based on the interaction force between two surfaces, i.e., the cantilever-tip and the sample surface. A schematic diagram of AFM main components is illustrated in Figure 9.1. Atomic force microscopy makes use of a nanofabricated tip mounted at the end of a flexible cantilever (i.e. probe) to scan over a sample in a raster manner, providing surface feature and other information [Meyer and Amer, 1988]. The basic configuration of AFM consists of a cantilever-tip assembly, a scanner, a deflection detecting system, a control system that includes a feedback loop, and a sample holder. A sharp tip at the end of a flexible cantilever feels the force of

interaction which existed, while the scanner controls the tip movement over nanometer scale using a feedback system to adjust the tip vertical position, a four-quadrant photodiode detector monitors the movement and position of the tip over the sample surface via optical beam detection. A controller attached to a computer with display screen for adjusting parameters, viewing and analyzing images controls the electronics (Fig 9.1).

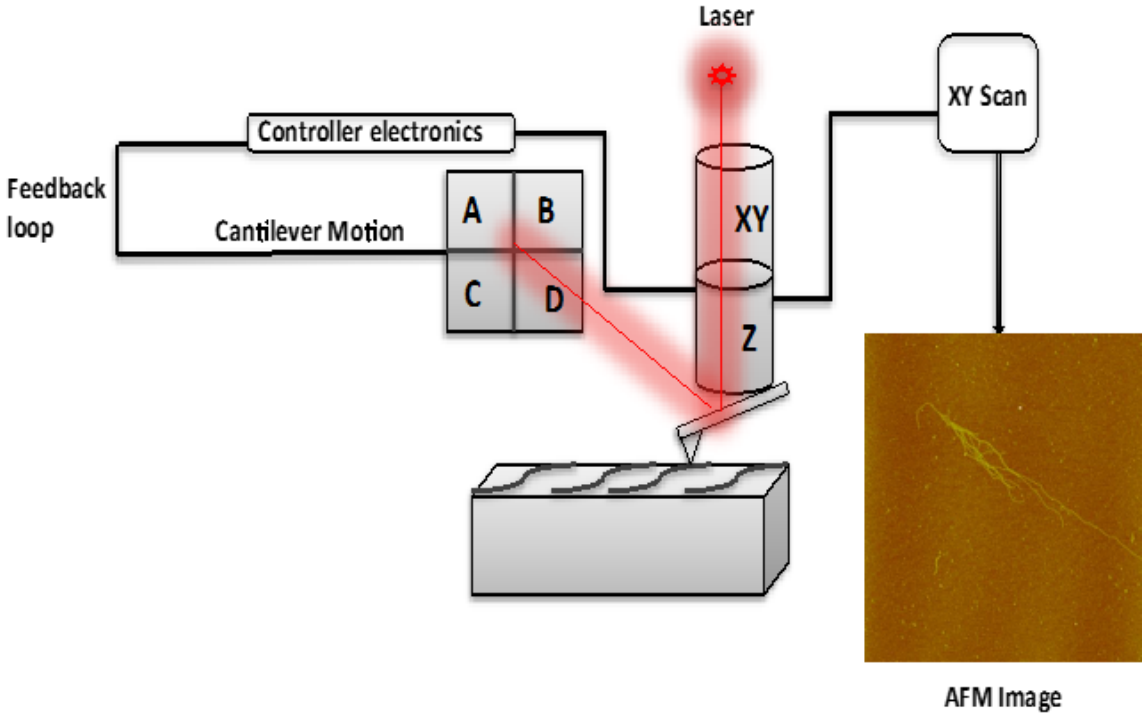

Figure 9.1: A schematic illustration of atomic force microscopy adapted from SPM training book.

AFM is highly sensitive because of the feedback loop, which is used to maintain a set force/height between the probe and the sample [Eaton & West 2010; SPM training book]. In the feedback loop, the input is the deviation from the height/force set point

experienced by the probe due to the topography of the sample surface, while the output is the displacement of the scanner in the z-direction to adjust the position of the probe over the sample surface. There are two models of AFM, where the scanner is either placed beneath the sample or place above the cantilever-tip assemble. In the former model, the sample is scanned and the tip is fixed; while in the later the tip is the scanner. The AFM used in this thesis is the Dimension 3100 microscope, Nanoscope IIIa controller (Digital Instrument Inc., Vecco), which makes use of the later model. The different aspect of the AFM setup will be discussed below.

9.7.2 Cantilever-tip assemble

The cantilever-tip assemble is a very important piece of this instrument, because it is the part of the instrument that is in direct contact with the sample. The probe senses the force across the sample surface and responds to this force by deforming. The most common probe in AFM is the cantilever-tip assemble probe, which are highly suited to measuring the topography of a sample. Cantilever with different coatings are available to measure different properties such as magnetic, electrostatic, and near-field optical properties [Torre et al., 2011]. The cantilever-tip assembly is generally made up of etched silicon (Si) and silicon nitride (Si_3N_4) [Wolter et al., 1991; Akamine et al., 1990]. The type of cantilever-tip assembly used will depend on the imaging mode and the type of sample. However, the radius of curvature and the aspect ratio of the tip are the parameters to consider to optimize the resolution. Commercial tips commonly come with a curvature radius <10 nm, while ultra-sharp tips have radius <2 nm [Torre et al., 2011]. Cantilever length varies and can be in the range of 100-200 μm, while the whole cantilever-chip can be as long as 5-10 mm. The use of carbon nanotubes as AFM tips provides a high aspect

ratio with small radius of 1nm leading to high-resolution imaging. Also, carbon nanotubes provide possibilities for functionalization for attaching chemical groups and biomolecules [Hafner et al., 2001]. AFM image is a convolution of the tip and surface feature, therefore the shape and geometry of the tip is of the utmost importance [Morris 1999, SPM training book]. Etch silicon is used for creating probes with high spring constants. It has tetrahedral tip shape, with a rectangular cantilever. A stiff cantilever with higher spring constant, have a high resonance frequency and are used in tapping mode for imaging of soft samples to overcome surface tension force and reduce noise. Silicon nitride is used for creating probes with low spring constants. It has pyramidal tip shape, with a triangular cantilever. A cantilever with low spring constant has low resonance frequency and a tendency to bend and exert low force. This is used for imaging in contact mode and for tapping mode in liquid. Typical spring constant for AFM cantilevers range from 0.0 1 Nm^{-1} to 100 Nm^{-1}, enabling force sensitivity down to 10^{-11} N [Alessandrini and Facci, 2005]. The silicon probes used in this thesis are from vista probe (T300 and Aspire 300) with force constant 40 Nm^{-1} and a resonance frequency of 250-300 KHz.

9.7.3 Scanner

The scanner is made out of piezoelectric material, which converts electrical potential to mechanical motion. The piezoelectric material can be made to contract or elongate proportional to applied voltage. If they elongate or contract will depend on the polarity of the applied voltage. A conventional AFM scanner makes use of 5 or more independently operated piezo elements. By combining these elements to make one unit, system, makes it possible to manipulate the probe in an extreme precision over a sample

surface. Most AFM scanners are built with short scanner tubes with short piezo elements, which allow for imaging at higher magnification, highly controllable and easier to stabilize. When voltage is applied along the X,Y,Z direction to the electrode of the tubes, it powers the tip to raster scan the sample surface. All piezo elements exhibit a degree of nonlinearity and hysteresis. This nonlinearity can sometimes lead to a distortion of the tubes, known as bowing effect and also requiring the scanner to be calibrated with time [SPM training book]. The scanner system for modern atomic force microscopy use for high-speed imaging has been modified, to reduce vibrations by action of counterbalance method to produce a more compact scanner and increase resonance frequency of the material [Ando et al., 2008]. The scanner specification for the AFM Dimension 3100 microscope, Nanoscope IIIa used in this thesis are; X, Y- axis is 90 μm, Z- axis is 6 μm, electronic resolution of 16-bit (all axis), 1-2% accuracy, orthagonality is 2 degrees [SPM training book].

9.7.4 Detection

Optical lever detection is used in AFM to monitor the cantilever deflection. In this system a laser directed at the back of a reflective cantilever is reflected towards a four-quadrant position sensitive photodiode, which is divided into segment for measurement of vertical and lateral deflections of cantilever (Fig 9.1). The difference between the different sections of the photodiode indicates the position of the laser allowing the cantilever to be detected and recorded. The four elements combine to form a signal sum, SUM=(A+B+C+D). Vertical deflection also known as normal deflection is obtained from the difference between the two top segments and the two-bottom segments, N=(A+B-C-D)/sum. This signal is used for contact mode imaging. For tapping mode, the differential

signal is transfer to the RMS converter. Whereas lateral deflection or measurement of torsion in the cantilever is from the difference between the two left and the two right of the segment by L=(A+C-B-D)/Sum [SPM training book; Torre et al., 2011]. This is the most reliable way of measuring the tip-to-sample force of interaction, and easy to use [Miyahara et al., 2002]. The main advantage of the optical lever is that it magnifies the highly sensitive small movements of the cantilever. The cantilever deflections are due to different forces acting between the tip and sample.

9.8 Tip-sample force

Atomic force microscopy principle is based on the force interaction between the tip and the sample. These forces are detected by the AFM electronics to produce useful information about the sample surface. Therefore, it is crucial to understand the forces at play during AFM imaging. The forces have been explained in books and literatures [Morris et al., 1999; Torre et al., 2011]. The forces encounter in AFM imaging include: Van der Waals, capillary and adhesion forces. The Van der Waals force felt by the atom at the apex of tip and the atom of the sample is typically explained with the Lenard-Jones potential curve (Fig 9.2). The critical force regime at which the AFM tip operates includes, the short-range repulsive force region and long-range attractive force, depending on the tip-to-sample distance that is maintained (Fig 9.2) [Morris et al., 1999].

The long-range attractive force regions are where the non-contact mode is operative (Fig 9.2). In this region, there is a small attractive force pulling the tip closer to the sample surface as the tip-to-sample distance is reduced.

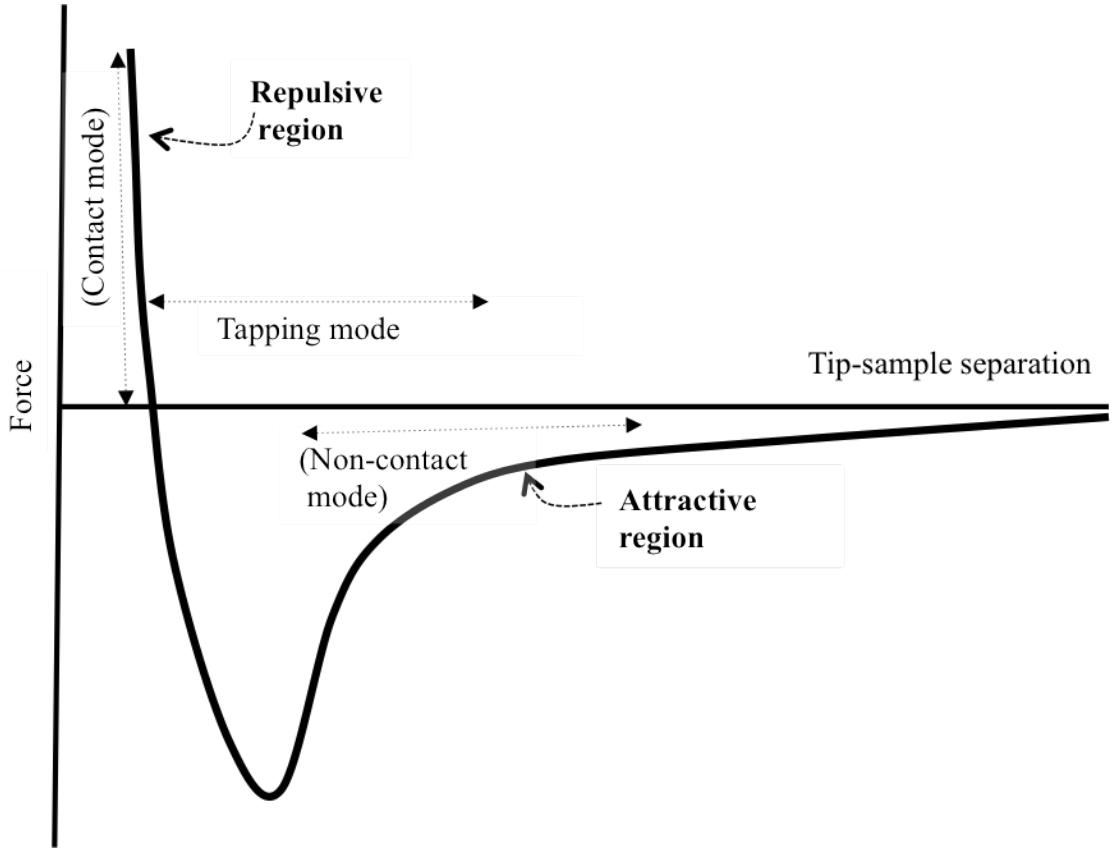

Figure 9.2: Typical "Lenard-jones potential curve" illustrating the force of interaction between tip and sample, and the region where the different imaging modes are operative. Adapted from [Torre et al., 2011].

At the short-range repulsive force region, the electrostatic force acting on the tip and sample at the very small separation distance cause tip deflection. This occurs when the outer shell electrons of atoms at the apex of the tip and the atoms at the sample surface are closely interacting, the force become repulsive, pulling the atoms apart. This is the region where contact mode is operative [Morris et al., 199; Torre et al., 2011].

The tapping mode is operative between the two force regions when the tip oscillates. The deflection of the tip relative to the sample can be affected by the presence of both capillary and adhesion forces. A capillary force is an attractive force applied

from the existence of the meniscus of water between the tip and sample surface. This force pulls the tip towards the surface and can sometimes cause damage to soft samples. The capillary force is not in play when imaging in liquid. Finally adhesion force is the interaction between the tip and sample surface due to a contaminant, and this is usually overcome by changing of the tip [Morris et al., 1999; Torre et al., 2011].

9.9 Imaging Modes

The modern AFM allows different imaging modes and experiment to be carried out. Figure 9.3 presents the diagram of the four different modes of AFM to be described. The three common topographical modes are contact mode, tapping mode and non-contact modes. Other non-topographical modes of experiments are available which allow for measurement of mechanical, magnetic electrical and thermal properties of sample. The last and widely used mode is the force spectroscopy mode, which allows AFM to measure directly the force interaction between single molecules.

9.9.1 Contact mode

Contact mode AFM provides the topographical image of the sample by measuring the deflection of the cantilever. In contact mode, also called the constant force mode, the probe is directly in contact with the sample surface, (Fig 9.3a) and undergoes deflection [Morris et al., 1999]. The applied force, leading to cantilever deflection is kept constant during the scan by the feedback loop. Recording of the peizo-scanner vertical position required to keep the force constant thereby creates images.

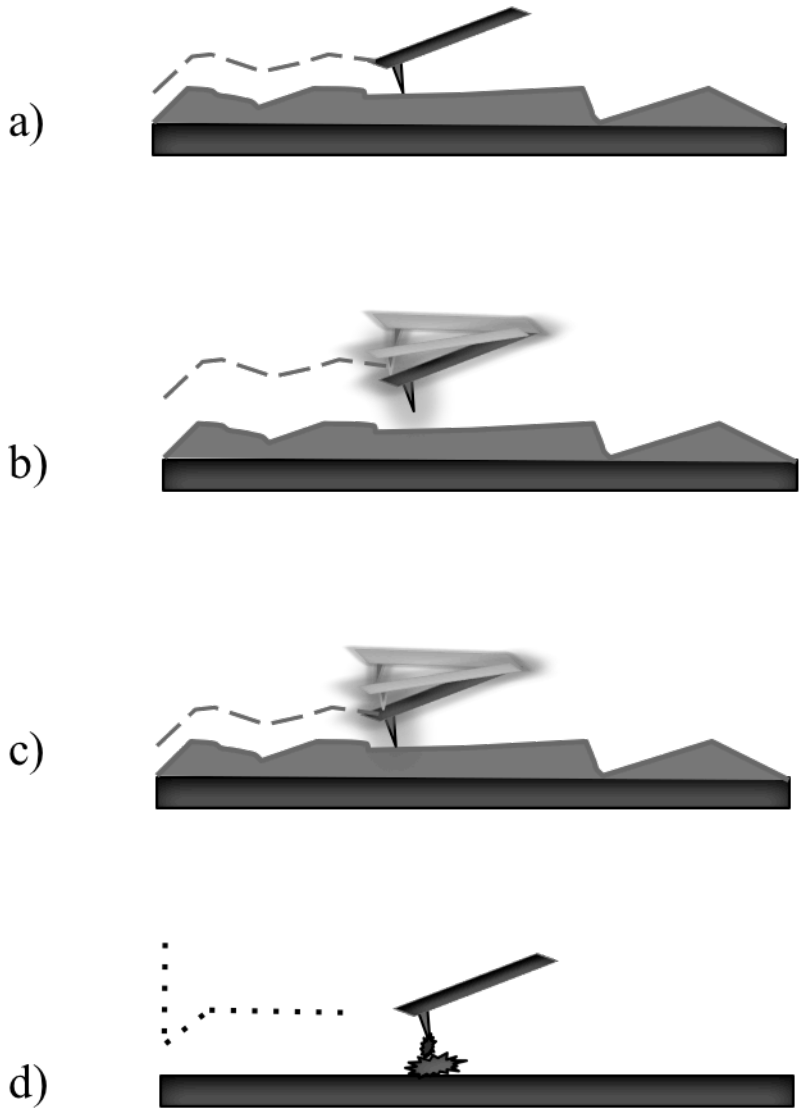

Figure 9.3: Schematic diagrams of the different imaging modes accessible in AFM, a) contact mode, b) non-contact mode, c) tapping mode, d) force spectroscopy mode. Adapted from [Tessmer et al., 2013].

Contact mode is highly suitable for imaging of flat and hard samples. However, since the tip is in contact with the sample, damage to soft samples due to strong lateral force can occur. This can be counteracted by use of very soft cantilever with extremely low spring constant. This kind of cantilever is applicable for contact mode imaging in liquid for biological samples. Imaging in liquid also reduces the capillary force that is present with imaging in air [Torre et al., 2011]. In contact mode, more information can be obtained about the sample surface in error mode, which is created from the signal difference between the deflection set point and the actual deflection of the cantilever from the feedback loop response. Also, torsional distortion of the cantilever due to the lateral force can provide useful information on the different friction and adhesion properties of the sample surface [Alessandrini and Facci, 2005].

9.9.2 Non-contact mode

In non-contact mode, the cantilever oscillates above the sample surface at a certain distance, (Fig 9.3b), and attractive Van der Waals force acting between the tip and the sample can be detected. Recording the cantilever amplitude at a fixed cantilever frequency that is kept constant through the feedback loop creates the images. Imaging in non-contact mode is difficult due to the presence of a thin layer of water at the tip-surface interface, which can trap the oscillating cantilever or create a distance further than the attractive force of interest. Non-contact mode cannot be performed in liquid; nonetheless, it has been used in visualization of biomolecules [Yang et al., 2007]

9.9.3 Tapping mode

In tapping mode, also known as the intermittent contact mode, the cantilever makes intermittent contact with the surface (Fig 9.3c). The cantilever is oscillated near its resonance frequency and the oscillation amplitude is monitored. Oscillation of the cantilever can be controlled either acoustically by piezo-actuator or magnetically by a magnetically susceptible thin film on the back of the cantilever [Revenko and Proksch, 2000]. When the cantilever is in contact with the surface, the oscillation amplitude is damped by the repulsive force, therefore the feedback loop keeps the amplitude constant, and by recording the signal the topography of the surface can be obtained [Morris et al., 1999]. In tapping mode, the tip encounters both the attractive and repulsive force. Phase images obtained from the phase lag cantilever oscillation relative to the signal sent to the piezo driver can provide information on different interaction regions and viscoelastic properties of the sample [Magnov et al., 1997]. Tapping mode is used for imaging of soft biomolecules, because of the less applied force. The advantage of tapping mode is that lateral force is eliminated leading the better lateral resolution [Tamayo and Garcia, 1996]. It can also be performed in liquid [Moller et al. 1999; Melcher et al. 2013]. Tapping mode is the most widely used mode for imaging of biological samples, and it is the mode used in this thesis.

9.9.4 Force spectroscopy mode

In addition to being used for imaging, atomic force microscopy can also be used for quantifying the interaction between the tip and a specific spot on a sample surface. This is the typical force spectroscopy mode, which makes use of the force detection

sensitivity of AFM [Carvalho and Santos, 2012]. This mode involves the cantilever-tip that is moved down toward the area of interest on the sample, (Fig 9.3d). The vertical tip deflection due to the force of interaction is then recorded. The force curve is a measurement of the cantilever deflection as a function of the piezoelectric scanner z-axis position, as seen in Figure 9.4. When the separation distance between the tip and the sample is large, the cantilever feels no force of interaction and no deflection. As the stage extends and brings the tip closer to the surface, long and short-range attractive interaction force is felt, causing the cantilever to deform towards the surface (Fig 9.4). The interaction force causes the tip to jump into contact with the sample region. At very small separation distance, repulsive forces felt by the tip leads to the stage retracting and pulls the tip away from the sample [Torre et al., 2011]. The force curve is then converted into a force-distance curve; the distance corresponds to tip deflection distance and piezo scanner position together. The cantilever deflections are converted into force by applying Hooks law of elasticity, equation 9.1:

$$F = -k \text{ X } d \tag{9.1}$$

Where F is equal to force in (N), k is the probe spring constant (N/m) and d the deflection distance (m). The spring constant of the cantilever-tip assemble provided by the manufacturer are of a wide range, therefore determination of the cantilever-tip force constant is essential. Different approaches for this have been established [Butt et al. 2005, Zlatanova et al., 2000; Carvalho and Santos, 2012]. For biological applications, the AFM tips are usually functionalized with specific chemical groups, which can allow assessing of the different forces between the molecule of the tip and that of the sample surface

[Zlatanova et al., 2000]. Quantitative interpretation of the force spectroscopy data requires use of developed force theories.

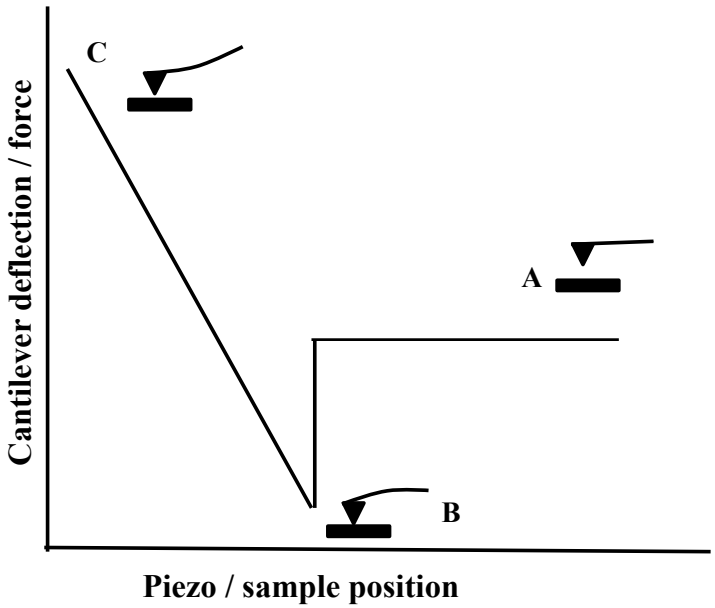

Figure 9.4 Typical force curves illustrating the cantilever deflection portions of moving stage when it extends closer to the surface (A), when the probe jumps in contact with the surface, causing a deformation of the probe (B) and when it retracts the tip away from the sample, and the probe deflects due to repulsive force (C). Adapted from [Tessmer et al. 2013].

9.10 Spatial resolution & Artifacts

Spatial resolution in AFM imaging is related to different factors affecting the image, such as the radius of curvature of the tip, the type of sample being imaged and forces encounter by the tip. Concerning sample types, hard and flat sample surface can be

image easily with higher spatial resolution. The tip plays an important role in AFM image resolution, whereby the image results as the convolution between the samples and tip shape. The choice of optimal tip will be the one with the radius of curvature smaller than the object being imaged. Commercially available silicon tips have radius of curvature of <10nm, as the one used in this thesis, therefore when imaging sample of smaller size, i.e., proteins, DNA an effect called tip broadening (Fig 9.5), is encountered. Consequently the measured lateral sizes of the sample, mostly biomolecules, are a few nanometers wider than expected.

The force exerted by the tip on the sample affects the vertical height information of the object being imaged. Usually the measured height is less than expected. Especially for imaging of soft biomolecules, i.e. DNA, proteins, and RNA, deformation due to applied pressure could lead to the under estimation of the measured height information [Alessanrini and Facci, 2005]. Other tip related artifacts include double tip effect, due to tip damage or contamination and flattening of pits and holes due to the tip geometry whereby the tip does not reach the bottom of the pit [Canale et al., 2011; Morris et al., 1999; SPM training book]. The environment at which the AFM is operated does affect the imaging and the resolution. Therefore it requires a stable environment for optimum results. The mechanical vibrations and acoustic noise from the building can cause image artifacts that are more pronounced when imaging flat samples. As well thermal drift from external temperature can affect imaging. External temperature can be controlled in some AFM with temperature controls [Canale et al., 2011]. The AFM used in this thesis was in an isolation box to reduce the external noise, and a floating/vibrating box to reduce drifting.

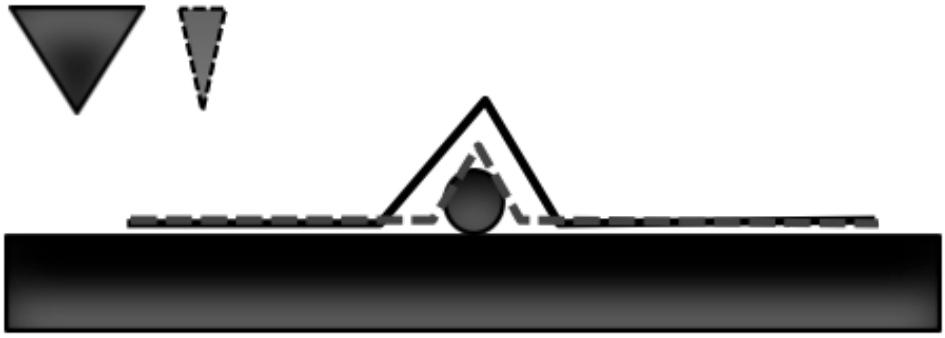

Figure 9.5 Profile illustrating AFM tip broadening effect. The image shows effect of two tips with different radius on sample imaging. Adapted from [Torre et al., 2011].

Scanner sensitivity deteriorates with time; as well it is affected by how frequently the instrument is used. Scanner artifact nonlinearity can be observed as a non-uniform image of a uniform structure. Another artifact is called the hysteresis effect that can be visible in the difference between height traces recorded while scanning from the left to the right and from the right to the left. Lastly an effect called creep and bowing of the scanner can also be observed in images, however this can be removed from the software during image processing. Scanner artifacts occur mainly because the scanner material does not respond linearly to an applied voltage. Scanner artifacts are more pronounced for prolong scanning and large scan sizes, whereas, they are often negligible for small scan sizes. To reduce scanner artifacts and to enable quantitative analysis of sample morphology with AFM, the scanner has to be calibrated from time to time [Canale et al.

2011; Morris et al., 1999 and SPM training book]. In this thesis we used the software method to calibrate the scanner. This involves three steps: 1) imaging of the calibration grid with known dimension and uniform steps, so to detect the non-linearization artifact of the scanner; 2) adjusting the x, y and z parameters of the scanner and reimage the same grid to check that the non-linearization effect is removed; and 3) uploading of the new parameters to the software to be used for imaging. The calibration grid used is a silicon substrate with regular series of pits, each 200 nm in depth and spaced apart by 10 μm by 10 μm.

In addition to all the above-mentioned artifacts, the image resolution can be affected by the feedback loop and scanning parameters settings. Different parameters have to be adjusted each time to obtain the best image. For example in contact mode, the deflection set point; and for tapping mode, the oscillation amplitude and the feedback gains have to be adjusted each time. The general rule used is to set the gain parameters as high as possible until there is a presence of the periodic noise artifact. Then the parameters can be reduced until the tip is tracking the surface successfully without noise. Adjusting the scan rate and the number of lines per image can also affect the resolution of the images. In this dissertation, tapping mode images of biomolecules were obtained with a scan rate of 1-2 Hz, scan sizes from 500 nm^2 – 3 μm and 512 lines per images. In tapping mode, the amplitude set point can be lowered to increase the drive frequency to push the tip to track the surface without interruption. This usually led to better lateral resolution; however it can affects the height information. This is because by increasing the drive frequency we are increasing the force that is applied thereby increasing the applied pressure on the soft biomolecules.

9.11 Image processing

Tapping mode AFM was performed with a Dimension 3100 microscope and Nanoscope IIIa controller (Digital Instrument Inc., Vecco). Tapping mode AFM images recorded in air were obtained using silicon probes with a resonance frequency of 200-300 kHz (vista probe). The images were captured at a scan rate of 1-2 Hz and with a 512x512 pixels resolution. Image height scale is typically of the order of 3 nm, exact values are provided for each image. Images were subjected to a third order flattening to remove image-bowing artifact using the microscope's software (Nanoscope, V613r1).

Volume analysis of samples from AFM images was performed using NIH software image SXM. The software fits the sample shape to an ellipse and provides quantification of sample properties, such as their individual height, projected area and the minor and major axes. The background is subtracted by first generating a histogram to obtain the average surface height (S), which can then be subtracted from the measured particle mean height (M_i) to get the correct average mean height (H_i). The volume of each particle from AFM images (V_i) is calculated by multiplying the area of the particle, A_i, by the corrected average mean height of the particle H_i, using the equation given below.

$$V_i = A_i(M_i - S) = A_i \times H_i \qquad (9.2)$$

Detailed description of this volume analysis is provided in my Master's thesis [Ore, 2010]. The first step is to determine the surface height of freshly cleaved mica by using the histogram function under analyze menu in the software. Next we identified the proteins and measured properties such as area, and mean height of the proteins. Ratcliff and Erie have demonstrated that the volume of 7 different proteins as measured from

AFM images depends linearly on their molecular weight [Ratcliff and Erie 2001]. Consequently, dimerization constant of DNA helicase UvrD, was determined from that volume analysis [Klinov et al., 2009.]. The linear relationship between AFM volume analysis and molecular weight is described by equation 3.3 below [Yang et al, 2003];

$$V = 1.2(MW) - 14.7 \qquad (9.3)$$

Following Eq. 9.3 where V is the volume measured using AFM and MW is the molecular weight of the protein, we can calculate the expected volume for monomeric VraR, with MW= 23430±0.2 Da [Belcheva et al., 2009]. Therefore, using Eq. 9.3, the calculated volume for a VraR monomer is 13.4±0.2 nm^3. In this work, all histogram graphs were plotted using sigma plot software. The histograms were fitted with nonlinear regression of either Lorentzian or modified Gaussian distribution to obtain the mean (x value at maximum height) and standard deviation (full width at half maximum height).

Chapter Ten

VraR –DNA *vraSRp* Complex AFM Results and Discussion

10.1 AFM imaging of *vraSRp* DNA and VraR-P protein

Investigation of pathogens at the molecular level can provide new insight and understanding of their mode of action. AFM allows direct visualization of the biomolecules as shown in Figure 10.1a for a typical tapping mode AFM image of *vraSRp* DNA strands deposited on mica. The *vraSRp* is a 612bp DNA and the sample was deposited at a 2 nM concentration using a deposition buffer containing Mg^{2+}. The deposition buffer allowed effective adsorption of the DNA molecules onto the mica surface. A representative tapping mode AFM image of phosphorylated VraR protein deposited on mica (from a 20 nM solution) is shown in Figure 10.1b. The proteins are visible as globular or spherical shapes in the image. Both the DNA and protein molecules can be distinguished from each other due to their different shapes and sizes. AFM investigation of proteins and DNA are well published [Schneider et al., 1998; Yang et al., 2003; Schlacher et al., 2005] and supports the approached use in this work.

The DNA strands in the AFM image (see Fig 10.1a) are visualized as featureless long polymers without their helical structure of the DNA being visible. This is due to the type of tip and the AFM model used for the experiment. The silicon tip utilized has a radius of curvature ca. <10 nm, which is larger than the pitch and diameter of the DNA double helix of ca. 3 nm and ca. 2 nm, respectively.

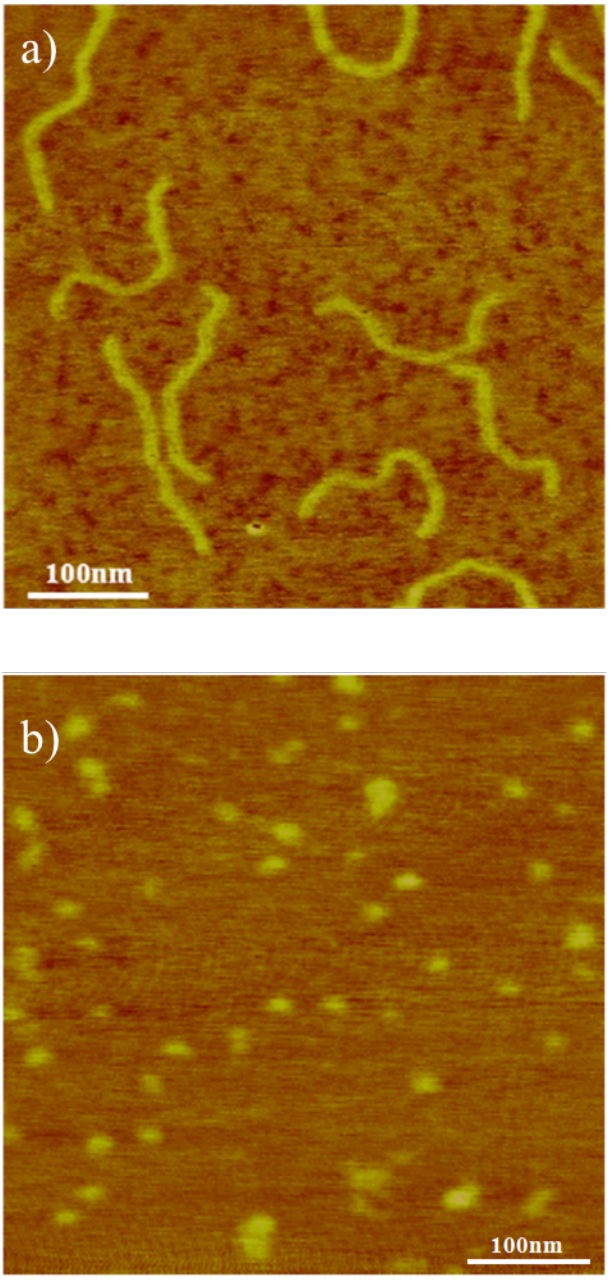

Figure 10.1: Representative tapping mode AFM image of a) DNA *vraSRp* 2 nM *b)* 20 nM VraR phosphorylated. The volume deposited on mica was 20 µL and the molecules were left to interact with the mica surface for 1 min before the surface was rinsed with double distilled water, and dried with argon gas.

However recent advances in AFM technologies have led to the development of new AFM models together with the availability of ultra-sharp tips have made it possible to image DNA with resolved helical feature, i.e., the minor and major grooves [Leung et al., 2012; Ido et al., 2013; Pyne et al., 2014]. In addition, AFM has been used for the investigation of both soluble and membrane bound proteins [Alessandrini and Facci, 2005]. For example, membrane proteins that are packed in a 2D crystalline array have been imaged with high-resolution and a detailed conformational structure of Aquaporin Z protein was obtained [Horber and Miles, 2003]. Moreover, AFM has been used not only for imaging of protein but also for quantitative analysis of association constant between proteins, [Ratcliff and Erie, 2001], interaction between proteins [Funetes-Perez et al., 2013; Schlacher et al., 2005] and stoichiometry of protein bound to DNA [Wyman et al., 1997].

10.2 AFM result of VraR-*vraSRp* complexes

Proteins are important biomolecules, as they regulate large number of biological processes. For gene regulation, the protein must interact with DNA by recognition of specific sites at the promoter region on the DNA. Biochemistry analysis using DNase I footprinting of VraR binding to *vraSRp* complex was performed by Belcheva et al. and three important binding sites, namely R1, R2 and R3, were identified. VraR was found to bind with greater affinity to site R1, whereas it was found to only bind to R2, and R3 upon phosphorylation. AFM was employed to visualize the protein binding on the DNA, the extent of binding of the protein and where the protein is bound.

Figure 10.2 shows tapping mode AFM images of VraR-*vraSRp* complexes formed on a mica surface, and of complexes formed in solution prior to their deposition on mica. When VraR protein is introduced to the DNA sample either free in solution or pre-adsorbed onto a mica surface, VraR can be specifically or non-specifically bound to the DNA, remain free in solution or bind to the mica surface. All of these states are apparent in the AFM images shown in Figure 10.2. From these images, the interaction site of VraR on *vraSRp* is mapped using the circular bump on *vraSRp* with the significant height difference shown using black arrows as corresponding to the protein-DNA complex of interest. The red arrows points to non-specific interactions, while the white arrow points to freely adsorbed DNA and VraR protein (Fig 10.2). Atomic force microscopy has been used previously for the investigation of other protein-DNA complexes [Erie et al., 1994; Harada et al., 2001]. Lushinkov et al. make use of AFM for the visualization of restriction enzyme protein SFiI, which binds to site specific region of DNA, but required binding to two DNA for stability [Lushinkov et al., 2004]. Contact mode has also been used for imaging of protein-DNA complexes, of mutated *EcoRI* endonuclease, which binds with high affinity to a specific site on a plasmid DNA [Alison et al., 1996].

In this work, VraR was able to recognize, access and bind to the specific recognition site on the DNA bound to mica. As it was demonstrated, the use of a low concentration of divalent cation does not hinder the accessibility of the protein to DNA bound to mica [Pastre et al., 2009]. Figure 10.3, shows representative AFM images of the complex formation of phosphorylated VraR with the DNA fragment *vraSRp*. Also visible in the images are VraR proteins that are specific and non-specific bound to DNA as well as freely adsorbed onto mica.

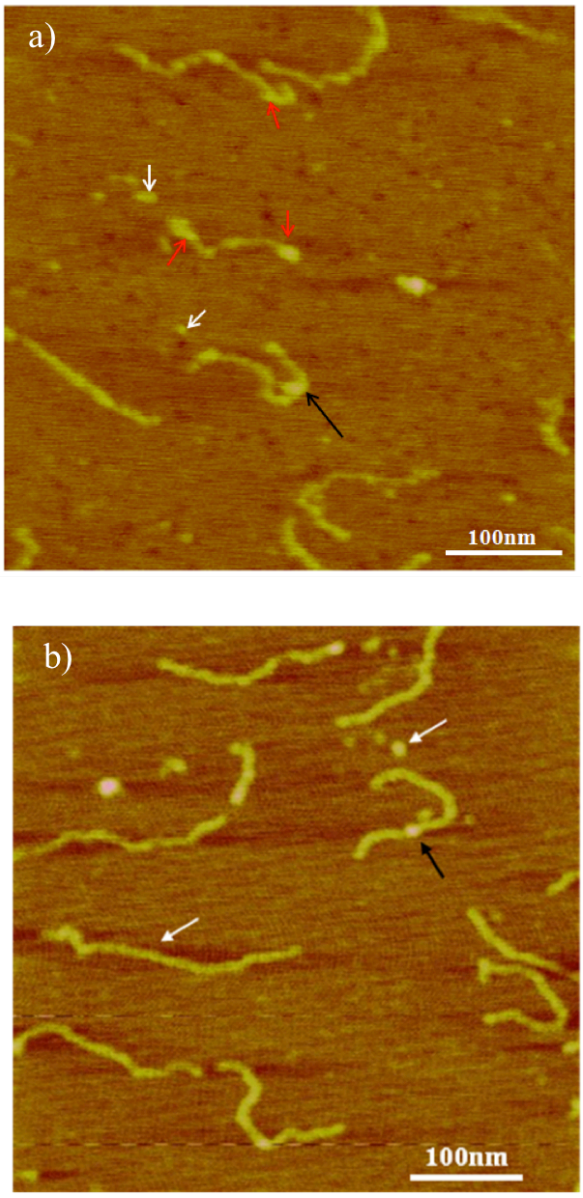

Figure 10.2: Representative tapping mode AFM image of **(A)** VraR-*vraSRp* complex formed on mica surface following protocol I**.** The black arrow shows specific complexes, the red arrow represents non-specific interaction between the proteins and the DNA molecules and the white arrow shows adsorbed VraR proteins on mica **(B)** VraR-*vraSRp* complex formed in solution and deposited on mica following protocol II. The black arrow shows site-specific interaction of VraR and *vraSRp.*

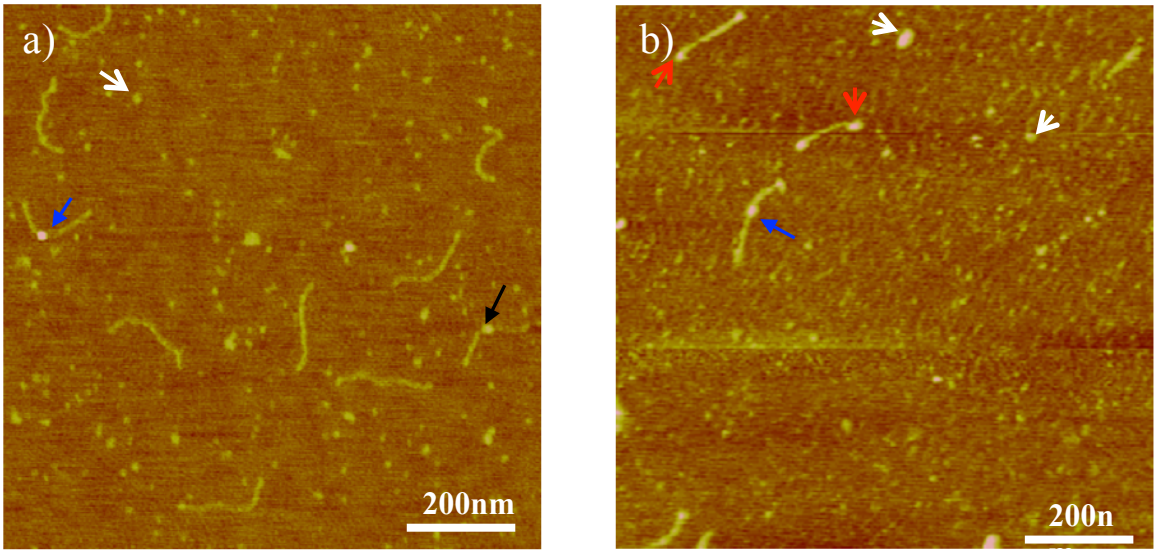

Figure 10.3: Representative tapping mode AFM images of **(A)** phosphorylated VraR-*vraSRp* complex formed on mica surface following protocol I **(B)** phosphorylated VraR-*vraSRp* complex formed in solution and deposited on mica following protocol II. The black arrow shows site-specific interaction of VraR-P- *vraSRp* promoter complex similar to observed previously, whereas the blue arrow points to VraR-P-*vraSRp* promoter complex with larger height. The red arrow represents non-specific interaction between the proteins and the DNA molecules and the white arrow shows freely adsorbed VraR proteins.

Two distinct specific VraR-*vraSRp* complexes are visualized in the images in Figure 10.3; one particular complex is similar to the complexes previously observed with dephosphorylated VraR with similar height. Interestingly, the second complex, blue arrow adopts a new conformation with much greater height. Binding of phosphorylated VraR leads to *vraSRp* DNA bending as seen in Figure 10.4. Interaction of the protein has been known to initiate conformational changes on DNA upon binding such as: bending, wrapping and DNA looping. [Rivetti et al., 1999; Wyman et al., 1997]. Also DNA gyrase was visualized by AFM to cause DNA wrapping in the presence of the nucleotide: whereas lose of DNA wrapping was observed in absence of nucleotides [Heddle et al., 2004]. Also reported was the visualization of ECoKI type 1 DNA restriction enzyme protein causing dimerization and DNA looping [Neaves et al., 2009]. AFM imaging in liquid has been used for protein-DNA binding for protein activity. AFM imaging in tapping mode has visualized *Escherichia coli* RNA polymerase (RNAP) activity with two different linear DNA molecules [Kasas et al., 1997].

10.3 Volume analysis of VraR protein

AFM volume analysis can provide information on stoichiometry of protein deposited on the surface, in protein-protein and protein-DNA interactions. Volume analysis can be performed either by geometric method or by direct method. The geometric method involves manual measurement of the lateral and vertical parameters of the molecule (height and width) and these parameters are then fitted to a volume equation of a predicted molecule shape, i.e., spherical, ellipsoid [Edstrom et al., 1990; Schneider et al., 1995].

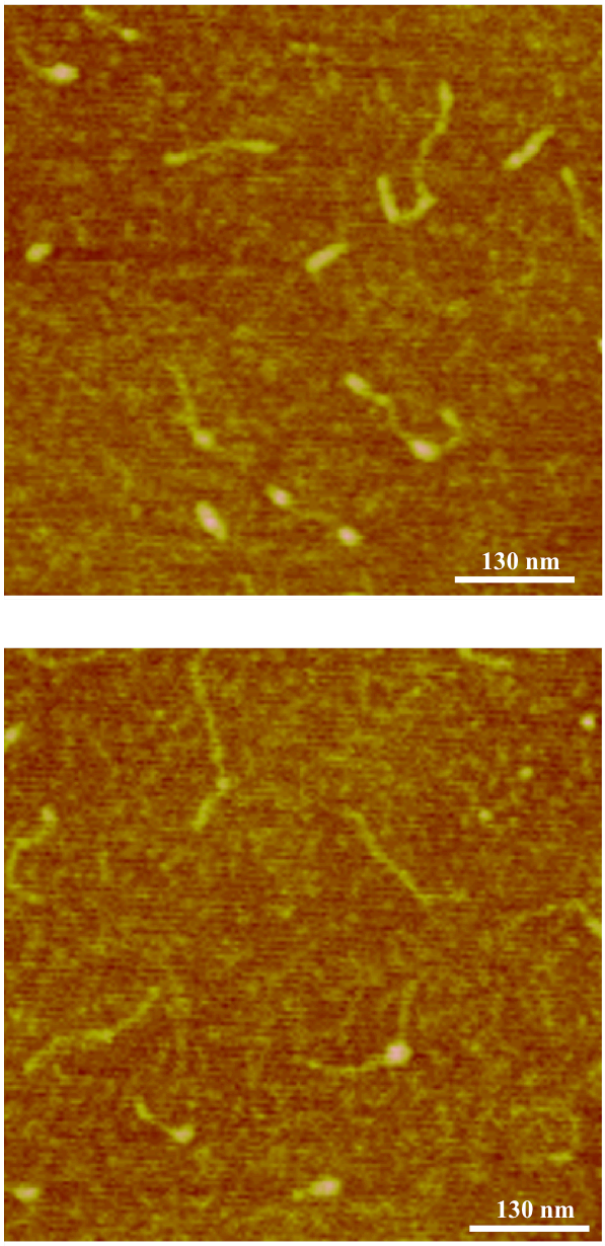

Figure 10.4: Representative tapping mode AFM images (a and b) of phosphorylated VraR-*vraSRp* complex formed on mica surface following protocol I.

The direct method, which was used in this thesis, calculates the volume by considering every pixel within a region of interest, this involve calculating the area of the slice above a height threshold and then multiply this by the average height [Wyman et al., 1997; Ratcliff and Erie, 2001; Beerens et al., 2005]. While both methods are widely used, the direct method can be applied to any molecule type or shape, which is why we decided to make use of it. In Figure 10.5 is the histogram of the VraR and VraR-P volume measured from the AFM images using the direct method following equation 9.2. The histogram of VraR volume (Fig 10.5a) shows a high distribution of VraR on the surface at a maximum of 13 ± 4 nm^3 for the nonlinear regression curve. The volume obtained from our AFM images is in close conformity with the theoretical calculated volume of 13.4 ± 0.2 nm^3 for a VraR monomer.

The theoretical volume was calculated following Equation 9.3 in chapter three knowing that the molecular weight of VraR tis equal to 23430 ± 0.2 Da. Equation 9.3 is the linear correlation of the molecular volume of different proteins obtained from AFM images as a function of their molecular weight as determined by Yang et al. [Yang et al., 2003]. The AFM volume of VraR was calculated using the same direct method as used by Yang et al. Therefore it is ideal to compare our data using this equation rather than other mathematical equation used for volume estimation with assumption such as the spherical shape of protein [Edstrom et al., 1990; Neish et al., 2002]. The high distribution of VraR is significantly close to the calculated AFM volume of monomer VraR of 13.4 ± 0.2 nm^3 indicating that VraR adsorbs on mica surface mainly as a monomer with few dimers and oligomers.

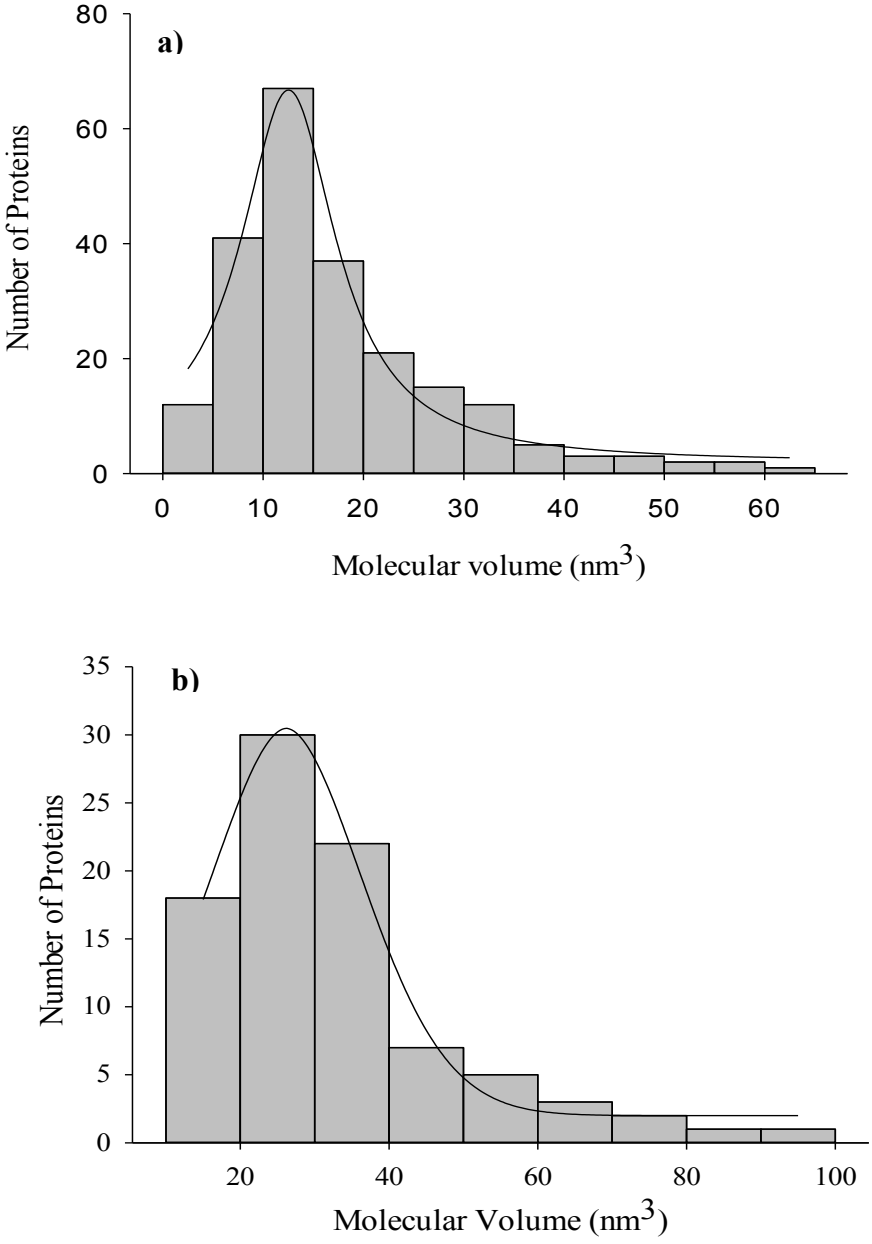

Figure 10.5: Histogram distribution of measured AFM volume of **(a)** VraR proteins deposited on mica from a 20 nM solution (20 µL were deposited); and (**b)** VraR phosphorylated proteins deposited on mica from a 20 nM solution (20 µL were deposited).

These results are consistent with the findings that VraR in solution exists as a monomer as determined from HPLC and MALDI MS measurements [Belcheva et al., 2009]. Similar analysis for the phosphorylated VraR protein revealed a mixture of monomer, dimer and oligomer occurring as shown in the histogram in Figure 10.5b. For the phosphorylated protein, the distribution peaks at a maximum of 26 ± 10 nm^3. This result clearly indicates that for VraR phosphorylated dimers are the dominant species on mica. This result is consistent with phosphorylated VraR existing mainly as a dimer in solution [Belcheva et al., 2009]. Volume analysis of proteins from AFM images has been used to compare protein sizes and obtain beneficial information. The method described by Ratcliff and Erie was used in this dissertation to obtain the experimental volume of VraR from the AFM images.

10.4 Volume analysis of VraR-vraSRp DNA complexes

The stoichiometry of VraR at the binding site of the VraR-*vraSRp* complexes, can be determine using the same volume analysis as described by Ratcliff and Erie. To understand the gene regulation mechanism utilized by VraR, we obtained the stoichiometry of VraR at the binding site *vraSRp.* The volume analysis was carried out using the software Image SXM. The software provides us with the means to measure properties of the complex such as mean height and area. First, we select the complex using the density slice function from the software and exclude all other background DNA fragments and proteins on the surface. Therefore the program, in this case, provides only measurements of one particular area, which is the complex. As well the program can measure the mean height of the background DNA which has no VraR bound to it using the density slice option to exclude the complex. Once all the required parameters (height

of the complex and DNA and area of the complex) have been measured, the volume of VraR protein at the complex site can be determined to evaluate the stoichiometry of the protein. Histograms of the calculated volumes of the phosphorylated VraR protein-DNA complexes are shown in Figure 10.6 for 25 complexes. Volume analysis of the phosphorylated VraR complexes shows complexes with volume corresponding to increased binding of VraR at the complex site. This was determined by the large volume of VraR at the binding site, from the volume value of 109 ± 2 nm^3 as the maximum of the histogram nonlinear regression curve (Fig 10.6). With phosphorylated VraR, it was discovered that there is an increase in VraR protein bound at the complex site [Belcheva et al., 2009] and this is also observed from our volume analysis where more VraR protein is bound to the DNA.

Similar AFM volume analysis was performed with DNA binding of the STAT3 protein: that is involved in gene regulation in various cancers. It was reported that dephosphorylated U-STAT3 binds as a monomer and dimer to the DNA promoter region-containing gamma activated sequence (GAS). STAT3 protein is consequently phosphorylated in various cancers and drives gene expression from GAS-containing prompter to promote tumor geneses [Timofeeva et al., 2012]. Binding of VraR protein to the most conserved site (R1) is phosphorylation independent, and this was proven by the observed complex formation from our AFM analysis of dephosphorylated VraR binding with *vraSRp* DNA, shown in Figure 10.2.

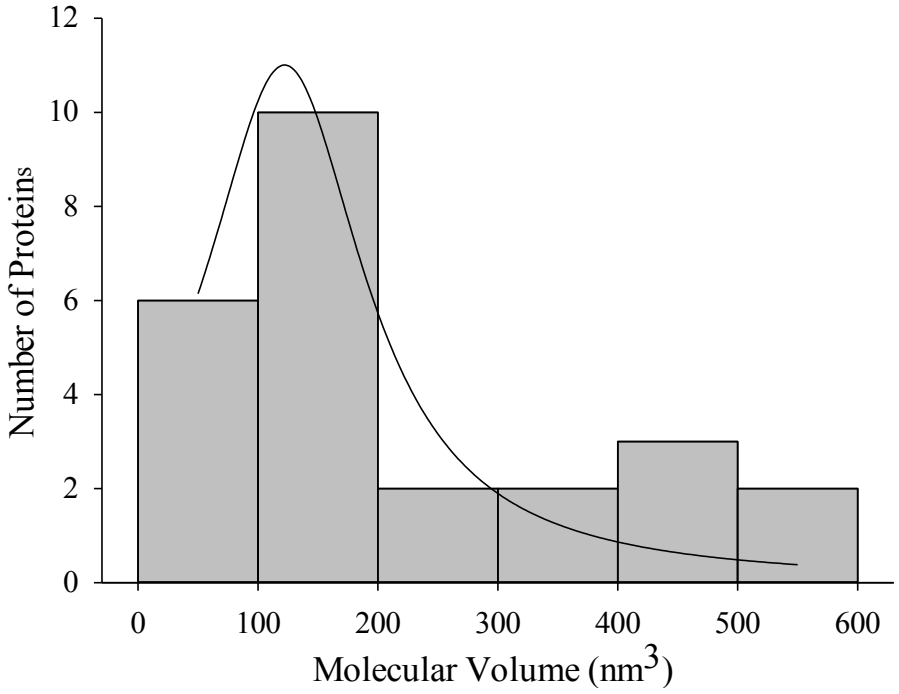

Figure 10.6: Histogram indicating the VraR distribution as a function of volume displaying phosphorylated VraR molecules bound to *vraSRp* promoters as a distribution of oligomers.

Binding of VraR to the less conserved site (R2, R3) requires phosphorylation of VraR, and this was observed by the increase in stoichiometry of VraR protein at complex site upon phosphorylation. Therefore, with the volume analysis, we were able to distinguish the binding capacity of dephosphorylated VraR and of VraR upon phosphorylation. As well we were able to identify conformation changes induced by an increase amount of binding of VraR on the DNA upon phosphorylation (Fig 10.4).

Figure 10.7 is the AFM image of phosphorylated VraR-DNA complexes with a complex bound by VraR as oligomer, which was expected upon phosphorylation. The binding sites on the *vraSRp* promoter DNA are separated by only 10 nucleotides, [Belcheva et al., 2009] therefore resolving the binding of VraR to each site would be unfeasible using the current method. As well this site is proposed to overlap with the binding site of the RNA polymerase complex, suggesting that VraR could be interacting with the transcription machinery in the presence of the cell wall stress signal [Belcheva et al., 2009]. In *S. aureus,* VraR protein is phosphorylated by it cognitive protein kinase VraS, leading to dimerization and binding of VraR to its specific sequence on the *vraSRp* promoter region. This initiates gene regulation in response to cell wall stress, for example the presence of antibiotic vancomycin or beta-lactam that can inhibit cell wall peptidoglycan biosynthesis. In this thesis we provide not only the direct visualization of VraR-DNA complexes (Fig 10.7), but also with the ability of AFM to provide three dimensional information, the stoichiometry and degree of VraR protein bound at the complex site.

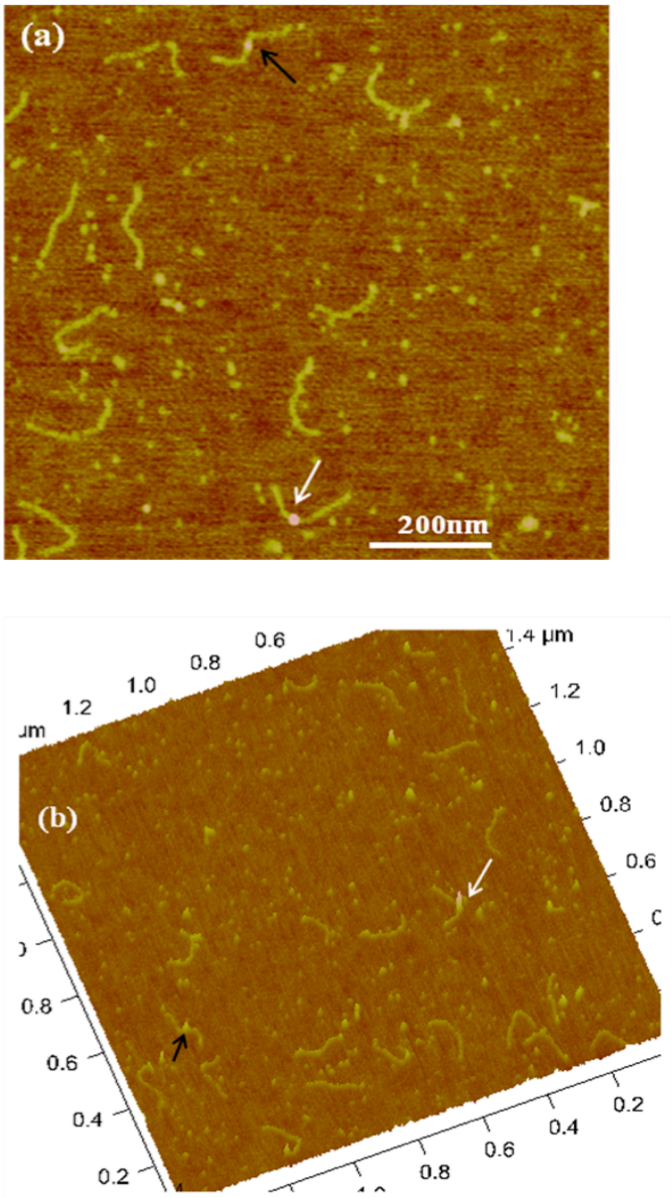

Figure 10.7: Representative tapping mode a) 2 dimensional and b) 3-dimensional AFM images of phosphorylated VraR-*vraSRp* complexes formed on a mica surface following protocol I. The black arrow shows site-specific interactions of VraR and *vraSRp* promoter as tetramers, white arrow shows VraR and *vraSRp* promoter as oligomers.

Chapter Eleven

Tomato Bushy Stunt Viral RNA AFM Results and Discussion

11.1 AFM images of Tomato bushy stunt virus (TBSV) genomic RNA

Secondary and tertiary structures of genomic viral RNA play essential regulatory role during translation, RNA replication and assemble of new viral particles [Davis et al., 2008]. However current methods such as structure prediction programs can only provide predicted structure base on lowest pseudo free energy, accompanied with long tedious experimental procedures. AFM provides us with the ability to directly visualize the structural conformations of genomic RNA. It requires little to no sample preparation, and important structural information can be obtained within minutes. Hence, we used AFM to gain insights into the global organization of the TBSV genome and high-resolution images of individual molecule were obtained (see Fig 11.1). This type of analysis provides information on the overall structure of the RNA molecule adsorbed to a mica surface and has been used successfully to assess global conformations of different viral RNA genomes [Kuznetsov et al., 2005; Davis et al., 2008]. In this thesis, the RNAs was in a Mg^{2+} containing buffer and were deposited onto freshly cleaved mica, dried under argon and imaged by tapping mode AFM in air. Different compact structures were observed for all the individual genome molecules.

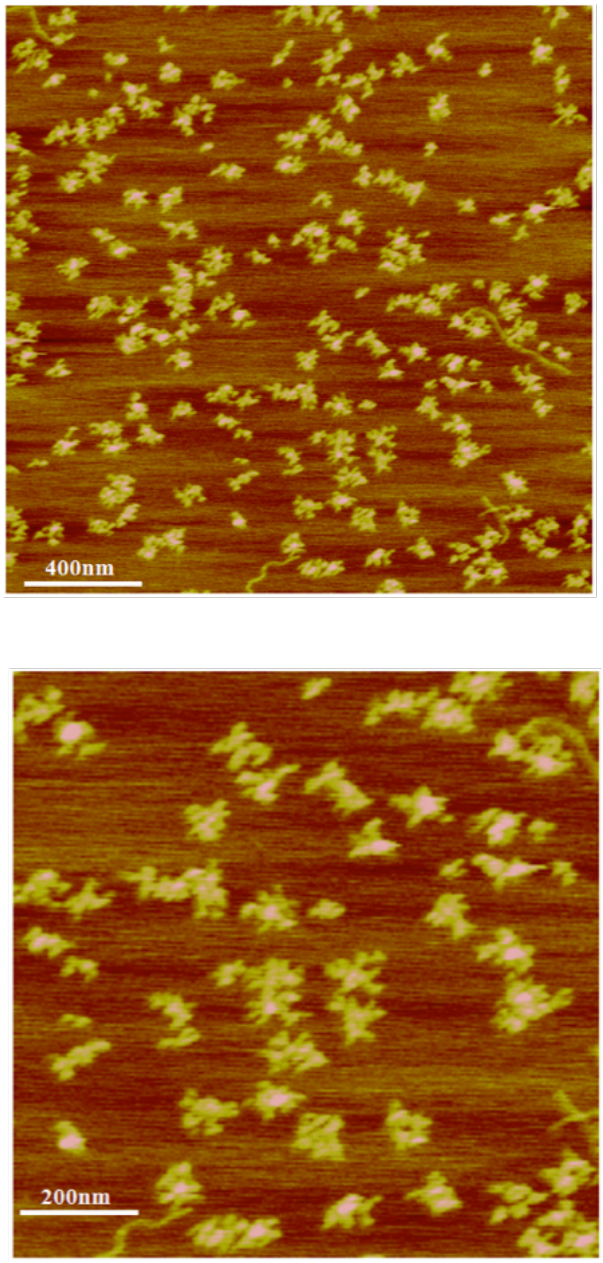

Figure 11.1: Tapping mode AFM images of 1.5 ng/µl TBSV RNA genome deposited on a freshly cleaved mica surface using a deposition buffer containing Mg^{2+}.

This was due to the different surface adsorption and conformation flexibility of the molecules. However, what was evident from the AFM analysis was the general conservation of a global organization consisting of irregular extensions emanating from a central core (Fig 11.1). Some variation from this overall arrangement was evident, but the level of compactness and the presence of multiple domain protrusions were typically maintained. These results suggest that the TBSV genome assumes a mostly condensed structure that is consistent with genome conformations that include multiple long-distance RNA-RNA interactions [Wu et al., 2012]. AFM provided informative analysis when used by Davis et al., for structural comparisons of different mammalian genomic viral RNA. It shows the different structural shape with some adopting a tightly condensed structure and others adopting irregular structure with protruding single stranded RNA [Davis et al., 2008].

AFM analysis of the genomic RNA structure can provide links between the predicted structure and that observed from the physical solution phase structure [Davis et al., 2008]. In this thesis we compared our obtained RNA structure from AFM analysis with that predicted secondary structure from selective 2'-hydroxyl acylation analyzed by primer extension technology (SHAPE). SHAPE is a chemical probing technique that provides quantitative reactivity information for every nucleotide in the RNA molecule. SHAPE can be applied to all sizes of RNA *in vitro* and *in vivo*. To provide accurate secondary structures of the RNA molecules, SHAPE technology must be implemented with a thermodynamic-based dynamic algorithm program [Low and Weeks, 2010]. Our collaborator performed this intricate experimental work using SHAPE technology, which involved: selective modification of the RNA molecules in a structure dependent manner,

followed by detection of the modification site by target labeled primer extensions, coupled with high-throughput capillary electrophoresis with DNA sequencing technique. The output of the electrophoresis is analyzed by a program SHAPE finder, which provides the reactivity values that are converted to pseudo – free energy terms. RNA structure programs use this energy terms to generate an accurate secondary structure of RNA. SHAPE has been used to propose experimentally secondary structure of many RNAs [Diegan et al., 2009; Wilkinson et al., 2008; Low and Weeks, 2010].

The resulted secondary structure from SHAPE analysis of TBSV genomic viral RNA is shown in Figure 11.2b. It is obvious that our observed AFM structure is consistent with the SHAPE guided secondary structure model, (Fig 11.2a&b). The measured diameter of the TBSV genomic RNA from AFM images is 98 ± 12 nm (n = 40). A theoretical maximum ladder distance (MLD) [Yoffe et al., 2008] of 248 bp was calculated for the TBSV genome, which represents the number of base pairs passed when spanning the two furthest points in the optimal structure, predicted by the RNA structure software [Mathews, 2006]. With the average rise per base pair in dsRNA corresponding to, 0.27 nm [Kebbekus et al., 1995], this MLD converts to an average measurement of, 67 nm. The MLD average over 1000 suboptimal secondary structures was calculated as 252bp or, 68 nm [Wu et al., 2013]. The measured diameter (98 ± 12 nm) of the RNA genome from AFM images was not far off from the predicted from of 67 nm. The over estimation of the measure diameter from the AFM images can be due to tip broadening effect.

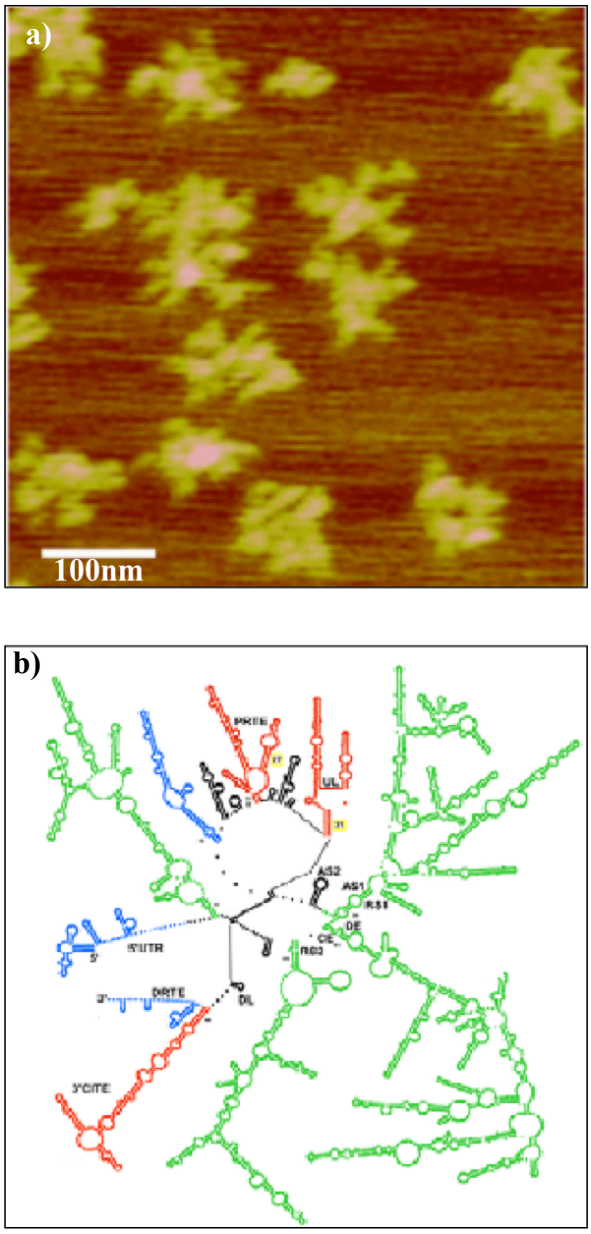

Figure 11.2: Representative tapping mode AFM image of, a) genomic TBSV viral RNA and b) a simplified version of the SHAPE guided TBSV genomic RNA secondary structure. Each dot represents a nucleotide and domains are labeled and color-coded. Adapted from [Wu et al., 2013].

11.2 AFM images of sub-genomic TBSV RNA

Two sub-genomic RNA, labeled (Sg1 mRNA and Sg2 mRNA) are transcribed from the genomic viral RNA of TBSV. In TBSV, the two sub-genomic RNA serve as a template for translation of important viral proteins, crucial for its survival. Within the Sg1, mRNA is the genetic codes of p22 and p19 that is translated to the movement protein and the suppressor of gene silencing [Oster et al., 199; Fabian and White, 2004]. Whereas within the Sg2 mRNA is the p41 codes that is translated to the coat protein [White and Nagy, 2004]. Long-range RNA-RNA interactions involved in regulating Sg mRNA transcription are not restricted to tombusvirus. Other plus-strand viruses also require such intra-genomic interactions for transcription of their Sg mRNAs [Lindenbach et al., 2002; Mateos-Go´mez et al., 2011]. Figure 11.3 is the tapping mode AFM images of Sg1 mRNA. The visualized structure exists as a compact structure with emanating domains/branches, which are evidence of the long range RNA-RNA interaction. Figure 11.4 is the representative tapping mode AFM images of Sg2 mRNA, visualized as a compact structure of one or two emanating branches/ domains. A single well-defined structure for the Sg mRNA molecules was not observed. Rather the different visualized structural features were sorted into categories.

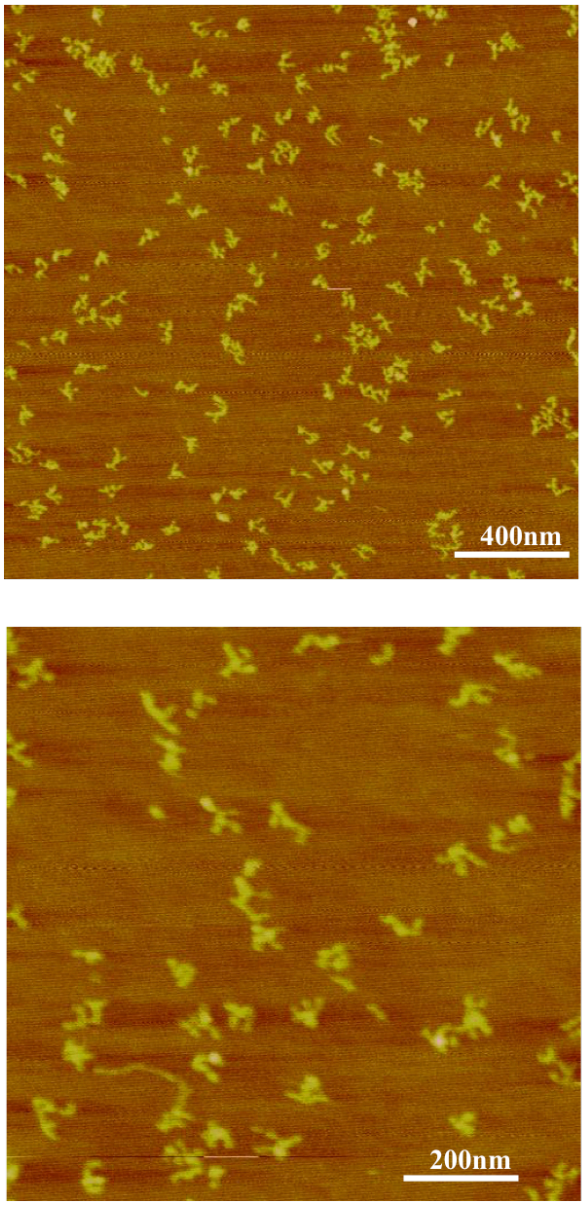

Figure 11.3: Tapping mode AFM images of 1.5 ng/µl TBSV Sg1 mRNA genome obtained on freshly cleaved mica using a deposition buffer containing Mg^{2+}.

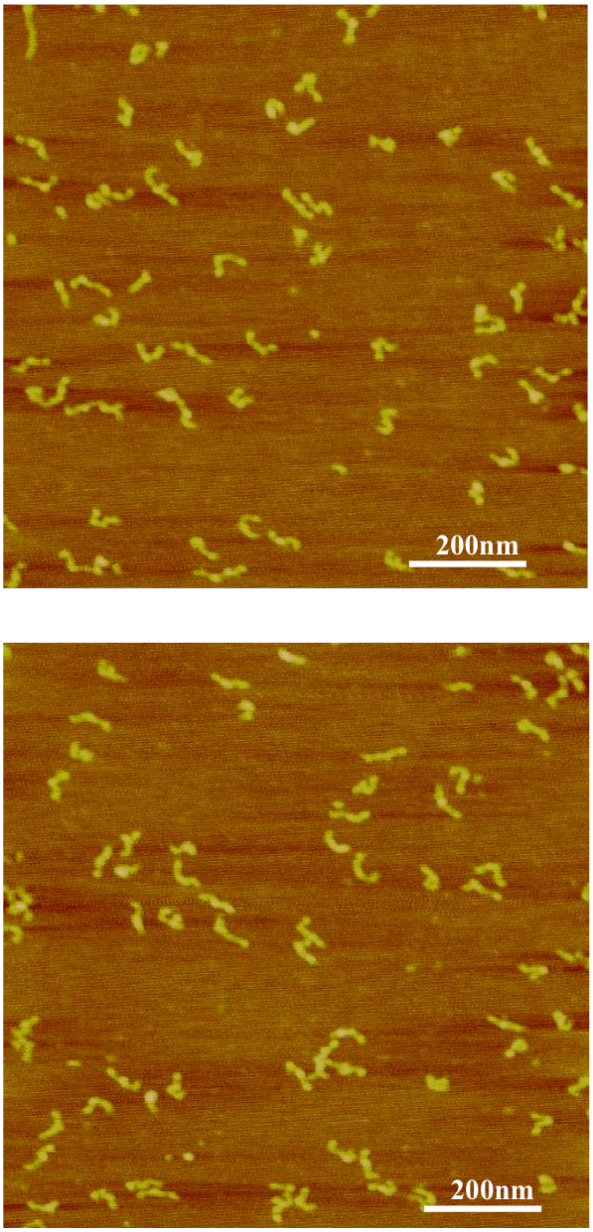

Figure 11.4: Tapping mode AFM images of 1.5 ng/µl TBSV Sg2 mRNA genome obtained on freshly cleaved mica using a deposition buffer containing Mg^{2+}.

The observed structural features of Sg1 mRNA from the AFM image are sorted in to four categories. The relative fraction of each visualized structures are as follows: (n=80), 10 % for one branch, 7.5 % for 2 branch, and 16 % for the four branches. The 3-branch has the highest percentage of 62.5 % and it is the structure that is more consistent with the SHAPE guided structure for the Sg 1 mRNA, (Fig 11.5). While the visualized structural feature for Sg2 mRNA were sorted into two categories. The relative fraction of each visualized structure was calculated as follows, 24% for one branch, and 76 % for 2 branches, (n=50). The two branches were the structure that was more consistent with the SHAPE guided structure for the Sg 1 mRNA, (Fig 11.6). The presence of multiple forms is due to the different deposition orientations of the molecule, as well as the degree at which they spread out onto mica substrate. The use of low concentration Mg^{2+} buffer for adsorption of the RNA molecules, might favour formation of the partially extended conformation because of the affinity of the negatively charged RNA with the partially positive mica. The different structural forms have been reported for other RNA investigated by AFM, i.e., satellite tobacco mosaic virus (STMV) [Archer et al., 2013]. However, it is important to note that the observed conformations with the highest percentages are in conformity with the SHAPE predicted structures for both Sg1 and Sg2 mRNA. This indicates that the majority of RNA molecules adopted there appropriated conformation under our deposition protocol.

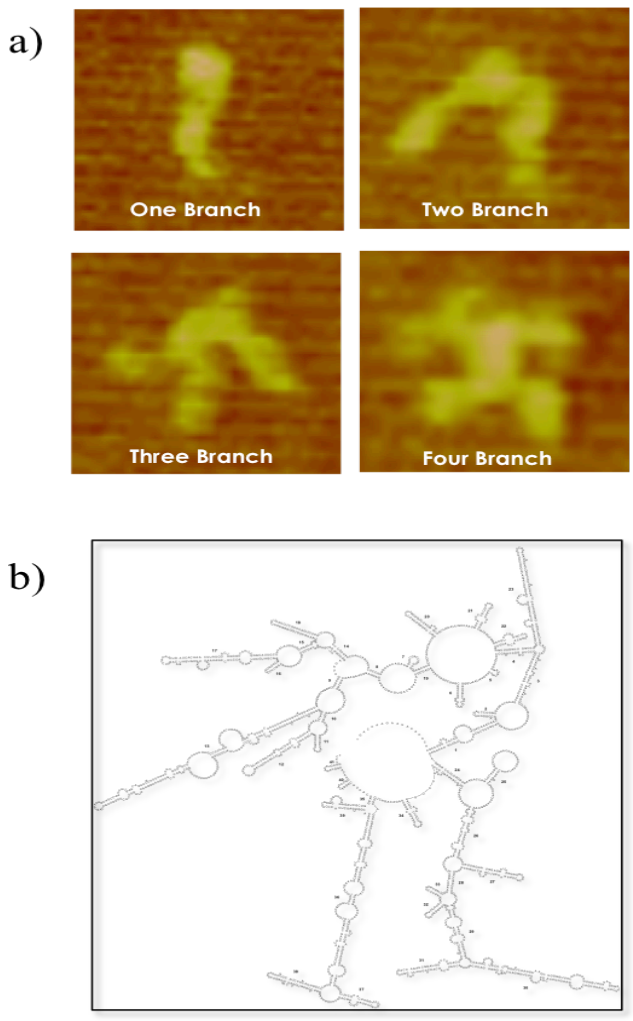

Figure 11.5: Classification by structural features of observed a) Sg1 mRNA from AFM images and b) the SHAPE guide structure.

a)

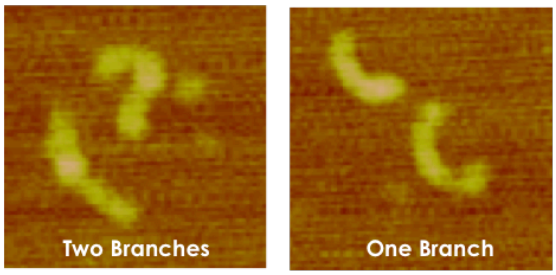

b)

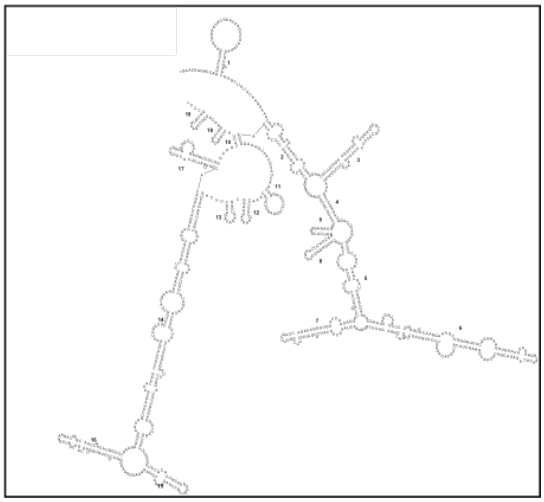

Figure 11.6: Classification by structural features of observed a) Sg2 mRNA from AFM images and b) the SHAPE guide structure.

11.3 Volume Analysis of TBSV viral RNA

The advantage of AFM over other imaging mode is the possibility of preforming quantitative analysis of obtained images to support the observed topography of the molecules. Volume analysis is a common measurement used for investigation of different biomolecules, to determine if the observed structural confirmations are in conformity with the expected results. We also embarked on volume analysis of the observed TBSV viral RNA structure. The volume analysis was performed using Image SXM software,

following the procedure illustrated in the imaging process section in chapter 9 of this thesis. The predicted volume of the RNA genome was obtained using a program found in the literature [Voss and Gerstein, 2005].

This program provides predicted volume of RNA and proteins by just providing the base pair transcript of the molecules. This software does take into account many factors such as atomic radii, crystal packing, structural complexity, solvent and associated protein to be able to provide a universal set of volumes that can be applied to proteins and RNAs [Voss and Gerstein, 2005]. This program provided us with a predicted volume of 1457 nm^3 for the volume of TBSV full genomic RNA, which as a size of 4777bp. The apparent volume of individual TBSV genomic RNA obtained from the AFM images fell within a broad peak centered at 2161± 388 nm^3, (Fig 11.7). The measured apparent volume from the AFM data was over estimated as expected due to the tip broadening effects. The measured volume values were high and illustrate the compactness of the conformation of the TBSV genomic RNA. This can be concluded from the fact that there were no observed structures with relatively low volume values, which would illustrate linear conformation (Fig 11.7). This is in conformity with the proposed structure, due to series of long-range RNA-RNA interactions leading to a compact structure of the genome. Six different functional long-range RNA-RNA base pairing interactions have been identified, required for different process of the TBSV virus survival. These processes include translation of p33 and p92 coding region to produce their respective proteins, genomic replication, and transcription of the sub-genomic mRNA [Wu et al., 2013]

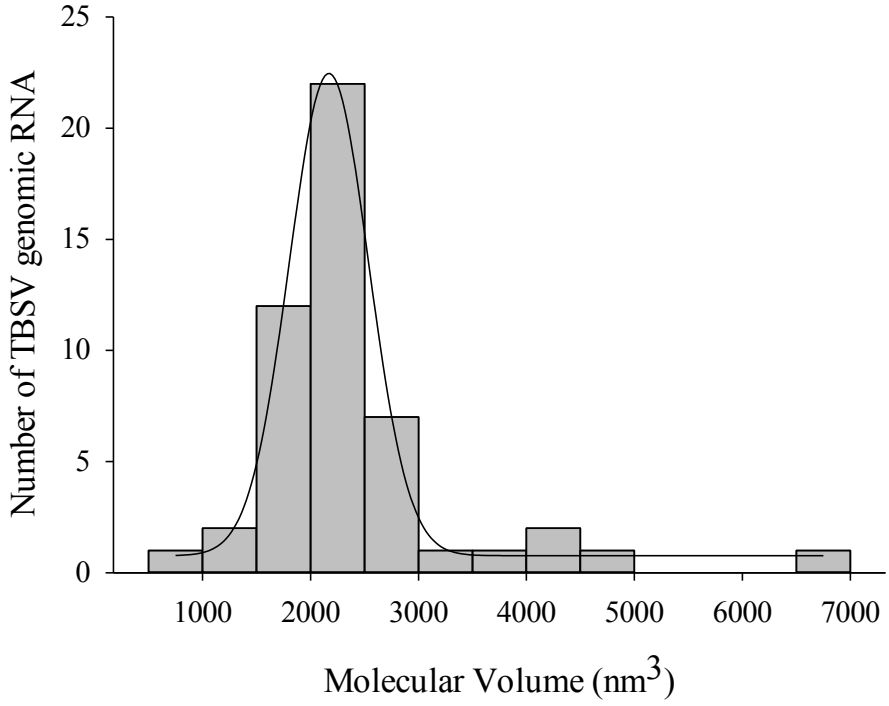

Figure 11.7: Measured apparent volume of TBSV genomic RNA from AFM images.

The measured apparent volumes for the Sg1 mRNA from AFM images showed a broad peak centered at 666 ± 153 nm^3, (Fig 11.8a). This is very close to the predicted volume of 658 nm^3 for sg1 mRNA with a size of 2157bp. The measure volume for Sg2 mRNA molecules from the AFM images also shows a broad peak centered at and 369 ± 56 nm^3, (Fig 11.8b). This is in close conformity with the predicted volume of 286 nm^3 for Sg2 mRNA with a size of 936bp obtained from the program. The volume analysis illustrates that both Sg1 and Sg2 mRNA molecules, did adopt their respective expected confirmation. Such volume analysis has also been performed in the literature for icosahedral satellite tobacco mosaic virus (STMV) [Archer et al., 2013].

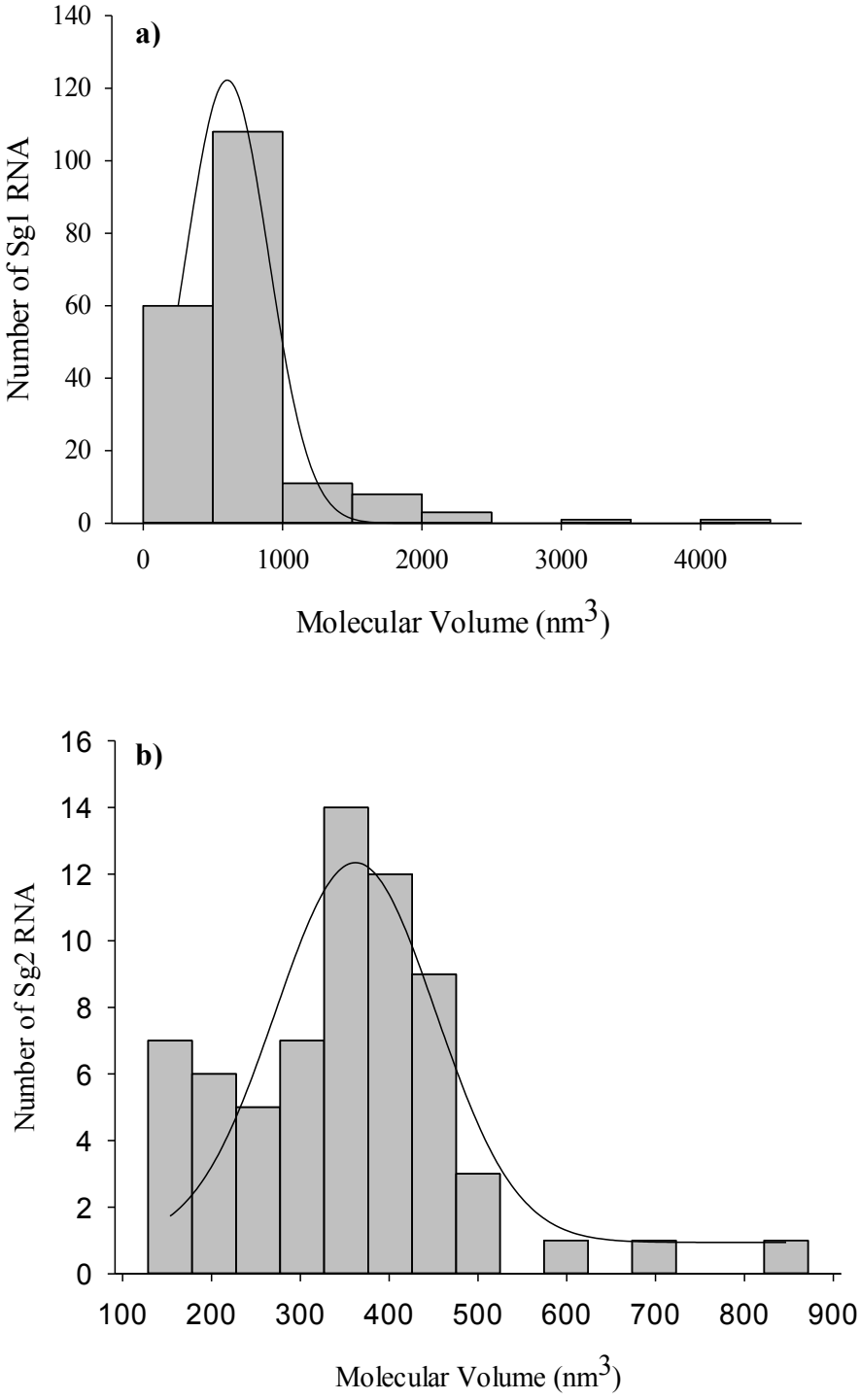

Figure 11.8: Measure apparent volume of observed features of by AFM TBSV: **a)** Sg1 mRNA, **b)** Sg2 mRNA.

Chapter Twelve

Conclusion

Atomic force microscopy has proved to be a valuable tool for structural analysis of protein-DNA complexes. Classical biochemistry techniques have been used to investigate different aspect of DNA binding activity of VraR, however AFM provides direct visualization of binding site and stoichiometry of phosphorylated VraR binding to *vraSRp*. Using volume analysis, VraR protein deposited on mica was discovered to be present on the surface mostly as a monomer, whereas phosphorylated VraR was present on surface as mostly dimers. Statistical volume analysis for phosphorylated VraR shows complexes with volume corresponding to the oligomer of phosphorylated VraR. VraR protein binds to site R1 with great affinity. At this site the recognition sequence are present as two tandem repeats which, lead to the proposition that VraR would bind to each of these sites as dimer [Belcheva et al., 2009]. It was also proposed that binding of VraR lead to recruitment of more VraR to site R2 upon phosphorylation. As expressed in this thesis, phosphorylated VraR bound to complex site as an oligomer, which will be complementary to what was proposed by Belcheva et al. Our findings are somewhat in agreement with what was published previously.

Most protein-DNA complexes studied in the literature are easily observed routinely by AFM and this is due to the high stability of the complexes and the low dissociation constant that usually are in the nano molar range [Bustamente et al., 1996]. The difficulty of this research dealt with the high dissociation constant of the VraR-*vraSRp* complexes in the low micro molar range [Belchva et al., 2009]. This made it

challenging to visualize the complexes at high frequency. However by optimizing our experimental conditions, tapping mode AFM images of the complexes were obtained repeatedly. This enabled us to perform statistical measurements confirming the specificity of the visualized complexes and stoichiometry of the protein at complex sites. In this thesis, AFM enables us to provide supporting information guiding our understanding of VraR-DNA interactions essential for gene regulation processes required by the VraSR signal transduction system of staphylococcus aureus in coordinating a response to antibiotic that inhibit cell wall peptidoglycan biosynthesis.

In addition, the visualized structure by the AFM of the TBSV genomic and sub-genomic RNA shows a family of conformations whose features are consistent with a compact overall structure with different branches/domain protruding from the core. The protruding branches confirm the existence of the long-range RNA-RNA interactions leading to complex secondary structures. The long-range RNA-RNA interactions determined are utilized by TBSV for different viral processes. The AFM images provide visual confirmation of the RNA genomic structure, which previously could only have been predicted statistically. The volume analysis supports the observed compact structure, and also support that none of the observed structure exhibits a fully extended structure. The observed conformation of the sub-genomic mRNA with the highest percentage is in conformity with the predicted SHAPE structure. The apparent volume of the sub-genomic mRNA obtained from the AFM images are also compatible with that volume predicted by the software using the base pairs. Overall, our results strongly support the biochemical and bioinformatics analysis. It also provides evidence and further insight into the existence of base pairing interactions of genomic RNA leading to a highly ordered structure.

Chapter Thirteen

Concluding Remarks and Future Directions

The main objective of this thesis was to enhance the capacity of desorption electrospray ionization mass spectrometry for analysis of biomolecules and tissue cells. As well as to apply atomic force microscopy to investigate and visualize biomolecules, and biomolecular interactions. With both analytical techniques we have made use of surface and interfacial approaches. Whereby for DESI-MS we have fabricated and functionalized porous silicon surface and made use of the interaction at the surface interface for enhancement of the DESI analysis. Conversely we made use of mica substrate with divalent cationic buffer to allow investigation of biological molecules by AFM.

Desorption electrospray ionization mass spectrometry is an ambient ionization technique that allows characterization and analysis of sample with minimal sample preparation. It is an emerging technique for analysis of biomolecules, tissue cell and early disease diagnosis. Effectiveness of this technique depends on the improvement of its desorption/ionization mechanism. In this research, we successfully implemented the use of functionalized porous silicon as suitable substrate for the enhancement of the desorption/ionization mechanism of DESI. In chapter five, we demonstrated the increase in stability of DESI signal of the investigated small molecules on the functionalized porous silicon substrate over time. We observed that the functionality of the porous silicon does affect the carry-over of analytes and their ionization efficiency. We concluded that super hydrophobic porous surfaces are the most ideal substrate for DESI analysis for it

prevents cross contamination of analytes; it provides increase ionization efficiency and lowest limit of detection of small molecules. Our proposed mechanism for improvement of the desorption/ionization of DESI, based on functionalized porous, silicon involves the hypothesis that the analyte are concentrated on a small sampling spot, the analyte do not penetrate into the pore due to the hydrophobic functionality, and the pores acts as a barrier concentrating the analyte in the spray solvent pool leading to efficient desorption/ionization. This mechanism showed improved desorption/ionization efficacy without fast removal of the sample, therefore maintaining high signal strength and stability for longer period of time. We obtained two orders of magnitude increase of the ion signal intensity compare to traditional porous PTFE surface also used for DESI analysis.

The investigated functionalized porous silicon surfaces could be suitable for several applications, such as quantitation analysis in real samples and especially for blotting or imprint techniques in imaging analysis. Future direction of this work includes fabrication of porous silicon surfaces with different functional groups to target specific molecules and reactive DESI experiments, making use of silicon facile surface chemistry. In addition, specific functional groups can also be produced on porous silicon surface at relatively low cost to enhance selective analysis of a variety of compounds. Investigating the desorption/ ionization efficiency of the porous silicon surfaces with different spray solvent, to determine how to further enhance the capacity of the instrument. Also porous silicon of varying thickness can be investigated to determine, which thickness is optimum for DESI analysis. Further optimization of the DESI parameters can be investigated using porous silicon as substrate. It is critical to develop protocol for sample preparation of soft

biomolecule, for DESI-MS imaging analysis. These new surfaces could potentially be commercialized bringing analytical advantages to DESI users.

Understanding pathogens and their infections requires the investigation at molecular level and this is indeed relevant for many biological systems. Protein-DNA binding and structural conformation of RNA have been investigated using different analytical techniques, where some are highly time consuming, requiring extensive sample preparation and others require the biomolecules to be tethered to the surface. However these techniques, i.e., EMSA and DNA foot printing has reveled valuable information of protein-DNA interactions. In conjunction with the SHAPE analysis method, valuable insight into the molecular conformation of various RNA molecules was obtained. Studying biomolecular interaction using AFM technique has become an emerging tool that provides information to better understand biological systems. Over the years, AFM has been use to characterize the geometry and spatial relationships of several protein-DNA complexes.

AFM was used for characterization of VraR-DNA complexes from *staphylococcus aureus*. AFM was used to confirm not only the binding site of the VraR protein, but also to ascertain the specificity of the binding interaction, and the stoichiometry of the complex [Ore, 2010]. In this thesis, we further our research through the investigation of DNA binding activity of phosphorylated VraR (chapter ten). Phosphorylated VraR was observed to be present as mostly dimer when deposited on a mica surface and imaged with AFM. Whereas binding of phosphorylated VraR with DNA *vraSRp* revealed a stoichiometry of oligomer at the complex site. DNase I foot printing revealed that phosphorylated VraR binds to three different sites on the *vraSRp* DNA, each site has tandem repeat leading to

VraR binding to each site as dimer. When all three sites are occupied, this lead to stoichiometry of phosphorylated VraR at complex sit as oligomer, which was what we observed from the AFM images. Future direction of this work would involve the investigation of the complex in solution near physiological conditions using AFM. Also our developed protocol can be used for the analysis of other biological relevant protein-DNA complexes. Understanding of two- component system can lead to interest as potential targets for new drug developments. As well future development of structural genomic technologies, and rapidly improving imaging techniques can drive new discoveries about two-component systems.

In chapter eleven, we provided for the first time, the AFM images of the three dimensional conformation of tomato bushy stunt viral genomic and sub-genomic RNA. The images are representation of the compactness of the TBSV genome due to the existence of long RNA-RNA interactions proposed by our collaborator Dr. White. AFM enables the confirmation of the SHAPE predicted of both the full genomic and sub genomic RNA structures. Volume analysis also supports the proposed structure, where the high volume value from the AFM images of the full genome suggests that of a compact structure. For the sub genomic RNA, the volumes from the AFM images was close to the predicted volume provided from the software. AFM was useful in not only supporting the proposed structure, but also confirming the existent of the long-range RNA-RNA interactions that are crucial for different biological process for the survival and propagation of the virus. Since TBSV replication processes similar to other viruses, such as humans and animal viruses, understating its viral infection process can provide insight into the infection process of other similar viruses. It should be noted that the use of

chemically modified surfaces could be beneficial in imaging of biological relevant system by ensuring that interactions between the biological molecules and the surface are optimized to ensure that the biological structure is as closed as possible to the one observed in solution.

Recently, mass spectrometry and atomic force microscopy have been combined as complementary techniques to provide both spatially resolved chemical information and physical characterization of the sample. Ovchinnikova et al. made use of atomic force microscopy probe for nanoscale proximal probe thermal desorption/electrospray ionization mass spectrometry. This involve heating up the AFM probe and brought in contact with the sample surface for thermal desorption /ionization of the caffeine analyte [Ovchinnikova et al. 2008]. The use of AFM probe allow reproducible mass spectral signal and imaging quality to be improved by incorporating a fixed real time optimal probe to surface distance particular in a imaging mode that continuously adapts to the changing topography of the surface during a line scan [Ovchinnikova et al. 2008]. This could potential eliminate the challenge of imaging soft samples in DESI-MS whereby the tip can adjust to changes in sample topography and eliminate issues with the imaging of rougher samples.

References

Ackermann, D., Jester, S.S., Famulok, M. *Angew.Chem. Int. Ed*. 51: 1-6 (2012).

Akamine, S., Barrett, R.C., Quate, C.F. *Appl. Phys. Lett.* 57: 316-318 (1990).

Ahlquist, P., Naueiry, A.D., Lee, W.M., Kushner, D.B., Dye, B.T. *J. Virol.* 77: 8181-8186 (2003).

Alessanrini, A., Facci, P., *Meas. Sci. Technol.* 16: 65-92 (2005).

Alvarez, D.E., Lodiero, M.F., Luduena, S.J., Pietrasanta, L.I., Gamarnik, A.V. *J. Virol*. 29: 6631-6643 (2005).

Ando, T., Uchihashi, T., Fukuma, T. *Progress in surface science.* 83: 337- 437 (2008).

Archer, E.J., Simpson, M.A., Watts, N.J., O'Kane, R., Wang, B., Erie, D., Mcpherson, A., Weeks, K.M. *Biochem.* 52: 3182-3190 (2013).

Belcheva, A., Golemi-Kotra, D. *J. Biol. Chem*. 282: 12354-12364 (2008).

Belcheva, A., Verma, V., Golemi-Kotra, D. *Biochem.* 48: 5592-5601 (2009).

Binning, G., Quate, C.F., Gerber, C. *Phys. Rev. Lett*. 56: 930-933 (1986).

Bustamente, C., Vesenka, J., Tang, CL., Rees, W., Guthold, M., Keller, R. *Biochem.* 3: 22-26 (1992).

Bustamante, C., Rivetti, C. *Annu. Rev. Biopys. Biomol. Struct.* 25: 395-429(1996)

Bustamente, C., Keller, D., Yange G. *Curr. Opin. Struct. Bio*l. 3: 363-372(1993).

Butt, H., Cappella, B., Kappl, M. *Surface Science Reports*. 59: 1-152 (2005).

Canale, C., Torre, B., Ricci, D., Braga, C.P. Recognizing and Avoiding Artifacts in Atomic force Microscopy Imaging. Ricci D, Braga C.P Atomic force microscopy in biomedical research: Methods and Protocols. Eds. 2011, New York: Humana Press.

Carvalho, F.A., Santos, N.C. *Life.* 64,6: 465-472 (2012).

Casino, P., Rubino, V., Marina, A. *Curr. Opin. Struct. Biol*. 20: 763-771 (2010).

Cross, S.E., Jin, Y.S., Rao, J., Gimzewski, J.K. *Nat. Nanotechnol.* 2: 780-783 (2007).

Davis, M., Sagan, S.M., Pezacki, J.P., Evans, D.J., Simmonds, P. *J. Virol.* 82: 11824-11836 (2008).

Deigan, K.E., Li, T.W., Mathews, D.H., Weeks, K.M. *PNAS*. 106,1: 97-102 (2009).

Del Sol, R., Armstrong, I., Wright, C., Dyson, P. *J. Bacteriol.*189: 2219-2225 (2007).

Dey, B., Thukral, S., Krishnan, S., Chakrobarty, M., Gupta, S., Manghani, C., Rani, V. *Mol. Cell. Biochem.* 365: 279-299 (2012).

Donaldson, L.W. *Biochemistry*. 47,11: 3379-3388 (2008).

Eaton, P., West, P. AFM instrumentation: Atomic force microscopy. 2010. Oxford university press.

Edstrom, R.D., Menike, M.H., Yang, X., Yang, R., Elings, V., Evans, F. *Biophys J.* 58: 1437-1448 (1990).

Erie, D., Yang, G., Schultz, H., Bustamante, C. *Science.* 266: 1562-1566(1994).

Fabian, M.R., White, K.A . *J Biol Chem*. 279: 28862-72 (2004).

Fernandez, J.M., Li, H.B. *Science.* 303: 1674-1678 (2004).

Funetes- Perez, M.E., Dillingham, M. S., Moreno-Herrero, F. *Methods.* 6: 113-121 (2013).

Gahlin, R., Jacobson, S. *Wear.* 222,2: 93-102 (1998).

Gamarnik, A.V., Andino, R. *Genes Dev.* 12: 2293-2304 (1998).

Guthold, M., Zhu, X., Rivetti, C., Yang, G., Thomson, N. H., Kasas, S., Hansma, H. G., Smith, B., Hansma, P. K., and Bustamante, C. *Biophys. J.* **77**: 2284-94 (1999).

Hafner, J.H., Cheung, C.L., Woolley, A.T., Lieber C.M. *Prog. Biophys. Mol. Biol.* 77: 73-110 (2001).

Hanaki, H., Kuwahara-Arai, K., Boyle-Vavra, S., Daum, R. S., Labischinski, H., Hiramatsu, K. *J Antimicrob Chemother*. 42,2: 199-209 (1998)

Hansma, H. G., Benzanila, M., Zenhausern, F., Adrian, M., and Sinsheimer, R.L. *Nucl. Acids. Res*. 21: 505-512 (1993).

Hansma, H.G., Oroudjev, E., Baudrey, S., Jaeger, L. *J. Microsc.* 212: 273-279 (2003).

Harada, Y., Ohara, O., Takatsuki, A., Itoh, H., Shimamoto, N., Kinosita, K. *Nature*. 409: 113-115 (2001).

Hearne, P.Q., Knorr, D.A., Hillman, I., Morris, T.J. *J. Virol.* 177: 141-151 (1990).

Heddle, J. G., Mitelheiser, S., Maxwell, A., Thomson, N. H. *J Mol Biol.* 337: 597-610 (2004).

Hiramatsu, K., Cui, L., Kuroda, M., and Ito, T. *Trends Microbiol.* 9: 486-493 (2001).

Hofmann, A., Simon, A., Grkovic, T., Jones, M. Methods of Molecular Analysis in Life Science. Cambridge University Press. Cambridge. (2014).

Horber, J.K.H., Miles, M.J. *Science*. 302: 1002-1005 (2003).

Hoshi, O., Ushiki, T. *Methods. Mol. Biol.* 736: 109-115 (2011).

Ido, S., Kimura, K., Oyabu, N., Kobayashi, K., Tsukada, M., Matsushige, K., Yamada, H. *ACS Nano.* 7: 1817-22 (2013).

Jalili, N., Laxminarayana, K. *Mechatronics.* 14: 907-945 (2004).

Jung, K., Fried, L., Behr, S., Heermann, R. *Curr. Opin. Microbiol*. 15: 118-124 (2012).

Kasas, S., Thomson, N.H., Smith, B.L., Hansma, H.G., Zhu, X., Guthold, M., Bustamante, C., Kool, E.T., Kashlev, M., Hansma, P.K. *Biochem.* 36,2: 461-468 (1997).

Kebbekus, P., Draper, D.E., Hagerman, P. *J. Biochem.* 34: 4354-4357 (1995).

Kobayasi, M., Sumitomo, K., Torimitsu, K. *Ultramicroscopy*. 107:184-190. (2007).

Krautbauer, R., Rief, M., Gaub, H.E. *Nano. Lett.* 3: 493-496 (2003).

Klinov, D.V., Neretina, T.V., Prokhorov, V.V., Dobrynina, K.G., and Demin, V.V. ` B*iochem (moscow)*. 74: 1410-1415 (2009).

Kuroda, M., Kuwahara-Arai, K., Hiramatsu, K. *Biochem Biophys Res Commun.* 269: 485-90 (2000).

Kuroda, M., Kuroda, H., Oshima, T., Takeuchi, R., Mori, H., and Hiramtsu, K. *Mol. Microbiol*. 49: 807-821 (2003).

Kuznetsov, Y.G., Daijogo, S., Zhou, J., Semler, B.L., McPherson, A. *J. Mol. Biol*. 347: 41-52 (2005).

Kuznetsov, Y., Gershon, P.D., McPherson, A. *J. Virol*. 82: 7551-7556 (2008).

Kuznetsov, Y., McPherson, A. *Micro Biol. Mol. Biol. Rev.* 75,2: 268-285 (2011).

Lee, G.U., Chrisey, L.A., Colton, R.J. *Science*. 266: 771-773 (1994).

Leonard, P.G., Golemi-kotra , D., Stock, A.M. *PNAS.* 110,10: 8525-8530 (2013).

Leung, C., Bestembayeva, A., Thorogate, R., Stinson, J., Pyne, A., Marcovich, C., Yang, J., Drechsler, U., Despont, M., Jankowski, T., Tschope, M., and Hoogenboom, B.W., *NanoLett.* 12: 3846-3850 (2012).

Lindenbach, B.D., Sgro, J.Y., Ahlquist, P. *J Virol.* 76: 3905-3919 (2002).

Low, J.T., Weeks, K.M. *Methods*. 52: 150-158 (2010).

Lushnikov, A. Y., Brown, B. A., Oussatcheva, E. A., Potaman, V. N., Sinden, R. R., Lyubchenko, Y. L. *Nucleic Acids Res.* 32: 4704-4712 (2004).

Lyubchenko, Y.L., Gall, A.A., Shylakhtenko, L.S., Harrington, R.E., Jacobs, B.L., Oden, P.I. *J. Biomol. Struct. Dyn.* 10: 589-6060 (1992).

Lyubchenko, Y.L., Shylakhtenko, L.S., Ando, T. *Methods*. 54: 274-283 (2011).

Magnov, S.N., Elings,V., Whangbo, M.H. *Science*. 375: 2385-239 (1997).

Mateos-Go´mez, P.A., Zun˜iga, S., Palacio, L., Enjuanes, L., Sola, I. *J Virol.* 85: 8968-8980 (2011).

Mathews, D.H. *Curr. Protoc .Bioinformatics* . Chapter 12: Unit 12.6 (2006).

Melcher, J., Matinez-Martin, D., Jaafar, M., Gomez-Herrero, J., Raman, A. *Beilstein. J. Nanotechnol*. 4: 153-163 (2013).

Miller, E., Garcia, T., Hultgren, S., Oberhauser, A.F. *Biophys. J.* 91,10: 3848-3856 (2006).

Miyahara, Y., Deschler , M., Fujii, T., Watanabe, S., Bleuler, H. *Appl. Surf. Sci*. 18: 450 (2002).

Meyer, G., Amer, N.M. *Appl, Phys. Lett.* 53: 1045-1047 (1988).

Moller, C., Allen, M., Elings, V., Engel, A., Muller, D.J. *Biophys.* 77: 1150-1158 (1999).

Morris V.J, Kirby A.R., Gunning, A.P. Atomic Force Microscopy for Biologist. Imperial College Press. London. (1999).

Neaves, K. J. Cooper, L.P., White, J.H., Carnally, S.M., Dryden, D.T.F., Edwardson, J.M., Hdnderson, R.M. *Nucleic acids research.* 37: 2053-2063 (2009).

Neish, C.S., Martin, I.L., Henderson, R.M., Edwardson, J.M. *British. J. of Pharmacol*. 135: 1943-1950 (2002).

Nicholson, B.L., White, K.A. *Nature Rev-Microbiol*. 450-451: 258-265 (2014)

Ore, M.O. DNA binding activity of vancomycin resistance associated regulatory protein VraR by atomic force microscopy. M.Sc. Dissertation. York University. (2010).

Oster, S.K., Wu, B., White, K.A. *J. Virol*. 72,7: 584-5851 (1998).

Pastre, D., Hamon, L., Sorel, I., Le Cam, E., Curmi, P.A., Pietrement, O. *Langmuir*. 26: 2618-2623 (2009).

Pogany, J., Fabian, M.R., White, K.A., Nagy, P.D. *The EMBO journal*. 22,20: 5602-5611 (2003).

Pyne, A., Thompson, R., Leung, C., Roy D., Hoogenboom, B.W. *Small*. 10: 3257-61 (2014).

Rajendran, A., Endo, M., Sugiyama, H. *Chem. Rev.* 114: 1493-1520 (2014).

Ratcliff, G.C., Erie, D. A. *J. Am. Chem. Soc*. 123: 5632-5635 (2001).

Revenko, I., Proksh, R. *J. Appl. Phys.* 87: 526-533 (2000).

Rivetti, C., Guthold, M., and Bustamante, C. *J Mol Biol*. 264: 919-932 (1996).

Rivetti, C., Guthold, M., and Bustamente, C. *EMBO. J*. 18: 4464-4475 (1999).

Rode, S., Oyabu, N., Kobayashi, K., Yamada, H., Kuhnle, A. *Langmuir*, 25: 2850-2853 (2009).

Schlacher, K., Leslie, K., Wyman, C., Woodgate, R., Cox, M. M., and Goodman, M. F. *Mol Cell.* 17: 561-572 (2005).

Schneider, S. W., Larmer, J., Henderson, R. M., and Oberleithner, H. *Pflugers Arch.* 435: 362-367 (1998).

Schneider, S., Folprecht, G., Krohne, G., Oberleithner, H. *Pflugers Arch* 430: 795-801 (1995).

Seeman, N.C. *Annu. Rev. Biophys. Biomol. Struc*. 27: 225-24 (1998).

SPM Training Note book. Veeco, instrument Inc. (2003).

Tamayo, J., Garcia, R. *Langmuir.* 12: 4430-4435 (1996).

Tessmer, I., Kaur, P., Lin, J., Wang, H. *J. Nanobiotechnol.* 11,25: 1-7 (2013).

Timofeeva, O.A., Chasovskikh, S., Lonskaya, I., Tarasova, N.I., Khavrutskii, L., Tarasov, S.G., Zhang, X., Korostyshevskiy, V.R., Cheema, A., Zhang, L., Dakshanamurthy, S., Brown, M.L., Dritschilo, A. *J. Biol. Chem.* 287,17: 14192-14200 (2012).

Torre B, Ricci D, Braga C.P. How the Atomic force microscope works. Ricci D, Braga C.P Atomic force microscopy in biomedical research: Methods and Protocols. Eds. 2011, New York: Humana Press.

Uehara, H., Osada, T., Ikai, A. *Ultramicroscopy.* 100: 197-2001 (2004).

Vahabi, S., Salman, B.N., Javanmard, A. *IJMS.* 38, 2: 76-83 (2013).

Voss, N.R., Gerstein, M. *J. Mol. Biol*. 346: 477-492 (2005).

White, K.A., Nagy, P.D. *Prog Nucleic Acids Res Mol Biol* .78: 187-226 (2004).

Wilkinson, K.A., Gorelick, R.J., Vasa, S.M., Guex, N., Rein, A., Mathews, D.H., Giddings, M.C., Weeks, K.M. *PloS Biol.* 6, e96 (2008).

Wolter, O., Bayer, T., Greschner, J. *J. Vac. Sci. Technol.* 9: 1353-1357 (1991).

Wu, B., Grigull, J., Ore, M.O., Morin, S., White, K.A. *PLoS Pathog* 9(5): e1003363 (2013).

Wu, B., Pogany, J., Na, H., Nicholson, B.L., Nagy, P.D, White, K.A. *PLoS Pathog* 5(3): e1000323 (2009).

Wyman, C., Rombel, I., North, A. K., Bustamante, C., and Kustu, S. *Science*. 275: 1658-1661 (1997).

Yang, Y., Wang, H., and Erie, D. A. *Methods*. 29: 175-187 (2003).

Yang, L., Wang, K., Tan, W., He, X., Jin, R., Li, J.., Li, H. *Anal. Chem*.78: 7341-73455 (2006)

Yang, C., Hwang, I., Chen, Y.F., Chang, C.S., Tsai, D.P. *Nanotechnology.* 18: 084009 (2007)

Yin, S., Daum, R.S., Boyle-Vavra, S. *Antimicrob. Agent Chemother*. 50: 336-343 (2006)

Yoffe, A.M., Prinsen, P., Gopal, A., Knobler, C.M., Gelbart, W.M., et al. *Proc Natl Acad Sci USA* 105: 16153-16158 (2008).

Yokokawa, M., Yoshimura, S. H., Naito, Y., Ando, T., Yagi, A., Sakai, N.,

Takeyasu, K. *IEE Proc., Nanobiotechnol*. 153 ,4: 60-66 (2006)

Zlatanova, J., Lindsay, S.M., Leuba, S.H. *Progress in Biophy & Mol Biol.* 74: 32-61 (2000)